Design and Investigation of PCF based Highly Sensitive Surface Plasmon Resonance Biosensors

by

Zarrin Tasnim (160021034)
Rakina Islam (160021050)
Raisa Labiba Khan (160021064)
Ehtesam Moazzam (160021104)

A Thesis Submitted to the Academic Faculty in Partial Fulfillment of the Requirements for the Degree of

BACHELOR OF SCIENCE IN ELECTRICAL AND ELECTRONIC ENGINEERING

Department of Electrical and Electronic Engineering
Islamic University of Technology (IUT)
Gazipur, Bangladesh

March 2021

Design and Investigation of PCF based Highly Sensitive Surface Plasmon Resonance Biosensors

Approved by:

Dr. Mohammad Rakibul Islam

Supervisor and Professor,
Department of Electrical and Electronic Engineering
Islamic University of Technology (IUT)
Boardbazar, Gazipur-1704.

Date: ……

Table of Contents

List of Tables

List of Figures

List of Acronyms

PCF	Photonic Crystal Fiber
SPR	Surface Plasmon Resonance
SPW	Surface Plasmon Wave
SP	Surface Plasmon
SPP	Surface Plasmon Polariton
RIU	Refractive Index Unit
RI	Refractive Index
TE	Transverse Electric
TM	Transverse Magnetic
EMI	Electromagnetic Interference
TIR	Total Internal Reflection
ATR	Attenuated Total Reflection
FEM	Finite Element Method
THz	Terahertz
SNR	Signal to Noise Ratio
FBG	Fiber Bragg grating
SERS	Surface Enhances Raman Scattering
CL	Confinement Loss
AS	Amplitude Sensitivity
WS	Wavelength Sensitivity
PML	Perfectly Matched Layer
FOM	Figure of Merit
FWHM	Full Width At Half Maximum
LSPR	Localized Surface Plasmon Resonance
AZO	Aluminum-Doped Zinc Oxide
TIN	Titanium Nitride
EML	Effective Material Loss
TC-PQF	Trapezoidal Channel Photonic Quasi-Crystal Fiber
TIO_2	Titanium dioxide

List of Symbols

$\mathcal{E}_0$	: Relative permeability
μ_0	: Permittivity in free space
n_{mat}	: Refractive index of the material
E	: Modal electric
$\propto_{eff}$	: Bulk material absorption loss
α_{loss}	: Confinement Loss
S_Z	: Z-component of the poynting vector
f	: Frequency of the guiding light
c	: Speed of light in vacuum
$\mathrm{Im}(n_{eff})$	: Imaginary part of the effective index of the guided mode
n_x and n_y	: RI of two orthogonal components of the polarization maintaining wave
A_{eff}	: Effective modal area
R	: Bending radius
n_{co}	: Refractive indices of the core
n_{cl}	: Refractive indices of the cladding
n_{eff}	: Effective refractive index
$\omega = 2\pi f$	: Angular frequency
$I(r) = \lvert E_t \rvert^2$	: Transverse electric field intensity in the cross section of the fiber
γ_D	: Damping frequency
ω_D	: Plasma frequency
Λ	: Pitch
$\epsilon\propto$	: Permittivity at high frequency
ε_∞	: Intra-band dielectric constant at infinity
$\Delta\epsilon$	: Weighting factor
ΩL	: Oscillator strength
d_c	: Diameter of the central air hole
r	: Radii of air holes
t_g	: Thickness of gold
t_{Ag}	: Thickness of silver
t_t	: TiO_2 film thickness
n_a	: Refractive index

n_C : Number of core air holes

ε : Intra-band dielectric constant

Γ : Damping coefficient

m_e : Free electron mass

n_t : Refractive index of ITO

λ : Wavelength

ε_{Ag} : Relative permittivity of silver

ω : Resonant frequency

Acknowledgements

"In the name of Allah, The Most Gracious and The Most Merciful". By the grace of ALLAH (S.W.T) we have completed our thesis work with satisfying results. We want to show gratitude towards our thesis supervisor Dr. Md. Rakibul Islam Dean, Faculty of Science and Technical Education (FSTE), Professor, Electrical and Electronic Engineering (EEE) Dept., Former Head, Business and Technology Management (BTM) Department for his constant guidance, convivial attitude and tremendous support during our learning sessions. His encouragement and amiable behavior towards us helped us to accomplish the goal of our thesis work. We would also like to thank the respected faculty members of the Department of Electrical and Electronic Engineering for their support during our thesis work. Their suggestions and helpful attitude also helped us in our research work. We also want to thank our parents for their continuous support .Without them it would have become difficult for us to finish our work. Lastly we would like to thank all our well-wishers.

Abstract

Due to SPR based PCF possessing numerous advantages, researchers have focused on improving the design of these sensors. As a result, sensors with better sensing performances are discovered and some are on the way to be discovered. While designing the sensors researches focused on choosing the appropriate plasmonic material, easier fabrication process, better sensing approach. Their main concerns were to design such sensors which could be practically implemented. In order to get better sensing performance, the sensor design becomes complex. So difficulty while fabricating can be faced. We tried to propose three designs for our thesis paper which gave us satisfying results .We also tried to focus on reducing the problems faced. In our first design, we proposed a circular lattice structure with gold coating. Our proposed design was surrounded with a thin PML layer. We tried to optimize various parameters like gold, PML, airholes and chose the values which gave us the best result. In our second design we proposed a highly sensitive SPR based PCF biosensor in which we used gold as the plasmonic material. We adapted stack and draw method for designing the propose sensor so that fabrication becomes easier. For this proposed design also we tried to optimize various parameters and chose the values which gave us the best results. In our last proposed design we tried to explore the sensitivity performance as well as the temperature sensitivity performance. In all cases we used COMSOL Multiphysics 5.3a and Matlab for our researched work. The sensing outputs of the proposed designs were explored by Finite Element Method (FEM). Our first proposed design gave the amplitude sensitivity of 1779 RIU^{-1} , 407 RIU^{-1} and wavelength sensitivity of 3000 nm/RIU, 2000 nm/RIU in x and y polarization modes respectively. In this case analyte refractive index (RI) was varied from 1.32 to 1.37 accordingly. This design gave a minimum amplitude sensor resolution of 5.6210^{-6} and a minimum wavelength sensor resolution of 3.3310^{-5}. We also obtained a birefringence of 0.0049 and FOM value of 187.5..The second proposed sensor gave us the maximum wavelength sensitivity of 14,500 nm / RIU in X-polarization mode and the maximum amplitude sensitivity of 4738.9 RIU^{-1} for Y-polarized mode, respectively .The RI was varied in the range of 1.35–1.41 .This sensor gave the lowest wavelength sensor resolution of 6.9×10^{-6}RIU and the lowest amplitude sensor resolution of 2.11×10^{-6}RIU for Y-polarized mode with FOM of 387 and 364 for X and Y polarization. Our last proposed sensor gave us the amplitude sensitivity of 1432 RIU^{-1} and 1291 RIU^{-1} in X and Y polarized mode, respectively. It gave a wavelength sensitivity of 13,500 and 13,000 in X and Y polarized mode respectively. Sensor resolutions of 7.407×10^{-8} and 7.692310^{-8} were obtained using wavelength interrogation method and 6.983210^{-6} , 7.7459310^{-6} were obtained by using amplitude interrogation method in Y and X polarized mode respectively. FOM value of 521.4601 and 546.93 were obtained for X and Y polarization method. Birefringence of 1.5×10^{-3} was found for the proposed sensor. Temperature sensitivity for temp range (-114 to 78℃) was 4.5833 nm/℃. So after observing the results of our proposed sensors we can say that our sensors can be used for sensing purposes.

Chapter 1

Introduction

1.1 Background History

A great number of advantages are offered by optical sensors. They are capable to direct real-time and label-free detection of many chemical and biological substances. Cost-effectiveness, high precision, small size, and sensitivity are among their benefits.

In the implementation of modern optical biosensors, several advanced principles and highly multidisciplinary methods are applied, including micro/nano-technologies, microelectronics, micro-electromechanical systems (MEMSs), chemistry, molecular biology, and biotechnology. There has been an unprecedented increase in the scientific and technical advancement of optical biosensors over the past decade. The research and development of optical biosensors have been primarily targeted at healthcare, environmental applications, and the biotechnology industry.

One of the most improved optical sensing technologies is an optical chemical and biomolecular sensor based on Surface Plasmon Resonance (SPR) [1]. Surface Plasmon Resonance is an incidence that occurs at the interface of a metal-dielectric media with different refractive indices when polarized light reaches a metal film.

SPR technology is used widely as a transducer for affinity-based biosensors. An affinity biosensor based on SPR is composed of a recognition element or ligand immobilized on an SPR transducer's metal surface. SPR techniques detect mutual oscillations of free electrons (called surface plasmons), in which light is focused through a glass prism on a metal film and the resulting reflection is observed. SPR is a label-free process that requires no additional reagents, checks, or laborious preparation measures for the sample. The key advantages of this technique are that it simply reacts to refractive index changes caused by molecular binding events. The biological recognition factor is immobilized at the sensor surface in SPR biosensors, and the analyte solution generally passes across the sensor-analyte interface via a microfluidic channel.

In recent years, studies have documented the use of SPR, its application, method of implementation, SPR technology, with more than 1000 new publications every year [2]. Surface plasmons, including second-harmonic generation, Raman scattering and fluorescence, have been used to increase the surface sensitivity of many spectroscopic measurements. However, SPR reflectivity measurements can be used in their simplest form to detect molecular adsorption, such as proteins, DNA etc.

1.2 Identified Problem

Several PCF SPR sensors have been investigated so far. Due to specific coating of metal layers and liquid penetration within the air-hole surface, most of the recorded sensors are difficult to fabricate (Dash & Jha, 2014b; Gao, Guan, Wen, Zhong, & Yuan, 2014; Qin, Li, Yao, Xin, & Xue, 2014; Shuai, Xia, & Liu, 2012). Furthermore, the output of these documented sensors is observed by following the inside sensing operation. To remove liquid infiltration and metal coating problems, D-shaped PCF SPR sensors were recently demonstrated, reducing the metal coating issue. For these sensors, achieving high sensitivity while having a low loss is still a challenge. So far, the following limitations have been found for SPR-based optical sensors:

- Complex design due to high sensitivity
- Challenges faced in the fabrication
- Comparably high loss

1.3 Purpose of Research

Surface plasmon resonance is a quantitative electromagnetic effect that allows the sensitive detection of bio-molecular interactions directly without the need to identify fluorescent marked probe molecules or the use of color-changing substrates that enables a broad array of applications. For instance, by sensing hormone interactions with complementary antibodies, we can immediately check for the occurrence of any growth hormone in the milk. DNA and RNA assays can be performed by detecting complementary base pairing responses in real-time. One can easily determine viruses such as dengue in blood samples by detecting reactions with particular virus antigens. The study's goals include developing a PCF-based SPR sensor and numerically investigation on the proposed sensors' characteristics and behaviors. The research's specific objectives are as follows:

- To create a simple PCF-SPR sensor that can be used to solve problems like selective metal coating, liquid infiltration, etc.
- To evaluate the proposed sensors' output using a wavelength and amplitude interrogation system.
- Proposing a design that is based on external sensing and is capable of guiding a large evanescent field
- To design a fabrication friendly sensor that can be implemented practically
- To detect different biomolecule analytes, food control, virus detection, etc.

1.4 Scope of Research

This research is entirely focused on simulations. The commercial COMSOL Multiphysics program is used to examine all proposed sensors, and output is optimized using amplitude interrogation and wavelength methods. The proposed PCF SPR sensors are designed to address issues such as selective metal coating, liquid penetration, and internal sensing.

1.5 Thesis Outline

There are eight chapters in this outline. This section contains a synopsis of the next seven chapters.

Chapter 2 sets out the basic insight view of photonic crystal fiber (PCF) and its advancement in optical fiber technology. The variations of PCF-dependent fibers from the traditional are addressed in various kinds of PCFs currently in use. Detailed information also covers the structural characteristics of PCF-based fiber as per the type of sensors and different sensor types. The method is briefly presented. The algorithms used for simulating the results, and the software used are also reviewed. The accuracy of numerical methods is explained, and then the results that have already been published in a reputable journal are reproduced to validate the following process.

The PCF-SPR sensor is introduced in Chapter 3. The recorded works are subjected to a brief technical examination. For the implementation of the proposed sensor, various methods are defined. The wavelength interrogation method and the amplitude interrogation method are used to examine sensor efficiency.

Chapter 4 describes the theoretical analysis of SPR sensors and their applications. A technical overview is given, as well as information on the sensing mechanism. Sensitivity, sensor resolution, detection accuracy, different factors that control the sensitivity and linearity are all factors considered when evaluating sensor efficiency.

Chapter 5, 6, 7 describe our research work of different proposed sensors and comparative analysis of different parameters. All results obtained from the simulation of the implemented design are compared with previously published designs and are presented and described. Chapter 8 is the culmination of our thesis work and delineates the future opportunities for our line of research.

Chapter 2

An Overview of Photonic Crystal Fibers and Their Characteristics

2.1 Evolvement of PCF

Photonic-crystal fiber (PCF) is basically a classification of optical fiber which is based on photonic crystal properties. It was first investigated in 1996 at the University of Bath in the United Kingdom. A hexagonal lattice of air holes in a silica fiber was first demonstrated by Philip Russell, with a solid (1996) or hollow (1998) core at the middle where light is led. It was first proposed by Yeh and Yariv (1978) as "Bragg fibers," other configurations involving concentric rings of two or more fabrics. Silica is the major element of photonic crystal fibers. An increasing interest in producing them out of polymer has sparked research into a variety of structures, including hollow-core fibers, graded index structures, and the ring formed fibers. PCF is now finding applications in fiber-optic communications, fiber lasers, nonlinear systems, high-power processing, highly sensitive gas sensors, and other areas due to its ability to confine light in hollow cores or with containment properties not possible in traditional optical fiber.

2.1.1 Brief Description of PCF

Photonic crystal fibers are optical fibers that get their waveguide properties from very small arrangement of closely spaced air holes that run the length of the

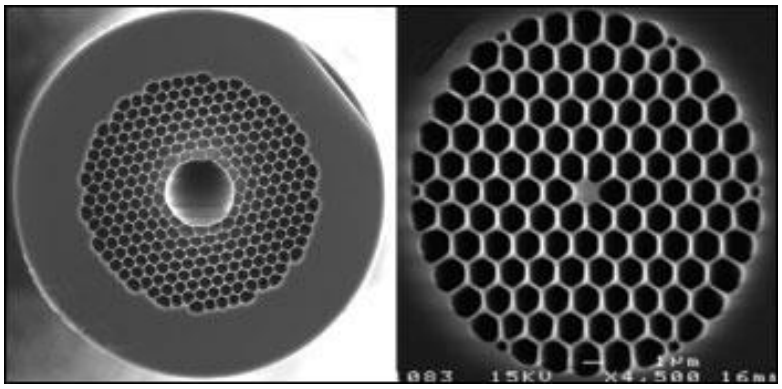

Figure 2-1: Cross-sectional view of Photonic crystal Fiber.

fiber. Such air holes may be created by solid tubes or using stacking capillary. By inserting those into a larger tube or by using a preform with (larger) holes this can be done. It is usually drawn to a cane with a diameter of about 1 mm, then into a fiber with a

final diameter of, 125 μm . Extrusion can also be used to make preforms for photonic crystal fibers, particularly with soft glasses and polymers (plastics) [3, 4]. The wide range of hole arrangements, results in PCFs with a wide range of properties. Many of these PCFs are referred to as specialty fibers.

2.1.2 Types of PCF

The Guiding mechanism of Photonic crystal fibers can be divided into two categories. Basically it depends upon the structure there are- Index-Guiding mechanism and Bandgap mechanism. The adjusted TIR mechanism is used to confine light in its nucleus.

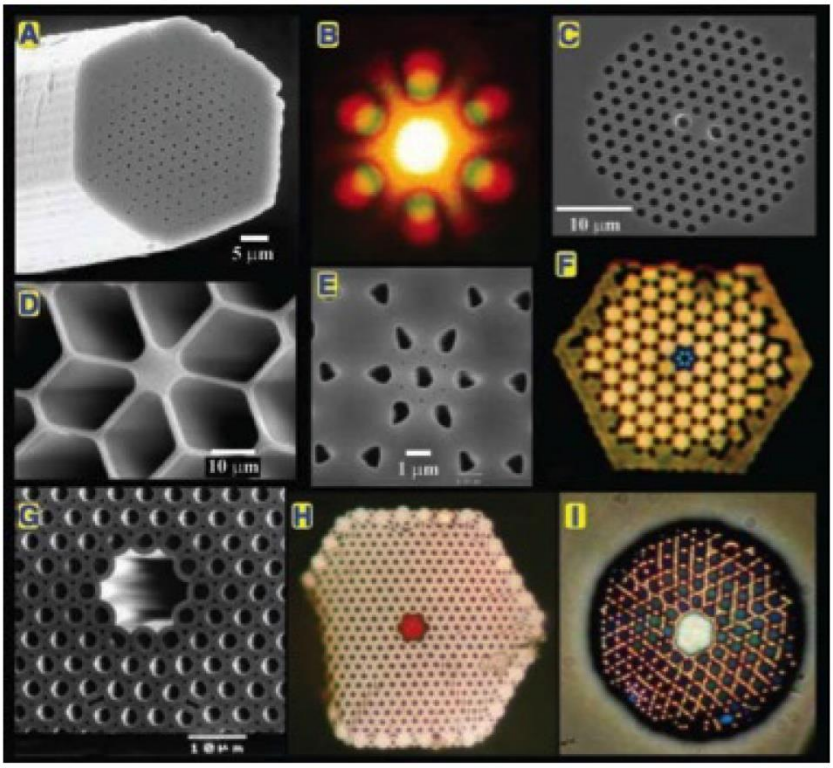

Figure 2-2: Different types of PCF.

Bandgap in Photonics (Air Guiding) Fibers are made up of periodic micro-structured elements and a low-index core. Usually, refractive index of the core region is less than that of the photonic crystal cladding. The light is directed by a mechanism that is distinct from a complete internal reflection in that it takes advantage of the photonic bandgap's presence (PBG). Air-Guiding fibers (AG fibers) or Hollow Core (HC fibers) and LIC fibers or Bragg fibers are two types of Photonic Bandgap Fibers (PBG-PCFs).

2.1.3 The distinction between PCF-based fiber and Traditional fiber

In a traditional fiber, light propagates through a medium with a high refractive index, with only evanescent "tails" passing through a medium with a low refractive index. In photonic crystal fibers, however, the nature of the fiber makes the light to disperse inside the hollow (AIR) center, with only "tails" getting into the surrounding material, resulting majority of the energy being concentrated in the air. Complete internal reflection confines light in traditional fibers, while band gap confines light in photonic crystal fibers. Since it is more localized, the latter mechanism is more stable for banding and influencing the surrounding bodies. The contrast of index between the center and the cladding is quite low in traditional fibers, but it is very strong and manageable in PCF. This is accomplished by fine-tuning the difference in optical properties between two fibers [5].

2.1.4 PCF's Light-guiding Mechanism

The first demonstration of the light guiding in a photonic crystal fiber was done inside a solid-core fiber in 1996. A rod was used to replace the central air capillary in a lattice of air capillaries [6, 7]. In materials with an energy-band structure, light guidance is an analog of the electron conduction system, which is known in solid-state physics.

The light-guiding mechanism of PCF is based on two categories: Total Internal Reflection (TIR) and Photonic Bandgap (PBG). Index-Guided PCF (IG-PCF) or High Index Contrast PCF is the name given to a light-guided PCF that uses a TIR mechanism (HIC-PCF). If the light is directed using a PBG mechanism, it is referred to as Photonic Bandgap PCF (PBG-PCF) or Hollow Core PCF (HC-PCF). IG-PCFs are characterized by the absence of a single air-hole in the structure, as well as a doped core with a high index score. The heart of PGB-PCFs is hollow. In general, by enlarging the air hole a hollow core is created in the structure's middle.

2.2 Optical Transmission Fiber: Structural Properties

This section depicts the structural properties of optical fiber. EML, confinement loss, birefringence, bending loss, chromatic dispersion, and effective area are all structural properties.

2.2.1 Material Loss Effectiveness

The critical parameter to consider for long-haul transmission in an optical fiber is Effective Material Loss (EML). Because of EML, signals are continuously dropped and cannot travel a long way. The EML is defined by the equation (2.1) [8].

$$\alpha_{eff} = \sqrt{\frac{\partial_0}{\mu_0}}\left(\frac{\int_{A_{mat}} n\alpha_{mat}\,|E|^2 dA}{2\int_{All} S_z dA}\right) \tag{2.1}$$

where $\in_0$ represents relative permeability, μ_0 represents permittivity in free space, and $n\alpha_{mat}$ represents the material's refractive index. E represents the modal electric, α_{eff} represents the bulk material absorption loss, and S_z represents the poynting vector's z-component.

EML decreases as core porosity increases because there are fewer materials within the core, resulting in less absorption loss. At fixed porosities, on the other hand, as core diameter grows, EML grows as well. Since the lower frequency light wave propagates inside the air holes of the cladding region rather than being perfectly contained in the core region, EML increases as frequency increases [9].

2.2.2 Confinement Loss

Because of their special light-guiding properties, photonic crystal fibers (PCFs) are being studied. Confinement loss is a function of PCF structural parameters, such as changing lattice pitch and the number of rings in the cladding. Since confinement loss can degrade device efficiency, it's critical to reduce its occurrence.

It is defined as the reduction caused by the standard cladding's finite magnitude [10]. The number of air holes, the depth of the air hole, the number of layers, and the pitch can all affect confinement loss. The equation that defines it is given in equation (2.2).

$$\alpha_{loss} = 8.686 \times 2\pi / c \times I_m(n_{eff}) \times 10^4 \text{ , dB/cm} \tag{2.2}$$

where f is the guiding light's frequency, c is the speed of light in a vacuum, and $I_m(n_{eff})$ is the imaginary portion of the directed mode's effective index. Many studies on PCFs with low confinement loss have already been written. For 2 μm, 1.8 μm, and 1.6 μm lattice pitches, the confinement loss is 10^{-8} dB/m, 10^{-6} dB/m, and 10^{-4} dB/m at 0.8 m middle wavelengths [11].

2.2.3 Birefringence

Birefringence is an optical property of a material whose refractive index is affected by light's polarization and propagation direction. Birefringent materials are optically anisotropic materials (or birefractive). The maximum difference between the material's refractive indices is often used to quantify birefringence.The perpendicularly polarized element can experience refraction at an angle as per ordinary refractive law and its reverse portion at a nonstandard angle when a non-polarized light beam moves through the fabric at an acute non-zero angle to the optical axis, as shown by the difference between the two efficient refractive indices called the birefringence magnitude. It is expressed as given below in equation (2.3).

$$\beta = |n_x - n_y| \tag{2.3}$$

The refractive indices of two orthogonal components of the polarization preserving wave are n_x and n_y .

2.3 Optical Fiber Sensors

Optical fiber sensing can be of many types like refractive index sensing, micro bend fiber optic sensing. This section presents the different types of optical fiber sensors based on different types of sensing technique.

2.3.1 Refractive Index Sensor

Due to benefits such as high sensitivity, lightweight, and immunity to external electromagnetic interference, several fiber-optic sensors for refractive index (RI) sensing have been developed. For RI measurement, long-period grating (LPG) and Fiber Bragg grating (FBG) is commonly used. Shifts in the reflection or transmission spectra are used to detect RI changes. This is due to the fiber gratings' response to external RI. Specialty fibers such as micro structured fiber, cladding stripped fiber, and D-shaped fiber [12, 13] are used for biochemical sensing. The thin-film coating on a fiber-optic has become a widely researched technique in the field of sensors in recent decades. It has been reported on the effects of depositing a thin, highly refractive index (RI) layer onto the cladding over the grating region [11, 14]. Since titanium dioxide (TiO_2) is one of the materials with a high refractive index under UV light, TiO_2 is considered to be a strong photo catalytic material. An interferometer-based RI sensor [15] has two beams: one serves as the reference, while the other is exposed to the external medium and acts as the sensing arm. When these two arms work together, they create an interference pattern.

2.3.2 Micro Bend Fiber Optic Sensors

One of the initial fiber optic sensors was the micro bend sensor. A mechanical perturbation of a multimode fiber waveguide induces a redistribution of light power among the fiber's many modes, to put it simply. More light is coupled to radiation modes and lost as the mechanical perturbation or bending becomes more intense. The use of a multimode optical fiber is one of the most critical characteristics of a micro bend fiber optic sensor (micro bender). Although careful experiments had previously been demonstrated vibration-induced intensity modulation of light in bent fibers [16], sensors based on micro bend loss in optical fibers were first proposed and demonstrated in 1980 [17, 18].

2.3.3 Raman Scattering with Surface Enhancement

In the literature, the mechanism of SERS's enhancement effect is still being debated. Although the mechanisms of the two primary theories vary significantly, separating them experimentally has proven difficult. The electromagnetic theory predicts the creation of charge-transfer complexes, while the chemical theory tells about the excitation of localized surface plasmons. The enhancement in the electric field produced by the surface causes an increase in the Raman signal strength for adsorbents on specific surfaces. Localized surface plasmons are excited when incident light hits the surface in the experiment. The plasmon oscillations must be perpendicular to the surface for scattering to occur; if they are in-plane with the surface, no scattering will occur. Roughened surfaces or nanoparticle arrangements are commonly used in SERS experiments due to this requirement, as these surfaces provide an area on which these localized collective oscillations can occur. Even when an excited molecule is relatively far away from the surface that hosts metallic nanoparticles that allow surface plasmon phenomena, SERS enhancement can occur.

2.3.4 Surface Plasmon Sensors

Surface plasmon resonance (SPR) is an optical technique that uses electromagnetic waves to generate light (plasmons). Surface plasmon propagation at the metal-dielectric interface is extremely sensitive to changes in the refractive index of the surface, allowing for the monitoring of ultrathin films grown very near to the metal interface. The propagation constant of the surface plasmon changes when the refractive index of the superstrate changes. This changes the coupling state between a light wave and the surface plasmon, which is visible as a shift in one of the optical wave's characteristics when it interacts with the surface plasmon. SPR sensors may be categorized as SPR sensors with angular, wavelength, strength, phase, or polarization modulation depending on which feature of the light wave interacting with the surface plasmon is measured. A monochromatic light wave excites a surface plasmon in SPR sensors with angular modulation. While a surface plasmon is excited by a collimated light wave comprising several wavelengths in SPR sensors with wavelength modulation.

2.4 Methodology and Simulation

The design methods for the SPR sensor are detailed in this section. This section also provides a theoretical overview of the model, as well as its efficiency metrics and numerical characterization to match real-world function. All numerical tools used in the development of the biosensor are also included in this section.

2.4.1 Methodologies

For the PCFs simulation, a lot of computational work has already been done. Several numerical methods are available to investigate the properties of PCFs. The Fresnel equation explains the phenomenon of light reflection from two media forming a single interface. On the other hand, according to Maxwell's equations, the electric field has basic continuity conditions across boundaries from one medium to another. The accuracy of these numerical methods is determined by a set of fundamental properties, which are described below. Full vector formulation enables the investigation of fibers with arbitrary structural parameters and refractive index contrast. Structural parameters can be modified and light guiding can be regulated depending on the applications. Among all the other PCF properties, the measurement of confinement loss is one of the most significant. The applications of PCFs have to do with light. If the loss is significant, the launching light will vanish quickly. As a result, it will be unable to move through the fiber and hence will not be suitable for any of the applications. Several well-known methods for solving modes exist, including the plane wave expansion method (PWEM), multipole method (MM), eigenmode expansion method (EME), and finite element method (FEM).

2.4.2 Finite Element Method

FEM is a common technique for numerically solving differential equations in engineering and mathematics. The standard fields of heat transfer, fluid flow, electromagnetic potential, and mass transport are typical problem areas of concern. The FEM is a computational method for solving partial differential equations of two or three variables in two or three dimensions. Over the domain, the method approximates the unknown function. The FEM approximates a solution by minimizing a related error function using various methods from the calculus of variations.

When it comes to studying micro-structured fibers, the approaches have several advantages. There are advantages to each approach, and we used the FEM method for our study because it accurately reflects complex geometry.

2.4.3 FEM implementation on PCFs

The evanescent field distribution of the proposed PCFs has been investigated. The properties of the propagating mode of the proposed PCFs are numerically investigated using the finite element method (FEM). As a boundary state, we used the circular perfectly matched layer (PML). Maxwell's equations are solved using FEM by accounting for adjacent subspaces.

2.4.4 Effective Refractive Index and PML

Perfectly Matched Layers are additional spaces or domains that absorb rather than reflect incident radiation (PML). It's a component of the model, and it will be made of various absorbing materials of varying thicknesses. There must be a matching isotropic permeability and permittivity with the physical medium outside the PML to avoid reflections.

2.4.5 Software Simulation

COMSOL Multiphysics 5.3a is a multiphysics simulation and finite element analysis program that is widely available and user friendly. It supports both traditional physics-based user interfaces and coupled partial differential equations systems (PDEs). For electrical, mechanical, fluid, acoustics, and chemical applications, COMSOL offers an IDE and a single workflow. We used this program for the simulation of SPR-based designs because it can perform modal analysis, Eigen-frequency, and finite element method (FEM).All proposed sensors are examined with the commercial COMSOL 5.3a program, also the performances have been optimized using wavelength and amplitude interrogation methods, as this analysis is entirely based on simulations.

Chapter 3
Analysis of Photonic Crystal Fiber Based on SPR

3.1 Introduction

From the Kretschmann-configuration, introduced in 1968 it is observed that there was no space between the metal layer and prism. The liquid to be identified was put outside the metal layer [19]. An inconvenience of this setup is it is unsuitable for curved surfaces. So it has very limited usage [20]. There are some problems associated with the prism-based sensors like-they are huge in size, they consist of different optical and mechanical materials which might be moving. So it causes difficulty in optimizing the sensing performance [21].To overcome this problem in 1992, Yee and Jorgenson came up with a proposition that instead of the prism as a carrier optical fiber could be used so that the SPR effect can be understood based on the Kretschmann prism structure. They created SPR fiber sensor in the subsequent year [22]. As PCF SPR sensors have numerous benefits like higher sensitivity, smaller size, lower propagation loss, real-time detection, label-free detection [23],[24] they are used in biotechnology [25], environmental monitoring[25], water testing [26] liquid and gas detection[26], biosensing [27] and so on. SPR can be classified into (A) Propagation surface plasmon resonance(PSPR) which is produced on an interface of a dielectric and thin metal layer and (B) local surface plasmon resonance(LSPR) which might be found on the rugged surface of nanostructured metal[28,29,30]. Because of the intense reliance features of SPR sensing applications on the local area's RI, it makes them ideal candidates for RI detection [31].

For the occurrence of the SPR phenomenon choosing the ideal plasmonic metal is an important step. Silver, aluminum, gold, and copper can be used for this purpose [32]. Silver can be considered as a plasmonic material as it gives lower damping loss and a sharper peak of resonance it is oxidized easily which causes problems in the sensing performance [33]. Though Aluminium can also be used as it gives higher electron density and reasonable damping loss it also faces oxidization problems [34]. Another important choice to be such a possible plasmonic metal is copper. Among all of them, gold is the plasmonic material often used because it does not have any oxidation problem and it is chemically stable [33]. In the case of PCF SPR sensors, two types of approaches related to sense can be observed. They are internal sensing and external sensing system [35]. In the case of an internal sensing system, analyte channel is formed by airholes..On the other hand in an external sensing system, the analyte channel is put on the external surface of PCF [36].

A lattice structure of square shape was proposed by Liu et al. [37] in which both right and left channels are coated with gold internally. Within the RI range of 1-1.43, this sensor gave a maximum wavelength sensitivity of 6,300nm/RIU. The amplitude sensitivity was not considered in this case. A problem with the internal sensing system is it becomes very difficult to place the metal layer on the very small-sized air hole surface, practically[38]. An internally coated high sensitivity design was proposed by Rifat et al. [39] with wavelength sensitivity of 11,000nm/RIU and the amplitude sensitivity of 1,420 RIU^{-1} but it faces difficulties in fabrication also. To

overcome this problem different externally coated structures have been analyzed. It's getting famous due to the easy fabrication and detection process [40]. Md. Ekhlasur Rahaman et al. reported a D-shaped model, in 2018 which showed a maximum wavelength sensitivity of 3000 nm/RIU and amplitude sensitivity of 241 RIU^{-1} [41]. We categorized basing on the different kinds of structure and materials that can be used in the PCF – SPR sensors.

3.2 D-Shaped Structures

In order to overcome the problem while filling the airholes with analyte and coating, the metal films D-shaped SPR based PCF sensors have been proposed as they are easier to fabricate. In August 2018 Emranul Haque and Anwar Hossain proposed a D-shaped PCF sensor dependent on SPR for RI detection of the analyte varying the range from 1.18 to 1.36. Gold was used as the plasmonic material. Both analyte sensing layers and plasmonic material gold were put on the outside of the PCF for better practical implementation [Fig 3.1(a)]. In comparison with other D-shaped structures, this modified design offered a wider range of RI detection. In order to increase the enhancement of resonance effect, gold was coated with an analyte channel. An array of air holes was arranged in a rectangular lattice to create an asymmetric core which helped to increase the birefringence. As the birefringence effect became higher the transverse electric (TE) mode of x polarization gave an evanescent field which is very large. As a result, opposed to Y polarized TE mode, there is indeed a better coupling effect with the analyte is observed. From this sensor through simulations a maximum wavelength sensitivity of 20000 nm/RIU and maximum amplitude interrogation sensitivity of 1054 RIU^{-1} were obtained. Furthermore, the sensor gave maximum wavelength interrogation resolutions of 5×10^{-6} RIU and amplitude interrogation resolutions of 16.7×10^{-6} RIU [42].

Khan S and Ahmed K proposed a D-shaped PCF sensor dependent on SPR in 2019 [Fig 3.1(b)]. In their proposed design, they used plasmonic metal gold as it is stable. They used two different diameters of airholes of 0.8 nm and 0.4 nm. Refractive index of analyte was changed from1.36 to 1.39 and a maximum WS of 66666.67 nm/RIU and AS of 1488.82 RIU^{-1} was obtained. This structure gave a resolution of 9.66×10^{-4} RIU for x polarization [43].

In 2018, Xin Chen and Li Xia proposed a D-shaped PCF SPR sensor coated by gold and an open ring channel [Fig 3.1(c)]. This design had two hexagonal rings. The ring which is situated inside consisted airholes of two different diameters denoted as $d_1 = 1.2$ μm and $d_2 = 1.5$ μm. The ring situated outside consisted of airholes of fixed diameter denoted as $d_3 = 1.8$ μm. A gold layer of thickness 50nm was placed on the inside of the open ring analyte channel to excite the surface plasmon. The maximum wavelength sensitivity of 11,055nm/RIU, high resolution of 9.05×10^{-6} RIU were found at a RI of 1.29. By observing the sensing performance it can be said that this sensor will perform better at low refractive index applications [44].

Table 3-1: Analysis of different parameters of PCF SPR sensors for D-shaped Lattice structure

Reference No.	RI Range	Maximum Wavelength Sensitivity(nm/RIU)	Maximum Amplitude Sensitivity (RIU^{-1})	Maximum Wavelength Sensor Resolution(RIU)
[42]	1.18-1.36	20000	1054	5×10^{-6}
[43]	1.36-1.39	66666.67	-1488.82	9.66×10^{-4}
[44]	1.20-1.29	11055	N/A	9.05×10^{-6}

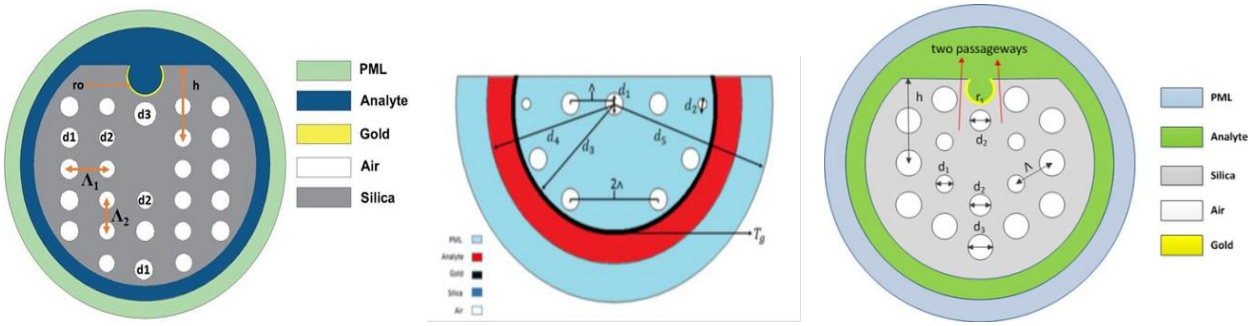

(a) [42] (b) [43] (c) [44]

Figure 3-1: Cross-sectional view of (a), Modified D -Shaped Photonic Crystal Fiber for Wider Range (b) Gold-coated D-shaped Photonic Crystal, (c) A Novel D-Shaped Photonic Crystal Fiber for Low Refractive Index Detection sensor.

3.3 Hexagonal Lattice Structures

In 2019, S.M.Abu and Tanvir Ahmed introduced a gold-coated hexagonal lattice structured SPR based PCF sensor [Fig 3.2(a)] by varying the RI spectrum from 1.33 to 1.43. With thickness of 40 nm, plasmonic material gold was placed outside the PCF sensor. An airhole was placed in the center and a number of circular air holes were organized in hexagonal structure in an annular. Maximum WS for both x and y polarization were 29500 nm/RIU and 9500 nm/RIU respectively. Maximum amplitude sensitivity for both x and y mode were 3060 RIU^{-1} and1260RIU^{-1}. Wavelength resolution for both x and y polarization were 3.39×10^{-6} and 1.05×10^{-5} respectively. In order to observe the change in loss and sensitivity thickness of gold was varied. The

performance analysis of this sensor showed that this sensor might be used for sensing biological and biochemical samples [45].

In 2020, Mahabubur Rahman and Aslam Molla introduced a PCF SPR sensor having a coating of gold. They preferred hexagonal lattice structure for an easier fabrication process [Fig 3.2(b)]. The gold layer with a thickness of 35nm was placed outside the PCF. For light confinement in the core, two airhole rings were arranged in a hexagonal structure. Two adjacent air holes were separated by a distance of $\Lambda = 2$ μm and diameter of first ring's airholes were $D = 0.5 \times \Lambda$ μm. The second ring's airholes diameter was decreased to $D_1 = 0.5 \times D$ μm so that a substantial route was created to drive light from core to metal-dielectric interface. As a result, it would assist in the activation of an evanescent field which resulted in the generation of SPW. By varying the analyte RI within the range of 1.33 to 1.37 a WS of 3000 nm/RIU to 13,000 nm/RIU and resolution of 7.69×10^{-6} RIU were found. This sensor provided an AS of 953.23 RIU^{-1}. So analytes of liquid nature within this range can be detected easily [46].

In 2016, A.A.Rifat proposed a gold-coated PCF SPR sensor [Fig 3.2(c)] in which both the plasmonic material and the layer to be sensed were placed outside of the metal layer. This design consisted of 3 rings of air holes which were positioned hexagonally. Two small-sized airholes were also used. To excite the metallic surface apart from the tiny airholes two opposite holes were removed so that evanescent field could pass through the gap created. The wavelength and amplitude sensitivities of the sensor were 1000 nm/RIU and 118 RIU^{-1}, respectively. This sensor gave a sensor resolution of 1×10^{-4} RIU and 8.5×10^{-5} RIU concerning the wavelength and amplitude interrogation method. The performance of this sensor allowed it to be used for biochemical and biological analytes detection [23].

Table 3-2: Analysis of the different performance of PCF SPR sensors for Hexagonal lattice structure

Reference No.	RI Range	Polarization	Maximum Wavelength Sensitivity(nm/RIU)	Maximum Amplitude Sensitivity (RIU^{-1})	Maximum Wavelength Sensor Resolution (RIU)
[45]	1.33-1.43	x-polarized	29500	3060	3.39×10^{-6}
		y-polarized	9500	1260	1.05×10^{-5}
[46]	1.33-1.37	N/A	3000-13000	953.23	7.69×10^{-6}
[23]	1.33-1.37	N/A	1000	118	8.5×10^{-5}

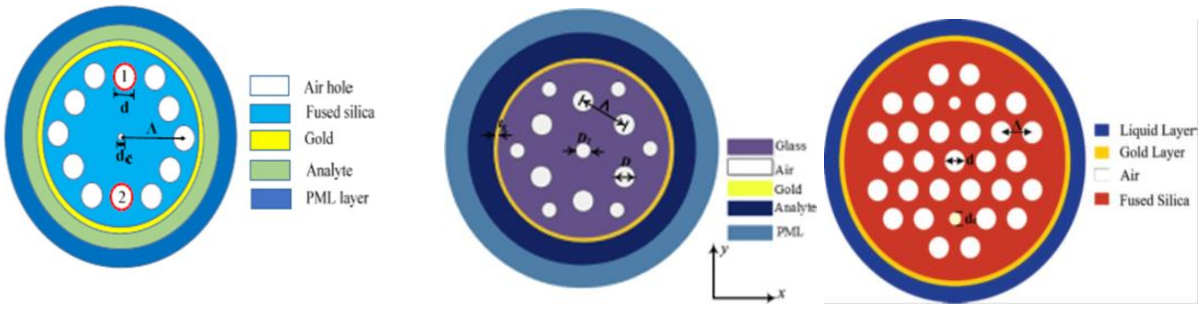

(a) [45] (b) [46] (c) [23]

Figure 3-2: Cross-sectional view of (a) hexagonal lattice PCF with a ring airhole, (b) hexagonal lattice PCF biosensor based on SPR, (c) 3-ring hexagonal PCF biosensor based on SPR.

3.4 Circular Lattice Structures

In 2018, Khalek, M.A., Chakma, S., introduced a gold-coated PCF SPR sensor having a circular lattice[Fig 3.3(a)].In order to carry out the investigation, they covered a wide range of optical spectrums of 0.48 µm to 1.10 µm. This design consisted of two layers of airholes. In each layer two airholes were absent. In addition, the second ring had two small air holes and the center had one big air hole. For the investigation purpose they denoted p as the distance between center to center, r_c as the radius of the center airhole, $r_2=r_c$ as the radius of the smaller airholes, r_1 as the radius of the rest of the airholes. A thickness of 35nm of a gold film was placed outside the fused silica. The single-core was preferred in this design because it could give high performance. The suggested framework revealed maximum sensitivity of 9000 nm/RIU using the wavelength interrogation method, and a maximum sensitivity of 318 RIU^{-1} using the amplitude interrogation method. Furthermore, in sensing ranges between 1.34 and 1.37, it gave the maximum sensor resolution of 1.11×10^{-5} [47].

In 2020, Q.M. Kamrunnahar, and Jannatul Robaiat Mou introduced a dual-core circular lattice PCF SPR sensor [Fig-3.3(b)]. An investigation was done within the range of 450 nm to 1150 nm which corresponds to the visible to near-infrared region. The structure of this design was done in such a way so that dual-core could be created. So, they placed an airhole in the center which was accompanied by two airhole rings. As a result, the structure also reduced the distance between the metal surface and the evanescent field. In order to get light confinement properly, they removed two airholes in two opposite directions in the first ring. The second ring includes six small air holes in two opposite directions for efficient evanescent field penetration and engagement with free electrons on surface of the metal. Gold layer of thickness 35nm was chosen for this design. This sensor offered a maximum WS of 11200nm/RIU and an AS of $503.037RIU^{-1}$. Resolution of 8.92×10^{-6} RIU for wavelength sensing in RI range of 1.33 to 1.44 was found [48].

In 2017, Hasan, M., Akter, S., introduced a PCF SPR sensor that had a two-layer circular lattice structure [Fig-3.3(c)]. As a plasmonic material, gold layer of a thickness of 40nm was used and it

was placed outside the PCF structure. The layer to be sensed was placed in the outermost layer so that the fabrication process could become easier. The proposed design consists of two airhole rings but two airholes were absent in the first ring. This was done so that an increment in the birefringence could be possible. Air holes were positioned in a 60 degree anticlockwise progressive rotation for first ring and 30 degree anticlockwise progressive rotation to form the second ring. It is indeed important to note that the second ring's two air holes, as well as the central hole, were all very small. The explanation for this is that the evanescent electromagnetic field circulates on two opposite sides of the PCF, allowing surface electrons to be easily stimulated. The proposed sensor gave a maximum wavelength sensitivity of 2200 nm/RIU and maximum amplitude sensitivity of 266 RIU^{-1} using the wavelength interrogation method in the sensing range between 1.33–1.36 and amplitude interrogation method. Maximum sensor resolution of 3.75×10^{-5} RIU was obtained [49].

Table 3-3: Analysis of the different performance of PCF SPR sensors for Circular lattice structure

Reference No.	RI Range	Maximum Wavelength Sensitivity(nm/RIU)	Maximum Amplitude Sensitivity(RIU^{-1})	Maximum Wavelength Sensor Resolution(RIU)
[47]	1.34-1.37	9000	318	1.11×10^{-5}
[48]	1.33-1.44	11200	503.037	8.92×10^{-6}
[49]	1.33-1.36	2200	266	3.75×10^{-5}

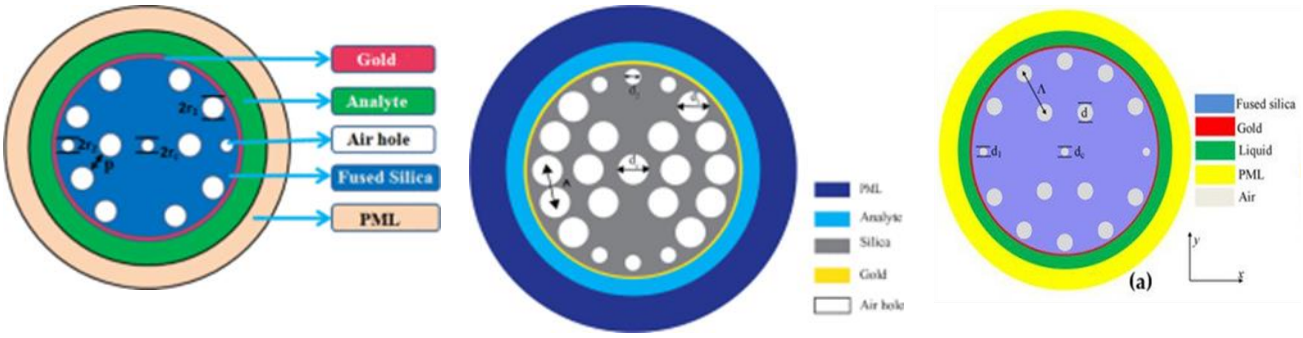

(a)[47] (b)[48] (c)[49]

Figure 3-3: Cross-sectional view of (a) a gold-coated circular PCF- SPR sensor, (b) dual-core circular lattice SPR-PCF, (c) two-layer circular PCF-SPR biosensor.

3.5 Square, Spiral, Trapezoidal Lattice Structure

Md. Nazmul Hossain, Md. Ferdous proposed a PCF SPR sensor in 2018 for identifying the unknown analytes[Fig-3.4(a)]. Gold was chosen as the plasmonic material because of its stability. The suggested sensor was composed of symmetrical square air holes which were double-layered. Hence more evanescent field was created by using a tiny airhole in the center. Compared to the other air holes present in the double layers the center air hole was chosen smaller. They denoted p=2μm, d_c = 0.4 μm, d=0.8 μm, d_g = 42 nm as the pitch size, a diameter of the center air hole, a diameter of common airholes, and thickness of gold layer respectively. To increase sensitivity the proposed sensor was designed in a way so that there was a possibility of coupling between both core and SPP mode. For refractive index of 1.37 and 1.38 silver and gold were used to analyze the sensor's performance. It was found that gold gave more amplitude sensitivity compared to silver. Hence gold was chosen as plasmonic material. The maximum AS was 442.11 RIU^{-1} with the highest sensor resolution of 1.66×10^{-5} using the amplitude interrogation method. Wavelength sensitivity was 6000 nm/RIU using 4the wavelength interrogation process [50].

In 2018, Md. Rabiul Hasan proposed SPR sensor depending on dual-polarized spiral PCF [Fig-3.4(b)]. In order to make the fabrication process easier, gold was selected as plasmonic material and it was put outside of the PCF. This PCF consisted of three rings and six arms. It's worth noting that the first ring was lacking two air holes along horizontal axis to establish birefringence asymmetry. As a result coupling of x or y polarized mode and SPP mode increases which leads to a better sensing performance. The central air hole had a diameter of $d_c = 0.2\times\Lambda$ and the remaining air holes had a diameter of $d = 0.65 \times \Lambda$, with a value of Λ= 2 μm. By varying the RI range from 1.33 to 1.38, a maximum wavelength sensitivity of 4600 nm/RIU and amplitude sensitivity of 420.4 RIU^{-1} were found in y polarized and maximum wavelength sensitivity of 4300 nm/RIU and amplitude sensitivity of 371.5 RIU^{-1} were found in the x polarized mode [33].

In 2019, Suoda Chu and K. Nakkeeran introduced a sixfold PQF with trapezoidal analyte channel dependent on SPR incident [Fig-3.4(c)]. They designed a trapezoidal analyte tube, in contrary to conventional D-shaped PCF, to examine position of sample liquid height inside channel and to discuss fabrication method functionality. Though this design was a common D-shaped structure it included a channel that was trapezoidal in shape. Because of its unique design, it has some benefits like low confinement loss, flattened zero-dispersion profile over wider range of wavelengths. The design consisted of four layers of air holes. They denoted d = 1 μm, Λ=2 μm, as diameter of airhole and pitch respectively. They also denoted d_a=2 μm, W_{top} = 5.62 μm, W_{bottom} = 3.12 μm as height of the trapezoid channel, width of top wider side, and bottom shorter side respectively. A gold layer of thickness 50nm was used in this design. The suggested sensor gave a maximum RI sensitivity of 4400 nm/RIU, 6100 nm/RIU, 8000 nm/RIU, and 17000 nm/RIU respectively, for the analytes RI range of 1.44 to 1.57, 1.41 to 1.51, 1.40 to 1.49, and 1.40 to 1.44[51].

Table 3-4: Analysis of the different performance of PCF SPR sensors for Square, Spiral, and Trapezoidal lattice structure

Reference No.	RI Range	Polarization	Maximum Wavelength Sensitivity(nm/RIU)	Maximum Amplitude Sensitivity (RIU^{-1})	Maximum Wavelength Sensor Resolution(RIU)
[50]	1.36-1.39	N/A	6000	442.11	1.66×10^{-5}
[33]	1.33-1.38	x-polarized	4300	371.5	2.69×10^{-5}
		y-polarized	4600	420.4	2.37×10^{-5}
[51]	1.41-1.52	N/A	6100	N/A	1.64×10^{-5}

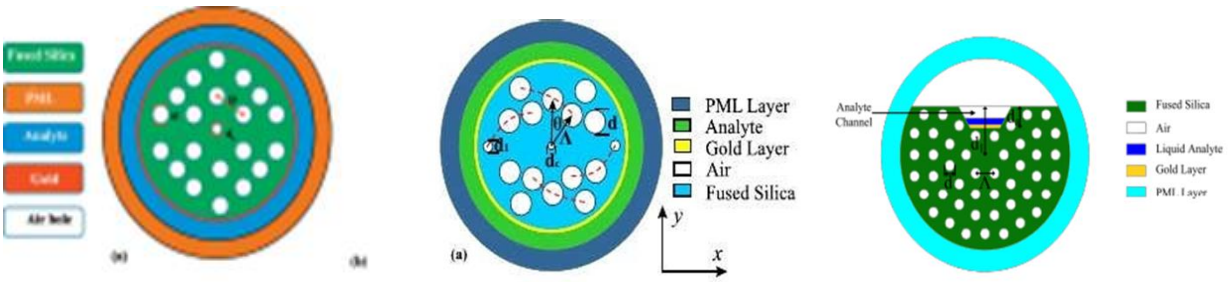

(a) [50] (b) [33] (c) [51]

Figure 3-4: Cross-sectional view of (a) a gold-coated square lattice PCF-based SPR sensor, (b) Spiral core SPR-PCF, (c) Trapezoidal lattice photonic crystal fiber biosensor.

3.6 PCF SPR Sensors Based on Bimetallic Materials

In December, 2020, Han Liang and Tao Shen proposed a D-shaped PCF Sensor-based SPR in which they used silver as the plasmonic material [Fig 3.5 (a)] and the sensor performances were observed by coating the sensor with grapheme layer and zinc oxide layer consecutively. The polished surface is coated with a material, which allows the manufacturing of the sensor simple and achieves its objectives of reinforcing materials throughout hole and coating on hole wall. By varying RI of the analyte within range 1.37 to 1.41, the maximum sensitivity of 6000nm/RIU and resolution of 1.667×10^{-5} were found respectively [52].
In 2015, Ahmmed A. Rifat and G. Amouzad Mahdiraji introduced a PCF SPR sensor in which they used silver as the plasmonic material [Fig 3.5(b)]. Graphene was used for the coating to prevent oxidation. Surface plasmon waves were created by placing liquid-filled cores near a metallic channel. In this design to create a straight line with central metal channel, two similar cores were stuffed with liquid of high RI. They used a triangular lattice and distributed the airholes accordingly. They denoted $\Lambda = 1.90$ μm and $d = 0.5\ \Lambda$ as pitch and airhole diameter. They chose the same value of $d_1 = d_c = 0.8\ \Lambda$ for airhole core, metallic channel diameter. The inner surface of the fiber's core structure is made up of graphene sheet on the top of thin silver layer. They denoted t_{ag}=35nm and t_g=3 nm as the thickness of silver and graphene layer. The suggested sensor gave a maximum amplitude sensitivity of 418 (RIU^{-1}) with a resolution of 2.4×10^{-5}RIU. Maximum wavelength sensitivity of 3000 nm/RIU in the sensing spectrum of 1.46–1.49 was achieved [53].

A PCF SPR sensor with gold and grapheme bimetallic layers was proposed by Junbo Lou in 2019 [Fig 3.5(c)]. In this design, the airholes situated in the cladding region were arranged hexagonally.To create a hexagonal design with an eccentric core, fiber core was lifted.. They denoted Δ,t, Λ, d as the gold thickness, the graphene thickness, pitch, and diameter of the airhole respectively. After adding graphene, an increment in the average sensitivity from 2938.86 to 5171.51nm/RIU was observed and the maximum sensitivity was found to be 8600 nm/RIU. By varying RI range from 1.33 to 1.37 it was seen that if the thickness of the graphene layer was increased the SPR phenomena would become weaker [54].

A thin TiO_2 coating with enhanced RI, non-toxicity, and environmental stability characteristics is commonly used between Au and glass to solve gold adhesion problems [Fig 3.5(d)]. Saiful Islam et al. published a paper in June 2019 in which they introduced a miniature, simple, and highly SPR-PCF biosensor. A thickness of 30nm was used for gold layer and a layer of titanium dioxide (Ti was selected for prevention of adhesion of gold. After carrying out the investigation optimum value for each parameter was found. They were $d_c = 0.125\Lambda$, $d = 0.67\Lambda$, $d_1 = 0{:}09\Lambda$, $\Lambda = 1.65$ μm, $\Lambda_1 = 1.16$ μm, $n_c = 5$, $t_g = 30$ nm, and $t_t = 5$ nm. From this suggested sensor a maximum wavelength sensitivity 25,000 nm/RIU and a maximum amplitude sensitivity of 1,411 RIU^{-1} were found [55].

Table 3-5: Analysis of different parameters using Bimetallic Material for PCF SPR

Reference No.	RI Range	Bimetallic Materials	Maximum Wavelength Sensitivity(nm/RIU)	Maximum Amplitude Sensitivity (RIU^{-1})	Maximum Wavelength Sensor Resolution(RIU)
[52]	1.37-1.41	Silver +Graphene/ZnO	6000	N/A	1.667×10^{-5}
[53]	1.46-1.49	Silver+Graphene	3000	418	2.4×10^{-5}
[54]	1.33-1.37	Gold+Graphene	8600	N/A	N/A
[55]	1.33-1.38	Gold+TiO_2	25000	1411	4×10^{-6}

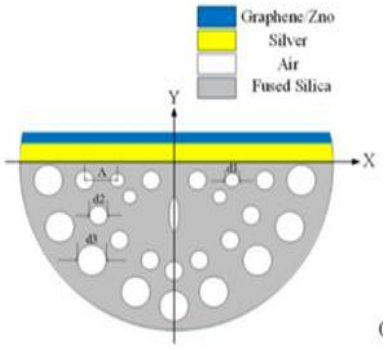

(a)[52]

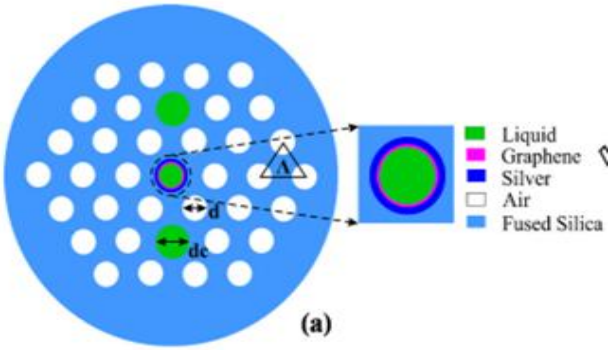

(b)[53]

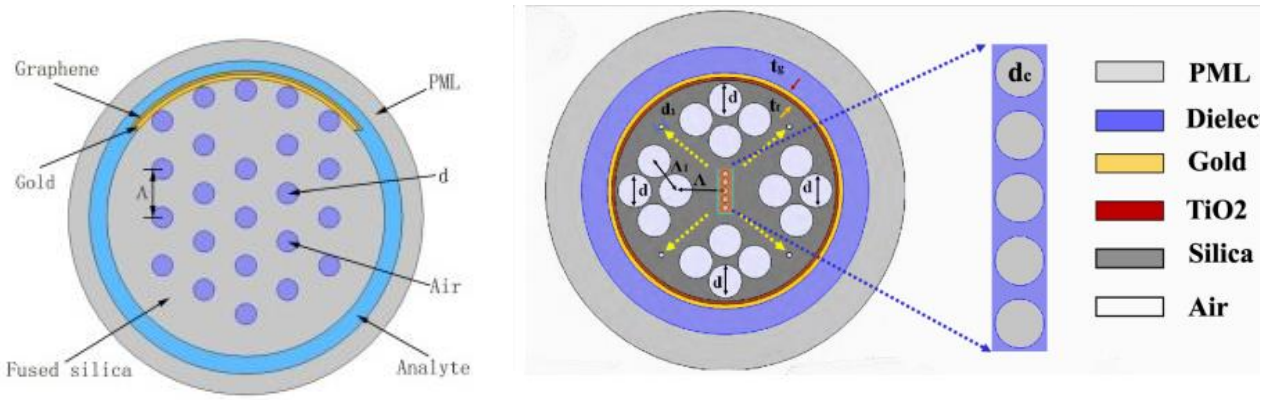

(c)[54] (d)[55]

Figure 3-5: Cross-sectional view of (a) a D-shaped Silver and Graphene /ZnO metallic layer-based PCF SPR sensor, (b) Hexagonal core Silver and Graphene metallic layer-based SPR-PCF, (c) Gold and Graphene layer-based photonic crystal fiber biosensor, (d)Gold and TiO_2 based PCF-SPR sensor.

3.7 Conclusion

To improve sensing performance of PCF SPR sensors, researchers explored different designs of the sensors. Their targets were to get maximum sensitivity, low confinement loss, practical feasibility to implement the sensor. Observing the papers we got an idea about which type of structure gives higher sensitivity, which plasmonic material can be used to improve the sensing performance. The perfectly matched layer is used outside so that light can't leave the fiber. Fused silica is used because of its ultra-low thermal sensitivity. Comparing to the internally sensing approach, the externally sensing approach gives better sensitivities of both amplitude and wavelength. Compared to hexagonal lattice structure, the circular lattice structure gives better sensing performance as light is confined more in this case. D-shaped lattice gives better sensing performance but implementing it practically is a challenging matter. Using smaller airholes passes more light to be limited to core. On the contrary, energy is transferred from core to SPP mode if larger air holes are used. The leakage of light from the core to cladding depends on the pitch. So it should be kept low. Gold, silver are chosen as the plasmonic material. Due to chemical stability of gold, it is often preferred to silver. Addition of another material like TiO_2, graphene with plasmonic material increases sensing performance of a sensor.

Chapter 4

Surface Plasmon Resonance and Theory Analysis of Surface Plasmon Resonance Based Biosensor

4.1 Introduction

The term “SPR” endures for Surface Plasmon Resonance which introduces an optical property. Basically, it executes the surface charges which are propagating in the metal-dielectric junction due to the confinement of the electromagnetic field after an oscillation of electrons has occurred. SPR based biosensors have already played vital roles in the field of bio-sensing applications, food controlling, medical technologies, chemical, and physical sectors, etc. and now it is gaining too much popularity because of its sensory characteristics. This SPR phenomenon occurs because of the evanescent field which is dealt with the proliferation of light in the core through the cladding region and for that electric oscillations take place in the interface.

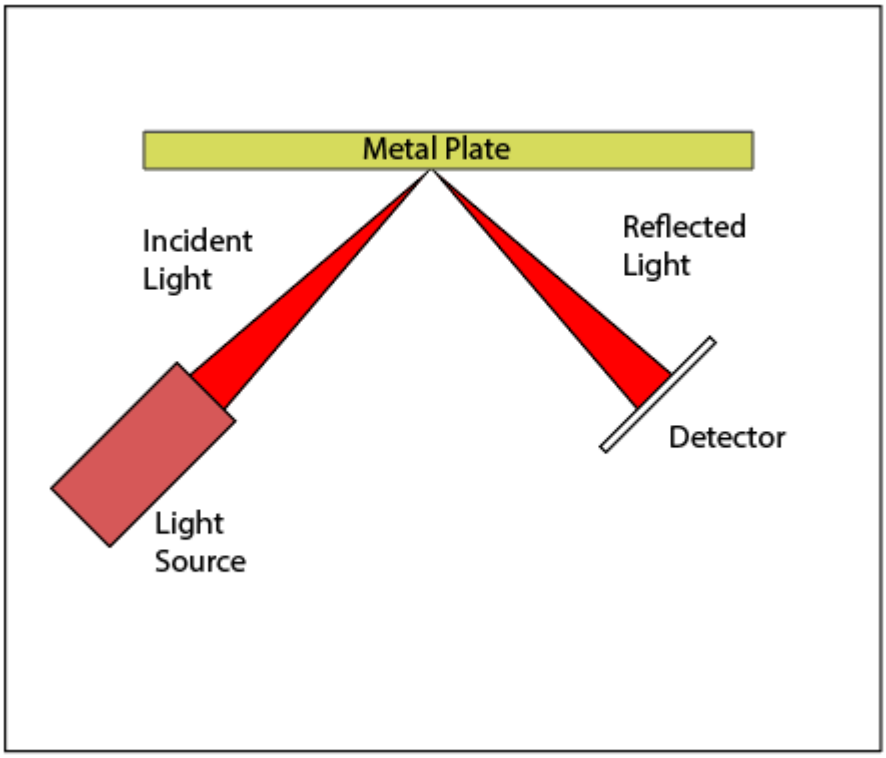

Figure 4-1: Occurrence of SPR.

4.2 Background History of SPR:

The surface Plasmon concept was first investigated by a researcher named Ritchie (1957). Later in the sixties, two configuration ideas have discussed elaborately as it encompasses the light guidance property of SPR sensor [56-58].

Based on the SP's idea of using the **Attenuated Total Reflection** (ATR) prism-based SPR Otto design, Otto (1968) stated that the prism and the plasmon metal layer were separated by a dielectric (sample) medium. So a finite gap in the middle of the prism and metallic layer, the sensing technique becomes quite difficult to achieve. Another upgraded configuration is Kretschmann. Kretschmann setup is a different operable configuration in which light is produced with a glass prism; focusing on a metallic film and then focusing on it responsive. This configuration detects the mutual waving of the free electrons called surface plasmons. Both techniques are getting tremendous admiration in the field of SPR biosensors. The SPR application is demonstrated first by Nylander and Liedberg [59] .He used the characterization of thin films [60-61] and prism coupling for biochemical analyte detection technique [62-64]. In the 1980s, SPR and similar techniques were applied to thin-film examinations in conjunction with biomolecule interactions [60]. These procedures add flexibility in real time, without classifying and in an extended way to analyze the interactions between immobilized receptors and analytes in solutions. There are various ways to afford information on the specificity, kinetics, and affinity of the interaction or concentration of the analyte can be exhibited by analyzing binding rates and binding frequency. Resonance occurs when the electromagnetic wave and surface plasmon wave are generated by cause of the penetration of light in the interface.

In the early 80s, one of the researchers named Pharmacia became interested in the SPR sensor and started to research this sensing mechanism. Pharmacia created “Pharmacia Biosensor AB” in 1984 to design, manufacture and market a functional SPR-machine, [65-66] and the manufacture of a silicone microfluidic cartridge have taken the easy-to-use SPR-machine closer to being a reality [67].

Due to its large size, it is not suited in remote sensing application which includes different optical and movable parts. The large peak wavelength shift can be spotted by a very meager variation of an analyte’s RI. Very slight change of analyte’s RI can be observed from the broad peak wavelength shift. Greater sensitivity results in greater precision in the identification of an unknown analyte [68]. Plasmonic (sensing) material performs a decisive role in the efficiency of SPR sensors. It is operated as a sensing material for the complete surface plasmon resonance phenomenon. It guides the incident light from the cladding portion to the metal-dielectric surface to produce the surface plasmon wave which results in the surface plasmon polariton. Silver, copper, Gold (Au), etc are treated as plasmonic material in the SPR sensor. Each of them has its own characteristics. Silver (Ag) is less chemically stable and less optical damping with a sharp resonance peak. But it has an oxidization problem in an aqueous environment and for that there strikes some restriction while using in a broader sensing technique. A thin layer of graphene can be implemented as a safer alternative in this matter, but it is very difficult to produce and costs

are relatively higher in number. It will be also difficult to fabricate further. Gold is also chemically stable as a consequence it is not easily oxidized in an aqueous state. It also shows high sensing performance in any environment [69]. Many research works are going through to intensify the sensing performance of SPR biosensors.

4.3 Literature Analysis

As SPR sensors are connected with different plasmonic terms such as surface plasmon wave (SPW), surface plasmon polariton (SPP), evanescent field, etc. We will discuss it all in the following section here.

4.3.1 Definition of Surface Plasmon Wave (SPW)

It is the key result of matching in the array of frequency between the evanescent field and complimentary electrons. It propagates along the surface of a plasmonic material. In such angles of incidence, a section of the light energy coupled through the gold coating induces a resonant oscillation of the conduction electron resulting in a surface plasmon wave at the sample and a gold surface interface. The waves are in a form of a transverse wave (TW) which is normal to the surface. It is because surface plasmons have only an electrical field portion, which is common to the surface. P-polarized light is needed to meet the boundary conditions that are necessary to stimulate SPR.

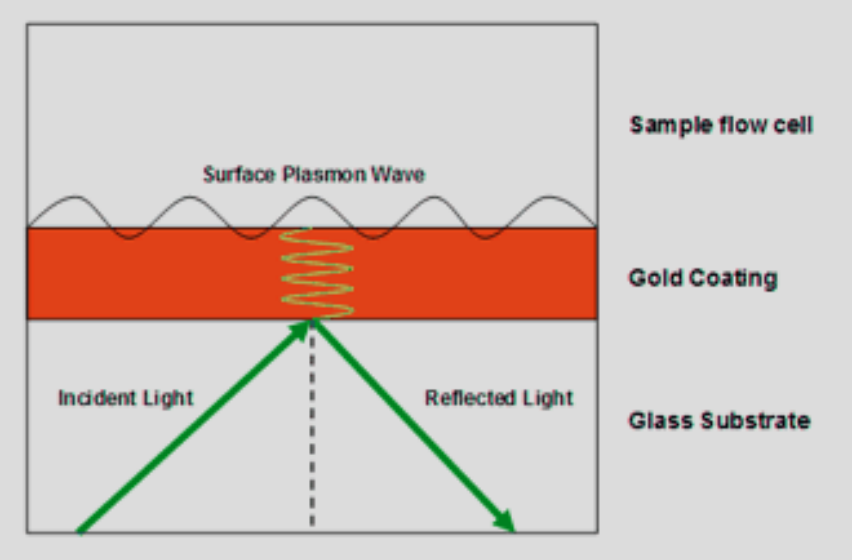

Figure 4-2: Surface Plasmon Wave (SPW).

SPW is symbolized by the propagation constant given in equation (4.1).

$$\beta = \frac{\omega}{c}\sqrt{\frac{\varepsilon_M \varepsilon_D}{\varepsilon_M + \varepsilon_D}} \tag{4.1}$$

Here ω stands for angular frequency, c signifies the speed of light in vacuum, and ε_M, and ε_D are the dielectric permittivity of metal and dielectric medium. The constant propagation of surface plasmon waves is higher than the constant propagation of light in the dielectric medium. So, the surface plasmon cannot be excited with normal light. So it is treated as the main basement of SPR.

4.3.2 Theory of Surface Plasmon Polariton (SPP)

It is the activity of electromagnetic oscillations in the junction enclosed by a metal and dielectric medium. The mechanism is similar to the way of light governed by an optical fiber. The wavelength of SPPs is less than that of the incident light (photons). SPPs may therefore have tighter spatial confinement and greater local field intensity. The SPP extends along with the interface until the energy is released either in metal concentrations or in other forms (such as into free space) [70].

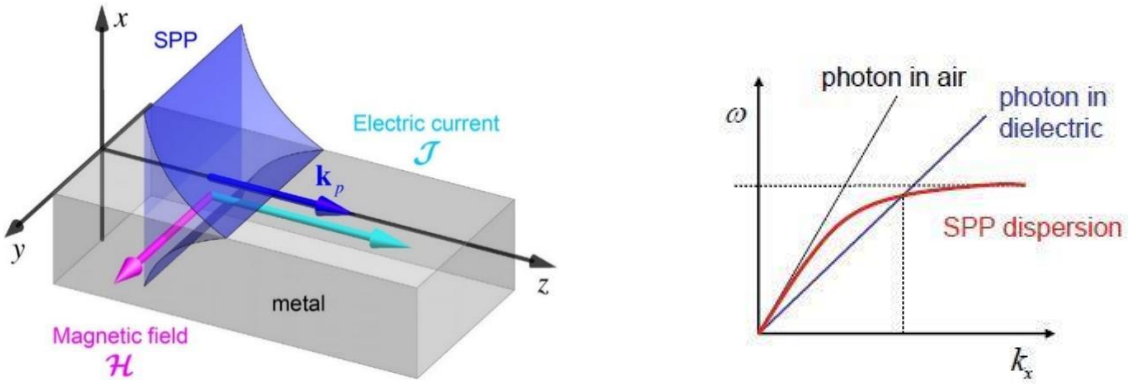

(a) **(b)**

Figure 4-3: (a) Generation of Surface Plasmon Polariton. (b) The curve showing the dispersion relation.

Both electrons and photons can be agitated by this mode. Excitation of the electrons is formed by firing electrons into the bulk of the metal. As the electrons spread, energy is transferred into the bulk plasma. To excite a photon, the frequency and momentum must be similar. However, for a certain frequency, a free space photon has less momentum than that of an SPP, since the two of them have different dispersion relations. Because of the deficiency of momentum, a free-space photon from the air cannot bind directly to an SPP.

4.3.3 Evanescent Field

The sensitivity of such an SPR sensor relies on the evanescent field which displays a core area and causes free electrons to have oscillated. A transient field is constructed as the light passes through a photonic crystal fiber core. The evanescent field interacts with the PCF-coated plasmonic material that activates SPW. It is an electro-magnetic field oscillating, not as an electromagnetic pulse, but the energy of which is spatially concentrated near the source. A distinctive characteristic of an evanescent field is that in that area there is no net energy flow. Since the average Pointing vector provides the net flow for electromagnetic energy, this means that on average for a full oscillation period, the Pointing vector in those areas is zero.

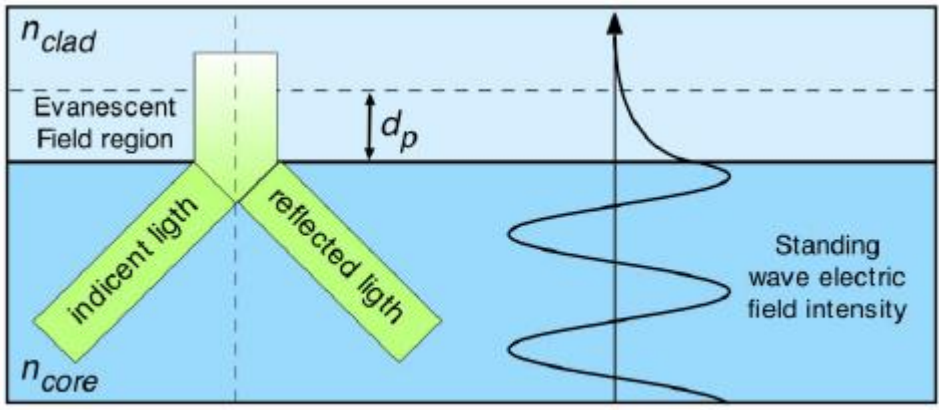

Figure 4-4: Generation of Evanescent Field.

Optical fibers are always assumed to use the whole internal reflection to direct light energy via the fiber. But usually, a section of the internally reflected wave travels a short distance far beyond the core boundary into the optical cladding. That is the evanescent wave property that can be utilized by extracting the fiber cladding to permit the evanescent wave to spread beyond the core barrier. The drawbacks of evanescent fields are that it is apparent that one must operate very near the surface, establish patterns just by using the range of incident angles beyond the critical angle for whole internal reflection, and allow for the strong difference in penetration depth as a result of the incident angle (which, on the other hand, allows 3D shaping of the evanescent field) [71]. Taken together, these issues ultimately reduce the outlines that can be achieved holographically in the near field and require the implementation of new algorithms.

4.4 Surface Plasmon Excitation through Light Mechanism

We realize that resonance occurs when the phase-matching condition is amused between the core mode and spp mode. And if the condition is fulfilled then only the excitation of surface plasmon will be possible. For the same frequency propagating in the surface for any wavelength, the SPs have a longer wave vector than light waves [72]. The wave path of light can be modified to fit the wave vector of the SP by delivering it through the metal from a medium with a RI higher than the RI of the range at the boundary where the SP is to be excited. The following figure imprints the graphical capture of a surface excitation in the interface of a metal-dielectric medium.

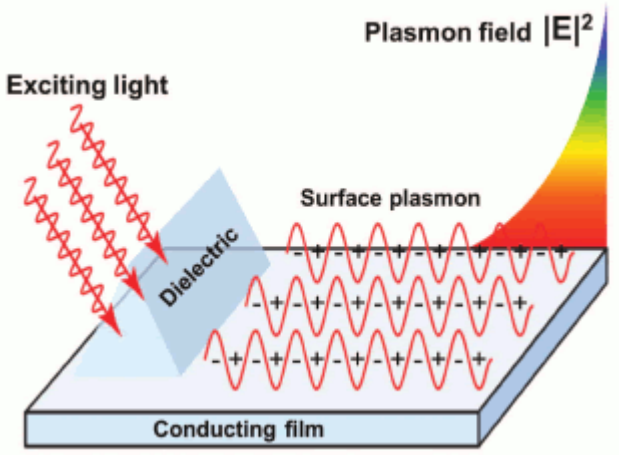

Figure 4-5: Surface Plasmon Excitation through Light.

There are different ways for exciting an SPR phenomenon such as coupling of light through a prism, grating, and waveguide. Initially, Kretschmann-Raether reported a prism coupling that was frequently used to stimulate the SPR sensors [73].

4.5 Prism Based SPR Configuration

There are several methods for generating surface plasmon resonance. One of the common ways is by using prism coupling. Kretschmann and Raether first explored prism-based SPR sensors in early 1968 [73].This architecture is portrayed in Figure 4.6, where the setup uses a high RI prism (glass) with such a metal layer on the bottom of the prism and a sample from the other side of the metal layer. SPR sensor resonance based on prism occurs when the constant penetration of the evanescent wave and the constant propagation of surface plasmon wave is the

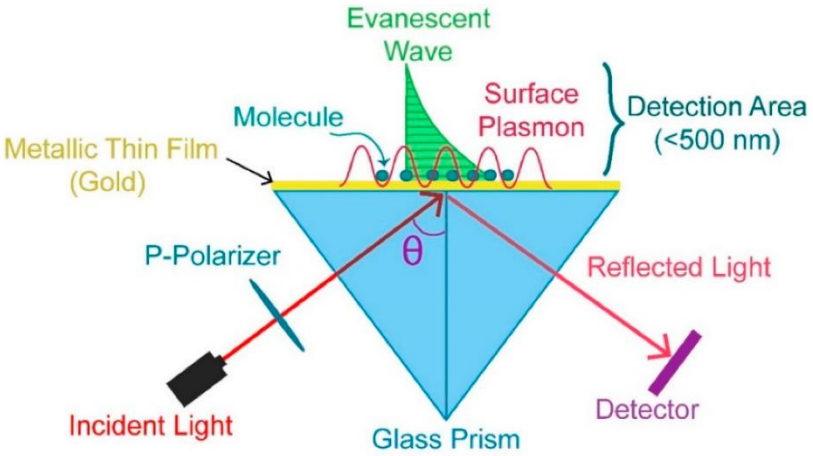

Figure 4-6: Prism based SPR Configuration.

same. As per the Kretschmann-setup propagation constant of the evanescent wave is denoted by equation (4.2).

$$k_{ev} = k_g \, sin\theta = \frac{\omega}{c}\sqrt{\varepsilon g} sin\, \theta \tag{4.2}$$

As per the formula of Maxwell's equation, *ksp* of surface plasmon waves that inseminate along the metal-dielectric interface can be signified by equation (4.3).

$$k_{sp} = \frac{\omega}{c}\sqrt{\frac{\epsilon_m \epsilon_s}{\epsilon_m + \epsilon_s}} \tag{4.3}$$

where $\epsilon_m$indicates the dielectric constant of the dielectric medium or sensing medium and ϵ_s indicates the dielectric constant of the metal. The prism-based SPR sensor is therefore large in scale, which involves many optical and electrical components. There is also sophisticated sensor architecture, and for remote sensing applications, this SPR sensor is inadequate in nature.

4.6 SPR Sensor in Optical Fiber

As the prism coupled SPR sensors have some drawbacks and are bounded to remote sensing, SPR sensors based on optical fiber technology is attaining immense admiration recently which was first proposed by, R. C. Jorgenson et al. in the year of 1993 [74]. The main mechanism is that the light spread in the core and the cladding in the pattern of modes are fully reflected within and outside the conserving interfaces. The core and the outer cladding interfaces have been bound by different modes at various angles. So, for realizing the SPR sensor in optical fiber, many effective attempts have been made successfully in the optical fiber sensor. There has been notable progress recently with context to SPR, SPR-located and photonic crystal fiber, and new types of SPR-based optical fiber sensors in the research community have attracted growing attention. Consequently, all datas in these areas cannot be verified. Details and some impressive reviews of some of the studies can be found in the following references. [75-78].

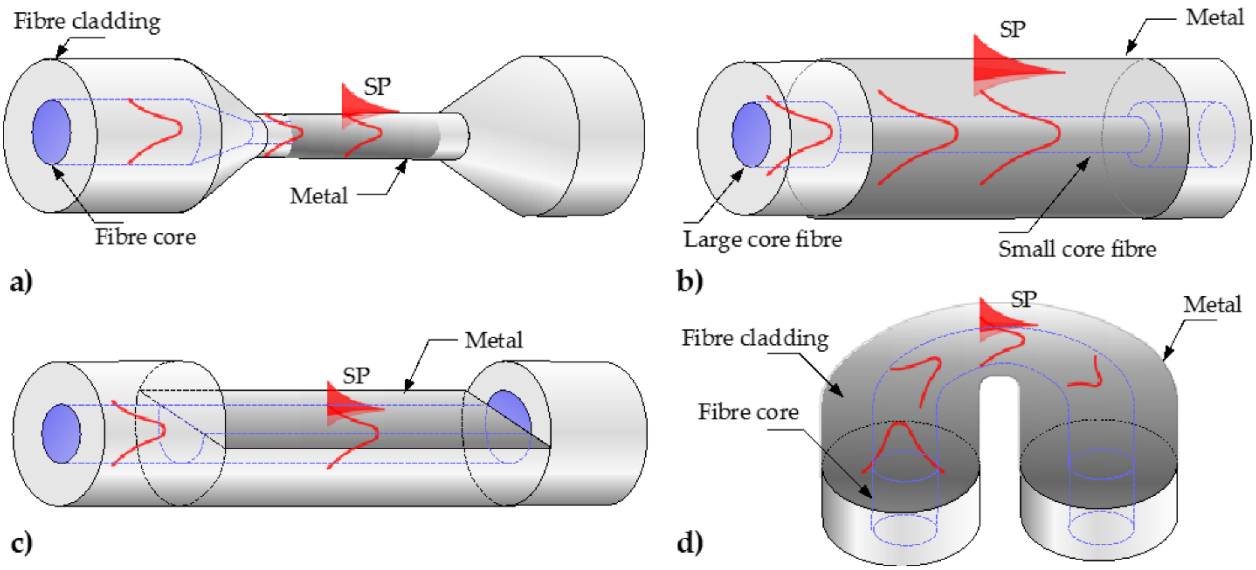

Figure 4-7: Schematics of geometry-modified optical fiber SPR sensors implemented on a side of an optical fiber: (a) Tapered fiber SPR probe; (b) Hetero-core structure; (c) D-shaped SPR probe; (d) U-shaped SPR probe.

A thin film gold-coated fiber or by imposing another active plasmonic material and the phase-matching condition is satisfied through it. It is not possible for SPR to be excited on the surface of the fiber because the strength of the evanescent field resulting from TIR at the core cover interface might be too fragile for the region and interfere with the metallic layer. A weak evanescent field leads to a higher core power fraction which means that no SPP mode can result in a light that can occur on the plasmonic layer. As we know that an evanescent field with a weak configuration will be responsible for a higher core power fraction resulting in a light unable to the incident on the plasmonic layer, no surface plasmon polariton will occur in the interface. For solving the issues, a coupling mode can be implemented to excite the SPR sensor from light propagating core mode to the cladding modes. Therefore, without deformations or modifications, there are no SPR sensors placed on the regular single-mode fiber. Current methods, which are implemented until now, are based on the stimulation of SPR by the improvement of the evanescent field closed to the alloy. SPR can be excited from the evanescent field caused by the reflection in the core-mode at the core interface if it is strong enough to reach the metal layer. The metal layer can be placed close to the core covering interface if the cover is removed partially or totally. In general, D type optical fiber may do this having a deep cut in the cladding or by bending the fiber and polishing one of the sides of the fiber or using non-standard fiber [79]. The use of a tapered fiber is another accepted solution in this case [80].

In certain ways, the plain metal layer may be replaced with nanoparticle layers. The unclad part is affixed on both ends by translation stages. The core of the unclad fiber is heated by combustion gas and slowly pulled at both ends to lessen the fiber's waist diameter. On this tapered region is a thin layer of metal that is exposed to the sensing which is shown in figure 3.7.a. [81] .A lot of researchers are working on the fiber-based SPR sensor to boost up the

performance of the sensing but still, there are some limitations in the field of research technology, and based on the published works, new methods are demonstrated to provide effective solutions for the fiber-based sensors. Our thesis work represents the current work of SPR sensor in order to enrich the sensing performance with a very low loss and also applicable for different biomolecule analyte detection sites furthermore. We explored PCF-based SPR sensors in our research to eradicate the loss problem and other fabrication problems.

4.7 Properties of SPR

4.7.1 Sellmeier Equation:

In order to fill the cladding layer with liquid, we used fused silica. Fused Silica (SiO_2) is used for the optical fiber-based excitation of SPR in the background material and in the main core material, as is our thesis. It is easy to vaporize polar substances, which are difficult to absorb non-polar organic substances. The vapor-phase axial deposition (VAD) arrangement was adopted for the making of silica nanoparticles which is applicable and necessary for the fabrication of fiber-based sensors. SiO2 Nano-fluids were generated at room temperature by adding nanoparticles in distilled water varying a two-step method. Colloids experienced agitation in a magnetic stirrer accompanied by ultrasonic mixing for around 1 hour in order to facilitate stabilization and coalescence of nanoparticles, thereby preventing the accumulation of materials [82, 83].

The refractive index of Silica ($n\ (\lambda)$) has been calculated using the Sellmeier equation given in equation (4.4).

$$n^2\ (\lambda) = \ 1 + \frac{B_1\,\lambda^2}{\lambda^2 - C_1} + \frac{B_2\,\lambda^2}{\lambda^2 - C_2} + \frac{B_3\lambda^2}{\lambda^2 - C_3} \tag{4.4}$$

Here *n* is silica's RI; λ indicates the wavelength in μm. The Sellmeier coefficients were taken from B1 = 0.696163, B2 = 0.407942600, B3 = 0.897479400, C1 = 4.67914826 × $10^{-3}\ \mu m^2$, C2 = 1.35120631×$10^{-2}\ \mu m^2$ and C3 = 97.9340025 μm^2 respectively [84]
For PCf based SPR sensor in our thesis, a metallic layer is mandatory.

4.7.2 Drude Lorentz Model

For the complex index of refraction and dielectric constant of materials, two researchers named Drude and Lorentz demonstrated a theory model (ca.1900). The idea is built on the application of electrons like particles that are harmonically bound to external electrical fields. To obtain the dielectric constant of gold, it is defined by the Drude-Lorentz model which is expressed in equation (4.5).

$$n_g^2 = \varepsilon_\infty - \frac{w_D^2}{w(w+j\gamma_D)} + \frac{\Delta\varepsilon^2\rho}{(w^2-\rho^2)+j\tau w} \quad (4.5)$$

here n_g= gold's refractive index, ε_∞= 5.9673 is gold's permittivity, $\Delta\varepsilon$ = 1.09 is the weighting vector, w is the angular frequency of the guided light, w_D and γ_D are the plasma frequency and damping frequency respectively, where w_D /2π = 2113.6 THz, and γ_D/2π = 15.92 THz. Moreover, ρ and τ indicate the frequency and spectral width of the Lorentz oscillator where ρ/2π = 650.07 THz and τ /2π = 104.86 THz [85].

4.7.3 Confinement Loss (CL) Property

Confinement loss is a very essential property for optical fiber technology. The losses in confinement result from leaking and the non-perfect PCF fiber structure. Then the modes are driven by structure-dependent loss according to the wavelength, the number of holes, and hole size. The confinement loss can be calculated by the consecutive equation (4.6).

$$\alpha_{loss} = 8.686 \times 2\pi/\lambda \times I_m(n_{eff}) \times 10^4 \text{ , dB/cm} \quad (4.6)$$

From the above equation, 2π/λ is wave number in the free space and the operating wavelength, λ is in μm. From the simulation, we can deduce the value of Im(neff) which signifies the imaginary part of the effective index [85]. The SPP mode is highly dependent on the small variation of analyte RI in the real part of n_{eff}. By creating a variation of analyte RI, there will be a significant change in n_{eff} which is accountable for phase-matching case in the resonance wavelength. If we increase the RI of an analyte, it will shift to the higher wavelength of the right side of n_{eff}. When the phase-matching condition is accomplished, a sharp resonance peak will appear in the resonance wavelength. From core mode to SPP mode, a large number of powers will be transferred. With little change in the RI index, the loss often varies. As the analysis RI increases marginally, the loss peak changes to greater wavelength [86].

.

4.7.4 Wavelength Sensitivity (WS)

Investigations on the sensitivity performance of SPR biosensor has been carried out using wavelength and amplitude interrogation method. WS is computed by the wavelength interrogation method through the formula given here in equation (4.7).

$$S_w(\lambda) = \frac{\Delta\lambda_{peak}}{\Delta n_a} \quad (4.7)$$

where, $\Delta\lambda_{peak}$ signifies the difference between the resonant wavelengths and Δn_a signifies the difference between analyte RI [85]. In the wavelength range, 600 - 1600 nm and up to ten graphene layers, sensitivity advances over conventional angular interrogated SPR sensors have been measured. The AS increases with an increment of analyte RI and resonance peak shifts towards higher wavelengths.

4.7.5 Amplitude sensitivity (AS)

Our main basis of the analysis and comparison between the two modes (X and Y Polarization mode) was dealt with Amplitude Sensitivity. The amplitude sensitivity of the sensor can be calculated by the amplitude interrogation method through the expression [85] given in equation (4.8).

,

$$S_A(\lambda) = -\frac{1}{\alpha(\lambda,n_a)}\frac{\Delta\alpha(\lambda,n_a)}{\Delta n_a} \tag{4.8}$$

here $\alpha(\lambda, n_a)$ means the overall loss where analyte refractive index is equivalent to n_a and $\Delta\alpha(\lambda, n_a)$ denotes the difference between two adjacent loss spectra due to a small change in RI of the analyte, Δn_a bespeaks the change of refractive index of the analyte. With an increment in film thickness, the sensitivity of amplitude increases since light is confined; which creates less penetration into the cover region of the core electric mode [87] .

.

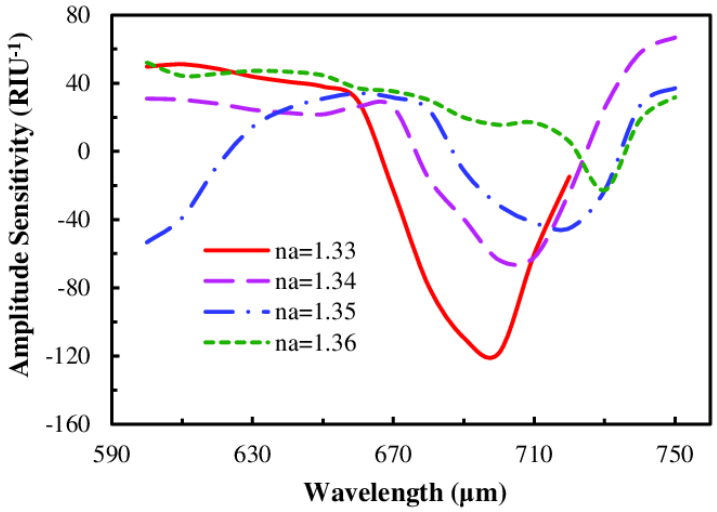

Figure 4-8: AS as a function of wavelength with the variation of analyte RI.

4.7.6 Sensor Resolution

Sensor resolution is an effective parameter which helps to achieve sensor detection ability. The resolution states that the sensor can detect a tiny change of RI of the order of 10^{-6} . The resolution provides an indication of the extent to which the RI is less modifiable. The suitability and significance of a sensor depend not only on increased sensitivity but also on the exact identification of the minimum spectral shift changes that are correctly accomplished by the analysts. By analyzing the sensor resolution, minor spectral shift shifts can be effectively detected with precision. In the resolution wavelength interrogation method, the resolution is determined by the equation (4.9).

$$R(w) = \frac{\Delta n_a \times \Delta \lambda_{min}}{\Delta \lambda peak(\ RIU)} \quad (4.9)$$

Assuming that, $\Delta\lambda_{min}$ = 0.1 nm which denotes the minimum spectral resolution, maximum peak shift stated as $\Delta\lambda peak$ and the analyte RI change is Δn_a = 0.01, we can calculate the maximum sensor resolution [85]. The resolution determined by the amplitude interrogation method is calculated by the equation (4.10).

$$R(A) = \frac{\Delta n_a}{S_A\ (\lambda)} \quad (4.10)$$

Here, Δn_a=0.01 and $S_A\ (\lambda)$ is the amplitude sensitivity. Amplitude sensitivity is displayed in Fig 4.8 as a function of analyte RI [85].

4.8 Factors that control the sensing performance of a SPR sensor

The consistency of sensor depends heavily on different geometry like the thickness of gold (Au) layer, thickness of TiO_2 layer, thickness of analyte layer, diameter of the air hole, etc. These parameters must be adjusted to achieve the sensor's highest sensitivity. Other parameters must be kept constant when optimizing one parameter. So we need the proper investigation; therefore, the best results can be attained by optimizing the various parameters, so that the value of the highest sensitivity with relatively low losses can be obtained. The definition and effects of these important parameters on the performance of sensing are given in this section.

4.8.1 Significance of plasmonic material thickness on sensing performance

A thin film-coated plasmonic material is used outside the cladding layer to strengthen the sensing efficiency of sensor, which also is vital to resonance wavelength shifting. Different plasmonic materials like silver, copper, gold, TIN, AZO, etc. are used in SPR sensor. The lower entry of evanescent field into the surface is also influenced by higher thickness, causing lower amplitude sensitivity. Moreover, increase in thickness leads to a decreased depth of loss raising the peak loss to a longer wavelength. Thus, the thickness and sensitivity are reversed. The excited polaritons have to drive more space to enter the analyte and to contact with it when the thickness is increased. Rising in thickness gradually reduces the penetration of light which translates the loss peak towards a higher resonant wavelength [88].

.

4.8.2 Significance of cladding and core air hole diameter on sensing performance

From the research work, it was investigated that if we vary the airholes in diameter, it will alter the amplitude sensitivity of the sensor. With the increment in diameter, the core guided useful index will spread out over the cladding region. This will result in the reduction of surface excitation. Thus choosing a proper optimum radius for the air holes of this position is a very crucial investigation to perform.

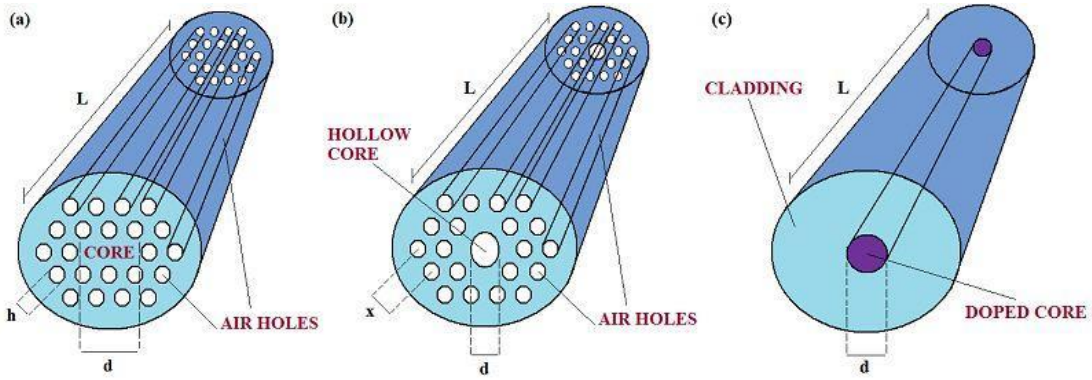

Figure 4-9: Airholes of different diameters in optical fiber sensor.

The n_{eff} gap between the core and cladding is smaller due to the greater core air hole diameter. This will raise losses in the SPR sensor [89].

4.8.3 Importance of pitch distance on sensing performance

The sensor demonstrates no noticeable change to the wavelength sensitivity when the pitch distances differ, but significant changes in the sensitivity to the amplitude are detected. In some cases, however, resonant peaks are transformed into higher pitch lengths and lower pitch lengths with a higher pitch. In addition, the loss peak varies with an increase in pitch (∧) toward a lower wavelength with an increased confinement loss value because the light is less tightly confined to the field of the core [88].

4.8.4 Effect of PML thickness on sensing performance

PML stands for "Perfectly Matched Layer" which has very slight impact on the confinement loss and also on the sensitivity. The absence of a PML layer does not contribute to an erroneous result nor does it affect the sensitivity of the sensor to a large degree. But it is competent for incorporating the dissipated PCF waves and thus acts as a computational boundary. This boundary is necessary for our software medium to

successfully simulate. By comparing amplitude sensitivity variations for different thicknesses, the thickness of this layer was optimized.

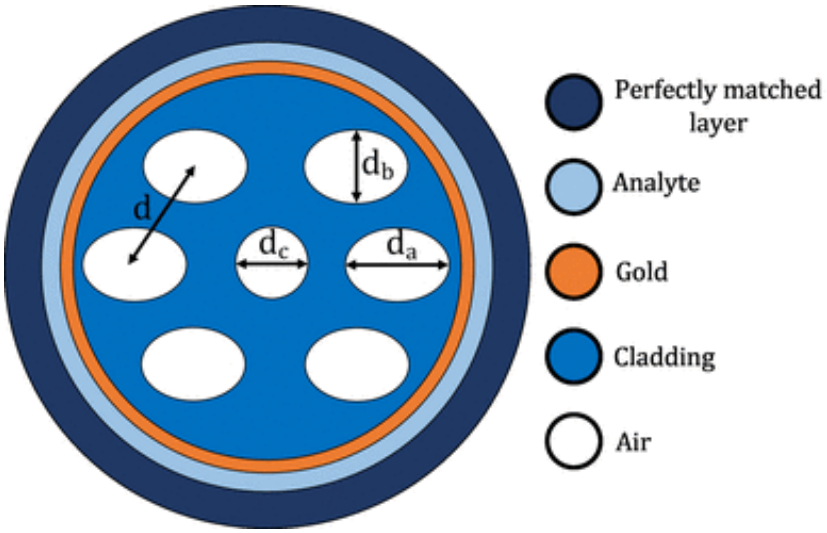

Figure 4-10: PML layer in SPR sensor

PML is still a wave absorbing substance in which even isolated waves disperse throughout it. There is no longer a reflectionless boundary between the PML and the normal medium but the responses are small as the boundary condition is (provided) a good approximation for the exact wave equation [90].

In our thesis work, we deeply analyze the effect of the PML layer in the SPR sensor. From our thesis work, it was concluded that reduction of PML thickness below 1.0 μm resulted in a great change in amplitude sensitivity but PML thickness larger than 1.0 μm produced similar type sensing performance.

4.8.5 Effect of Analyte RI on sensing performance

The sensors are placed on the RI, due to the need for a number of applications to establish easy, low-cost and high performance detection technologies. The sensing medium of most of the RI is quite similar but their design may vary from researcher to researcher. The RI inflation reduces the RI difference between the core-guided mode and SPP mode and allows the sensor more sensitive. Increasing RI reduces the sensor length because the sensor length depends entirely on the loss of absorption. Thus, the sensitivity peak changes into higher resonance wavelengths and extends the entire curve by rising RI conversely. In our thesis work, we achieve our various analyses based on the RI computation while obtaining various parameter values.

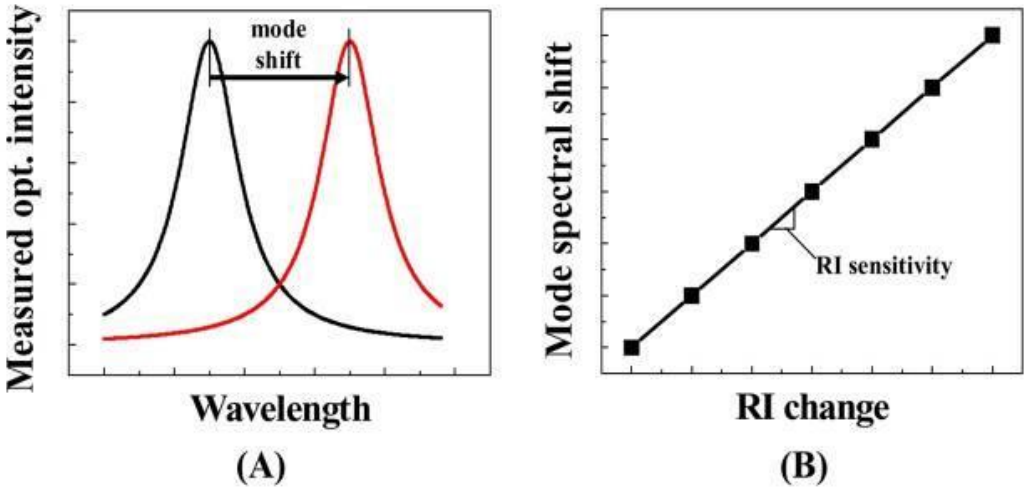

Figure 4-11: (A). The optical RI sensors typically have an optical resonance and a resonant wavelength depending on the RI of the sample. When the changes occur in a sample of RI, the mode transforms accordingly. (B). The RI sensitivity is accomplished by measuring the spectral shift of the resonant mode for known changes in sample RI.

Chapter 5

Simulation and Experimental Analysis of a low-loss Surface Plasmon Resonance-based PCF biosensor with a gold-coated structure

5.1 Geometrical Structure and Design Consideration

Commercially available COMSOL Multiphysics 5.3a has been introduced with Finite Element Method (FEM) and stack and draw method for the designing and fabrication of the proposed sensor. MATLAB was also used for the graphical analysis of various parameters. The structure consists of layers of plasmonic material (gold) of thickness t_g, analyte material of thickness t_a, a perfectly matched layer (PML) of thickness t_p, and air holes of three sizes (A_1, A_2, A_3). A perfectly matched layer does not have much effect on the performance of the sensor. It is still required for the successful simulation of the design. These parameters were optimized depending upon the maximum AS (Amplitude Sensitivity) obtained after varying each of the parameters for a certain range. The initial values were t_g = 20 nm, t_a = 1.5 µm, t_p = 1.5 µm, A_1 = 0.9 µm, A_2 = 0.25 µm and A_3 = 0.5 µm. The thickness of gold was varied from 0.20 nm - 0.40 nm, analyte thickness was varied from 0.75 µm - 2 µm, and PML thickness was varied from 1 µm - 2 µm. The optimized values of these parameters are given below. The structure showing all the layers and air holes is demonstrated in Fig. 5.1.

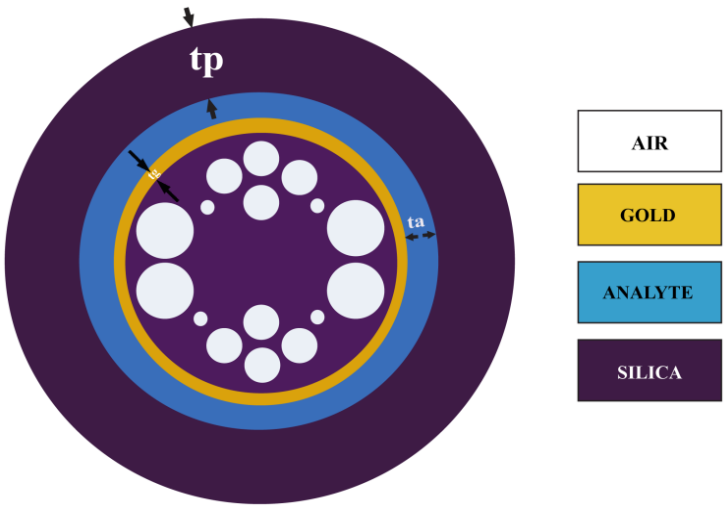

Figure 5-1 : Sensor with all the layers (2D Cross-sectional view).

Table 5-1: Parameter Optimization

Gold Thickness t_g	Analyte Thicknes t_a	PML Thickness t_p	Airhole_1 Radius A_1	Airhole_2 Radius A_2	Airhole_3 Radius, A_3
25 nm	0.9 µm	1.5 µm	0.85 µm	0.2 µm	0.5 µm

In order to get better accuracy in the sensing result, Mesh of "extremely fine" type has been applied which resulted in 64334 elements where we found 80 vertex elements and 2876 boundary elements. For the simulation, the Refractive index (RI) was chosen as the electric displacement field model. The refractive indices of silica and gold were found through various equations. Equation (4.5) is the equation for gold's RI (η_g) which was derived from the Drude-Lorenz model [85]. Silica's refractive index ($n\ (\lambda)$) property is defined by Sellmeier equation (4.4) [85].

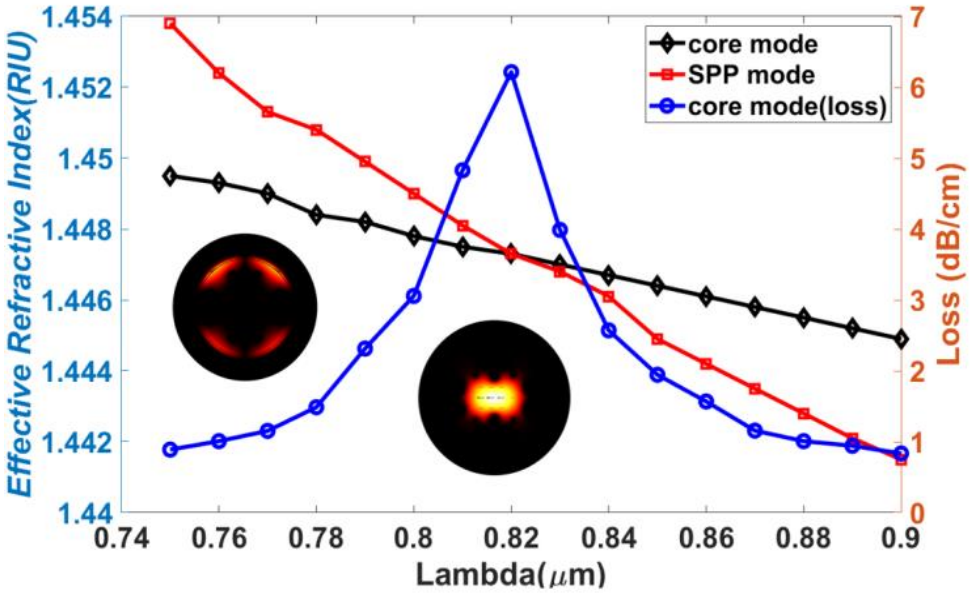

Figure 5-2: Matched phase of core-guided and SPP mode.

The authenticity of this structure was assessed by matching the phase of the core-guided mode and SPP (Surface Plasmon Polariton) mode of the sensor. The corroded electromagnetic field excites metal surface-free electrons during the light dissemination. SPR usually appears and transfers maximum energy if the frequency of free electrons and the leaky electromagnetic field matches. (Li X, Li S, Yan X, Sun D, Liu Z, Cheng T). High sensitivity photonic crystal fiber refractive index sensor with gold coated externally based on surface plasmon resonance. Micro machines 2018; 9:640]. 820 nm was found to be the resonant wavelength where the intersection occurred between the effective refractive indices (η_{eff}) of core-guided mode and SPP mode at η_{eff}= 1.447. This is shown in Fig. 5.2.

5.2 Result and Performance Investigation

In the following figures (Fig. 5.3 and Fig. 5.4) for both polarization modes, we demonstrated loss spectrum and amplitude sensitivity (AS) by varying the RI. It is evident that x-polarization produces the better result if we compare the amplitude sensitivity and thus this is our chosen mode for further analysis.

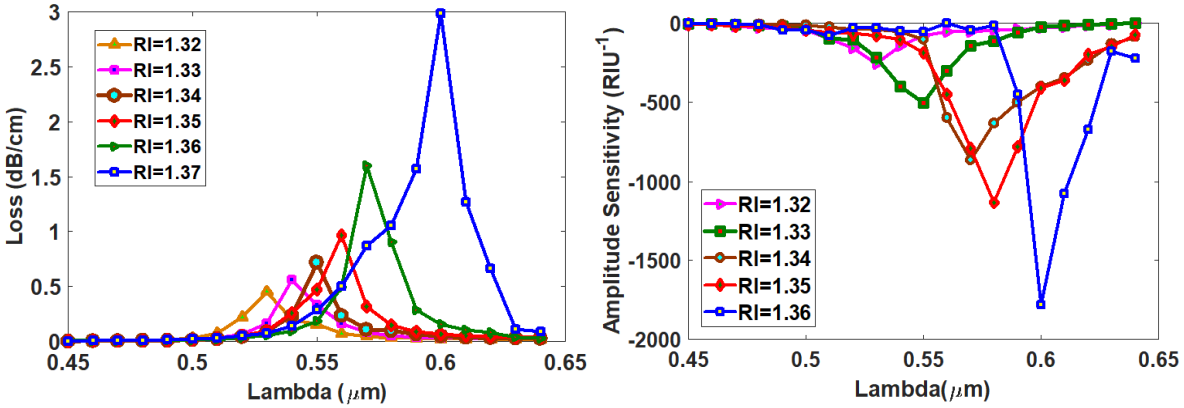

(a) (b)

Figure 5-3: (a) Loss vs. Wavelength and (b) Amplitude Sensitivity vs. Wavelength at X-polarization for different RI.

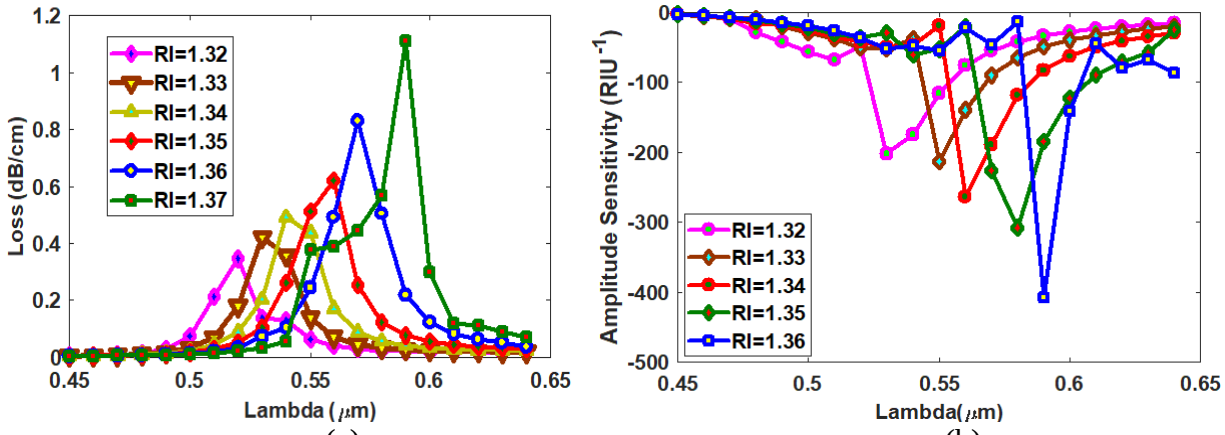

(a) (b)

Figure 5-4: (a) Loss vs. Wavelength for different RI and (b) Amplitude Sensitivity vs. Wavelength at Y-polarization for different RI.

The confinement loss and sensitivity using wavelength and amplitude interrogation were computed using equation (4.6), equation (4.7), and equation (4.8) respectively [85]. The chosen sensing range was between RI = 1.32 and RI = 1.37 and the analysis was done in between wavelengths of 450 - 640 nm. The highest loss (2.98 dB/cm) was found at RI = 1.37, the highest WS of 3000 nm/RIU, and the highest AS of 1779 RIU^{-1} was found at the previous RI which is at RI = 1.36. The sensor resolution by amplitude wavelength and interrogation were computed using the equation (4.10) and equation (4.9) respectively [85]. If we assume $\Delta\lambda_{min}$ = 0.1 nm, maximum peak shift to be Δλpeak and the analyte RI varies Δn_a = 0.01, we can calculate the maximum sensor resolution. Our minimum obtained sensor resolution for wavelength interrogation was 3.33×10^{-5} and that for amplitude interrogation was 5.62×10^{-6}. From the loss curve, the values of Full Width at Half Maximums (FWHMs) were taken and values of Figure of Merits (FOMs) were computed using equation (5.1) [85].

$$FOM = \frac{S_w(\lambda)}{\text{FWHM}} \tag{5.1}$$

Birefringence was also computed for all the RI in our sensing range and a highest value of 0.0049 was achieved by using equation (2.3) [85]. In order to keep the polarization state of the input signal significantly, the birefringence of the sensor has to be very high as possible [91]. The various performance parameters obtained from the analysis of the sensors are shown in table 5.2

Table 5-2: Performance of the proposed sensor

Analyte RI	Peak Loss (dB/cm)	Resonant Peak Wavelength (nm)	Resonant Peak Shift (nm)	Amplitude Sensitivity (RIU^{-1})) In X-polarization	Wavelength Sensitivity (nm/RIU) In X-polarization	FWHM (X-pol)	FOM(X-pol)	Birefringence
1.32	0.453	530	10	256	1000	20	50	0.0001
1.33	0.560	540	10	502.908	1000	15	66.67	0.0001
1.34	0.719	550	10	866.45	1000	13	76.92	0.0049
1.35	0.968	560	10	1137	1000	13	76.92	0.0028
1.36	1.60	570	30	1779	3000	16	187.5	0.0001
1.37	2.98	600	N/A	N/A	N/A	24	N/A	0.0049

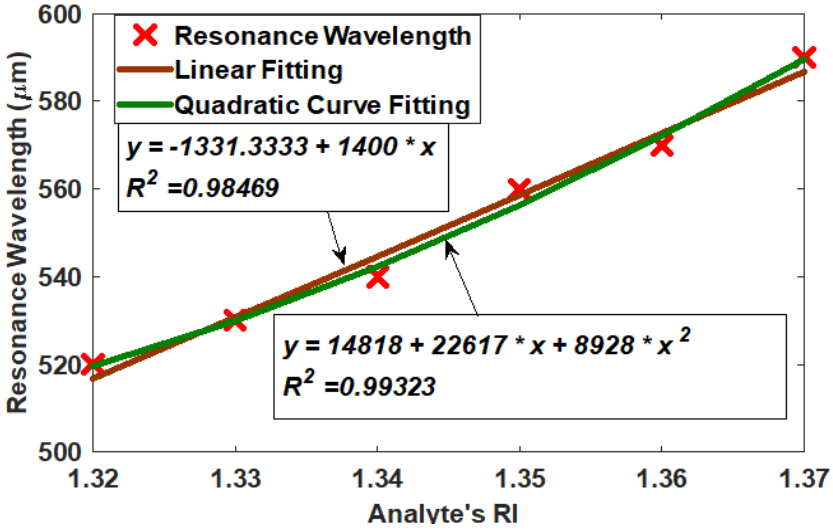

Figure 5-5: Curve fitting of resonant wavelength as a function of analyte RI for X-polarization.

Figure 5.5 shows the linear relationship of our obtained loss curve where R^2 for linear fit= 0.98469 and that for quadratic fit= 0.99323. This shows the relation between the resonant wavelengths at each RI with the respective RI.

Table 5.3 below compares some of the earlier works done on PCF-SPR sensors with this proposed sensor.

Table 5-3: Comparing suggested sensor with prior sensors

Ref No.	Sensing Range	Wavelength Sensitivity (nm/RIU)	Amplitude Sensitivity (RIU^{-1})	Sensor-Resolution (RIU)	Polarization Mode
[23]	1.33-1.37	1000	118	1×10^{-4}	N/A
[92]	1.33-1.37	2000	140	5×10^{-5}	N/A
[49]	1.33-1.37	2200	266	3.75×10^{-5}	N/A
[93]	1.33-1.35	2520	72.47	3.97×10^{-5}	N/A
Proposed work	1.32-1.36	3000	1779	3.33×10^{-5}	X pol

5.3 Conclusion

In essence, a gold-coated surface plasmon resonance-based PCF sensor has been investigated in our proposed structure, which can perform well for different sensing mechanisms. Our proposed design analysis showed an amplitude sensitivity of 1779 RIU^{-1}, 407 RIU^{-1}, and wavelength sensitivity of 3000 nm/RIU, 2000 nm/RIU in x, and y polarization modes, respectively, which is showing very low loss and higher sensing performances. It also exhibited a minimum amplitude sensor resolution of 5.62×10^{-6} RIU and a minimum wavelength sensor resolution of 3.33×10^{-5} RIU. Additionally, birefringence of 0.0049 and FOM value of 187.5 have been observed. The evaluated sensor will be useful due to its good sensing characteristics and will have candidates for problem-solving time diagnostic usages such as food control and biological analyte detection. Various biosensing studies can also be executed with this sensor furthermore.

Chapter 6

Simulation and Experimental Analysis of a Surface Plasmon Resonance Based Highly Sensitive Gold Coated PCF Biosensor

6.1 Introduction:

In this work, we are proposing a highly sensitive gold-coated simple dual-polarized, PCF-based SPR sensor having circular-shaped air holes for gaining better sensing performance and low loss. The sensor which is proposed can provide low losses and high sensitivity which is numerically tested by the Finite Element Method (FEM) through the software COMSOL 5.3a that is available to us commercially. Our goal is to successfully design a sensor that is structurally simple, easy to fabricate giving high sensing performance. Our desired characteristics also count for low loss, high sensor resolution with improved WS and AS. The simplicity of design allows for a practically realizable PCF manufacturing that provides the possibility of commercial use of the sensor.

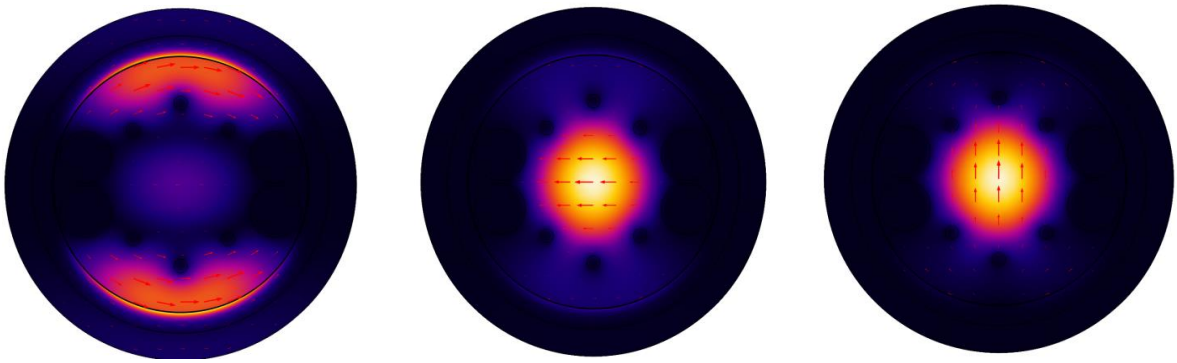

(a) (b) (c)

Figure 6-1: (a) SPP-mode, (b) core-guided mode X-polarization, (c) core-guided mode Y-polarization.

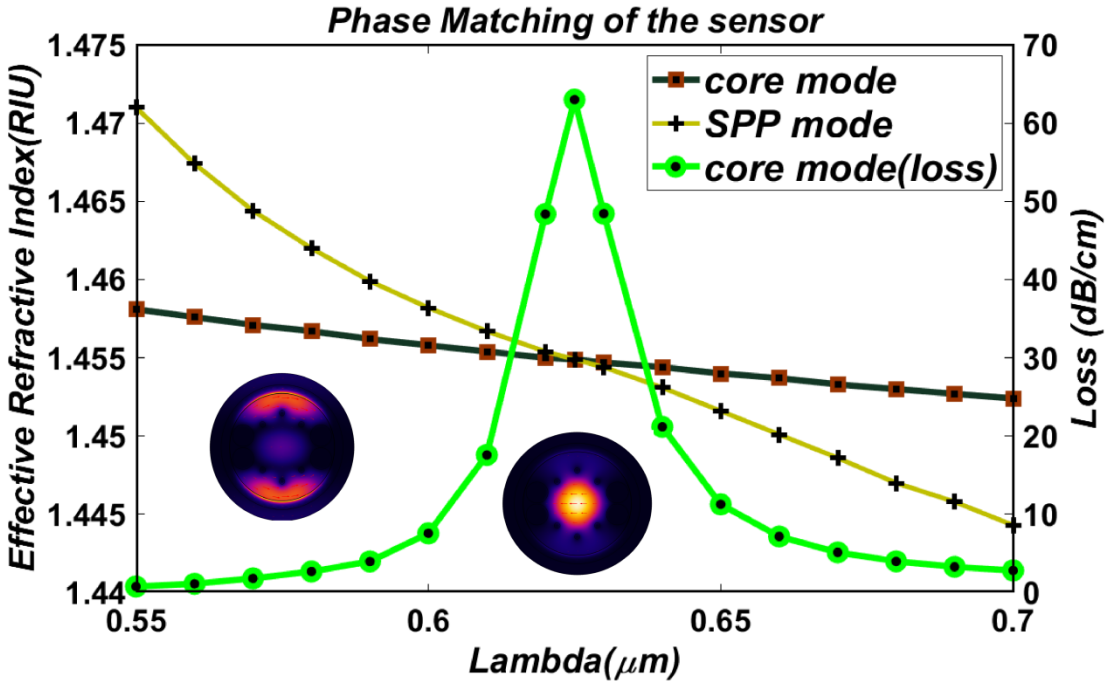

Figure 6-2: Phase matching of core guided mode and SPP mode.

According to the mathematical explanation, resonance occurs when the real effective refractive index (neff) of core-guided mode and surface plasmon polaritons (SPP) mode value are exactly equal. The core mode's effective value of the refractive index (RI) intersected with that of SPP mode at RI = 1.4549 and at the corresponding lambda = 625nm the peak loss occurred. So resonance will occur at lambda = 625nm. Unknown analytes will be detected at this phase of matching wavelength by shifting the resonance peak.

6.2 Design Methodology:

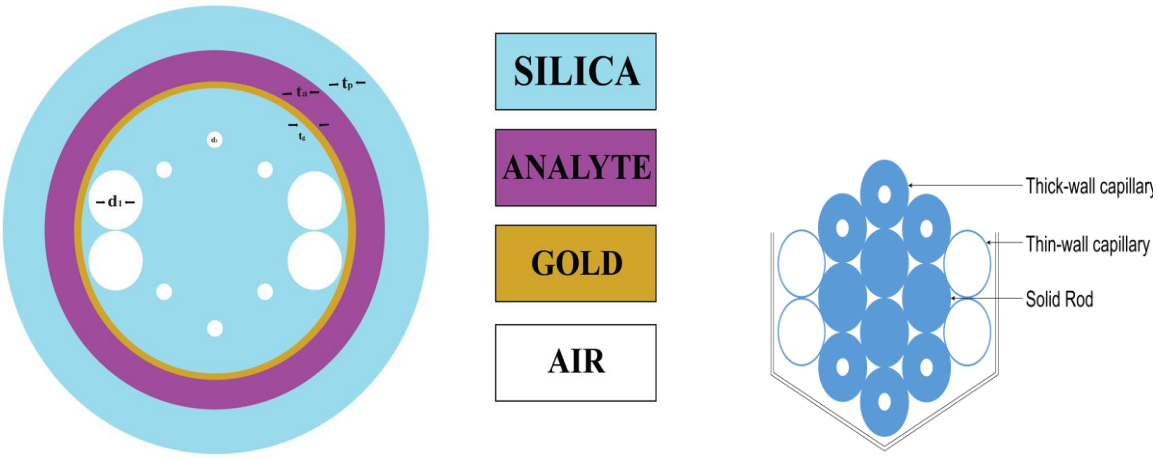

(a) (b)

Figure 6-3: (a) 2-D cross-sectional view and (b) Stack perform of the proposed sensor.

The design is computed and investigated using the commercially available COMSOL 5.3a software. The method which has been used for designing the sensor is the stack and draw method. The finite Element Method (FEM) was applied to assess the sensor. Figure 6.3 denotes the different parts of the sensor. The structure has been computationally analyzed with 153001 degrees of freedom and a mesh of "Extra Fine" was appointed for the simulation of the structure. The complete mesh consists of 34552 domain elements and 2358 boundary elements. The meshing of the structure gives us finite solutions instead of infinite solutions and is crucial for solving through FEM. The values of various parameters in the design are decided upon by their sensing performance. The material used in the perfectly matched layer (PML) and in the surface on which air holes reside is Silica. The refractive index of Silica has been calculated using the Sellmeier equation (4.4) [84, 85]. Figure 6.3(a) shows various layers of the sensor and their materials. Figure 6.3(b) shows the realization of the air holes through the stacking of capillary rods. The scaled-down air holes are represented by capillaries with thick walls and the greater air holes are depicted by capillaries with thin walls. Solid rods have been inserted where there is no air hole [94]. This stacking ascertains the practicality of realizing the fabrication of the designed sensor.

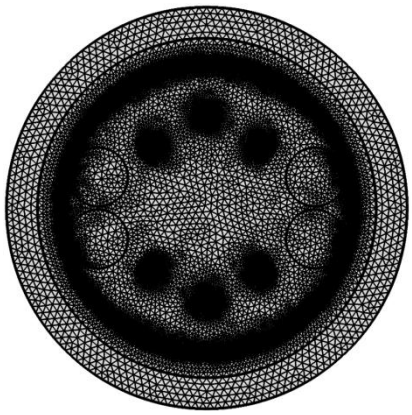

Figure 6-4: Mesh structure of the proposed sensor**.**

6.3 Investigation of sensing performance of parameters:

The sensor performance can be considered as a function of the geometrical parameters of the PCF. Moreover, these parameters affect the interaction of the gold surface and the evanescent field. Thus, these parameters must be selected carefully. These parameters include gold film thickness, analyte layer thickness, PML layer thickness, bigger air hole diameter, and smaller air hole diameter and refractive index values. Initially we used Gold film thickness = 30nm, Analyte layer thickness = 0.96 µm, PML layer thickness = 1.5 µm, Bigger air hole diameter = 0.95µm, Smaller air hole diameter = 0.25 µm, RI = 1.4 before optimization. While optimizing these parameters, we measured the confinement loss (CL), amplitude sensitivity (AS), and wavelength sensitivity (WS) for different values of any particular parameter.

6.3.1 Optimization of gold thickness:

Before optimizing the other parameters, we will talk about the inner circle of the gold layer in the structure. Its radius is kept at 4.7 µm. If it is increased, amplitude sensitivity would be decreased dramatically. Now let us examine the gold layer's thickness at first. Gold is used as a chemically stable and active plasmonic material in the aqueous region in this sensor design. It enhances the detection level of an analyte in the sensor. Proper thickness of gold layer contributes to enhanced sensor performance and affects the shift in resonant wavelength. Gold provides a significant resonance peak shift, which can be seen from Figure 5(a). Apart from this, the Gold layer also provides fabrication feasibility. Upon investigating, it was found that an increase in thickness caused the resonance peak to shift towards the larger wavelength. The gold layer's RI was measured by using the Drude-Lorenz model which is given by equation (4.5) [35, 85]**.** Nanoscale properties of gold are crucial for the surface plasmon waves (SPW) to appear. But this fact applies for thickness between 20nm to 50nm [95, 96]. The value of gold thickness was the first parameter to be optimized. To do so, all the other settings were kept constant, and gold thickness varied from 20nm to 35nm, and the range of wavelength was [550nm-800nm]. After comparing the results, we obtained amplitude sensitivity at various gold thickness values by amplitude interrogation method. From figure 6.5(a) and 6.5(b), it is evident that loss at gold thickness = 25nm is maximum, and a maximum sensitivity (1164RIU^{-1}) was found at gold thickness = 25nm. It can also be followed that the amplitude sensitivity at thickness = 20nm is higher than the sensitivity obtained at thickness = 30nm. Thus we take gold thickness = 25nm as the optimized value for this design.

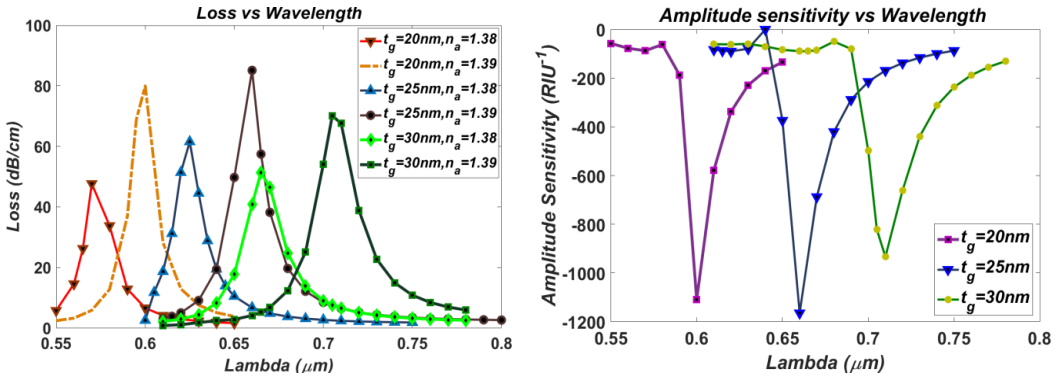

(a) (b)

Figure 6-5: (a) Loss vs. Wavelength and (b) Amplitude Sensitivity vs. Wavelength for various thicknesses of gold.

The confinement loss was calculated from the expression (4.6) [97]. We are optimizing all the parameters considering the amplitude sensitivity since it is a simple and economic process [75, 97, and 98] and wavelength interpolation is not required in this case. In wavelength interrogation methods, the maximum resonance wavelength shift can give the sensitivity of a sensor. Wavelength sensitivity was formulated by the wavelength interrogation method through the formula (4.7) [85, 97, and 99]**.** The AS can be computed from the following equation (4.8) [85,100].

Amplitude sensitivity rises with an increment of analyte RI and peak point shifts towards a higher wavelength.

6.3.2 Optimization of analyte thickness:

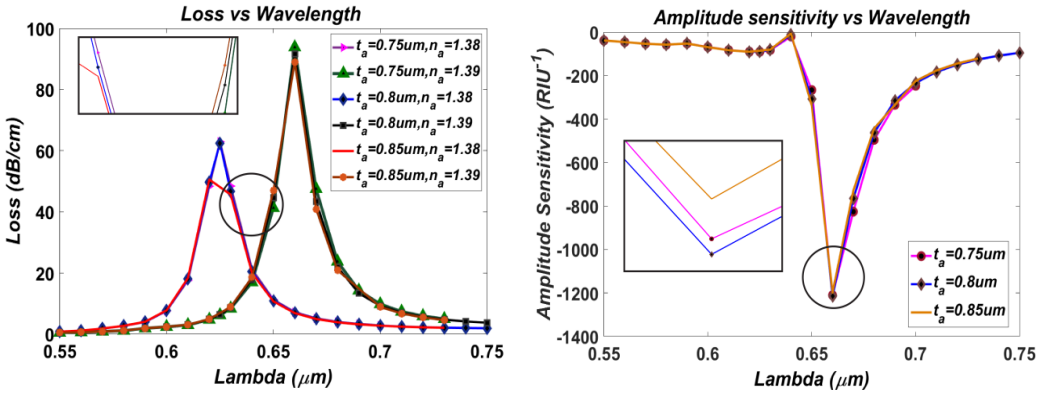

(a) (b)

Figure 6-6: (a) Loss vs. Wavelength and (b) Amplitude Sensitivity vs. Wavelength for different Analyte thicknesses.

The difference in the analyte refractive indices allows mode confinement and overall reflection. This sensor is dependent on the unknown output of the analyte detection. The thickness of the analyte is thus a vital element of the design. The thickness value of the analyte was optimized after optimization of the value in gold by maintaining a constant gold stiffens parameter and varying the thickness of the analyte. Few factors were considered during optimizing the thickness. A thinner analyte layer produces better results regarding sensitivity. But detection of an analyte using a layer too thin or too thick would result in errors. The resulting loss and sensitivity at different analyte thicknesses are shown in Figure 6.6. As the values were varied, it was found that at a thickness of less than 0.8µm, the amplitude sensitivity decreased. A similar case was observed for the thickness values of more than 0.8µm, which is evident from figure 6.6(b). At thicknesses lesser than 0.5 µm, we found AS of more than that for thickness 0.7 µm. Due to the lack of practicality of the thickness, those thicknesses were not chosen. Thus the values varied from 0.7 µm to 1 µm, and the wavelength varied from 550nm to 750nm. At the thickness of 0.8 µm, the highest sensitivity of 1214 RIU^{-1} was found. Hence this value was made the optimum value for analyte thickness.

6.3.3 *Optimization of PML (Perfectly Matched Layer) thickness:*

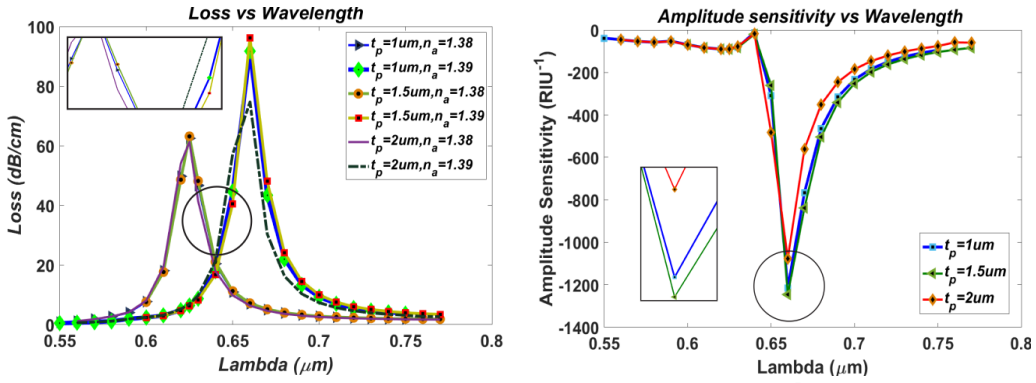

(a) (b)

Figure 6-7: (a) Loss vs. Wavelength for different PML thicknesses and (b) Amplitude Sensitivity vs. Wavelength for different PML thicknesses.

A Perfectly Matched Layer (PML) is an integral part of the simulation even though its absence in practice does not result in an erroneous result. Its capacity is to assimilate the dissipated waves from PCF and in this manner; it behaves as a computational boundary [85,101]. The difference in qualities due to variation of the thickness of the PML is seen in Figure 6.7. The confinement loss, as appeared in figure 6.7(a), shows that PML has an insignificant effect on the confinement loss of the sensor in contrast with the loss acquired for the analyte case (Figure 6.6(a)). When the PML thickness is made under 1.5µm, the Amplitude sensitivity decreases, and a similar case happens for a thickness of more than 1.5 µm. Taking the detecting performance and size of the sensor into thought, we pick 1.5 µm (ranging from 0.9 µm to 2 µm) as the ideal PML thickness, where maximum sensitivity (1245 RIU^{-1}) has been found.

6.3.4 *Optimization of bigger air hole diameter*

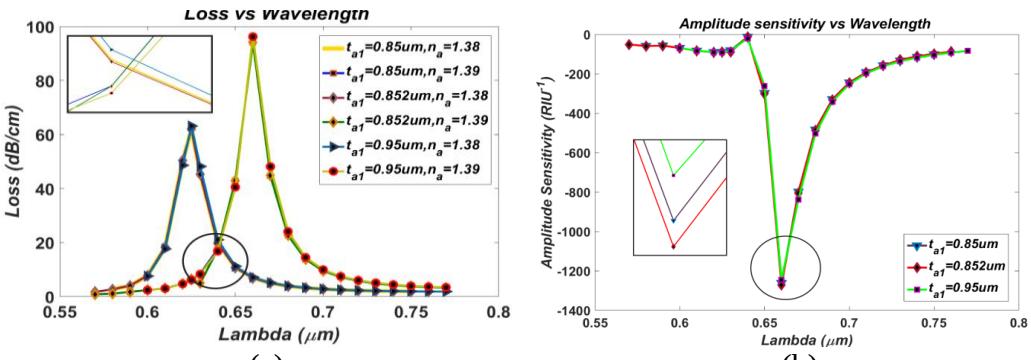

(a) (b)

Figure 6-8: (a) Loss vs. Wavelength for different radii and (b) Amplitude Sensitivity vs. Wavelength for different radii.

In this design, inside the first inner circle, there are air holes of two sizes. Subsequent to advancing the thickness of the gold, analyte, and PML layers, we

optimized the radius of bigger air holes between two different air holes. Figure 8 depicts the variety of confinement loss of the sensor, for change in range of greater airhole. The Refractive index of the core guided mode is influenced by the changes in the air holes and thus influences the phase matching between SPP mode and the core guided mode. Changes in the resonance intensity, resonance peak, and resonance wavelength are seen because of this. Subsequently, we can change the size of this airhole to optimize sensor performance. We found maximum sensitivity of 1271 RIU^{-1} at radius = 0.852 µm while varying the radius from 0.75 µm to 1 µm in the wavelength interval of 550nm - 800nm. It can be seen that changing the radius of the bigger airhole did not result in a significant amount of change in confinement loss and sensitivity. The positioning of the air holes of this radius and contribution to producing SPW are the reasons behind this.

6.3.5 Optimization of smaller air hole diameter:

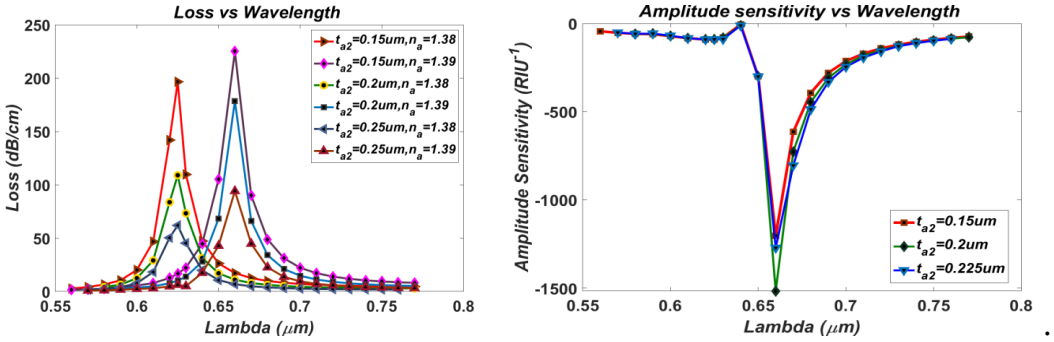

(a) (b)

Figure 6-9: (a) Loss vs. Wavelength for different radii and (b) Amplitude Sensitivity vs. Wavelength for different radii

Between the two different radii, now the smaller one is being optimized. In the cladding region, the air holes radius plays an essential part in sensing performance. These air holes play a bigger role in producing the surface plasmon polaritons and waves. Thus the effect of changing their radius by a small amount is significant on confinement loss and Amplitude sensitivity. From figure 6.9, we can see that the radius of this air hole mostly affects the confinement loss. The highest loss, in this case, is much higher than the highest loss obtained in the previous cases. With the increment in diameter, the core guided useful index will diminish, and guiding light will disseminate along the cladding region. This will result in the reduction of surface excitation. Thus choosing a proper optimum radius for the air holes of this position is a very crucial investigation to perform. After obtaining the optimized value of the bigger radius, the value of a smaller radius was varied from 0.15µm to 0.3µm in the wavelength interval of 550nm - 800nm. The maximum sensitivity of 1515 RIU^{-1} was found at 0.2µm among the other values, and it is evident in Figure 6.9(b). Excitation is a pivotal issue for SPR. In Figure 6.9(a), the confinement losses of core guided mode found at different radii of this air hole are expressed.

6.4 Sensing performance for different RI (Refractive Index) values:

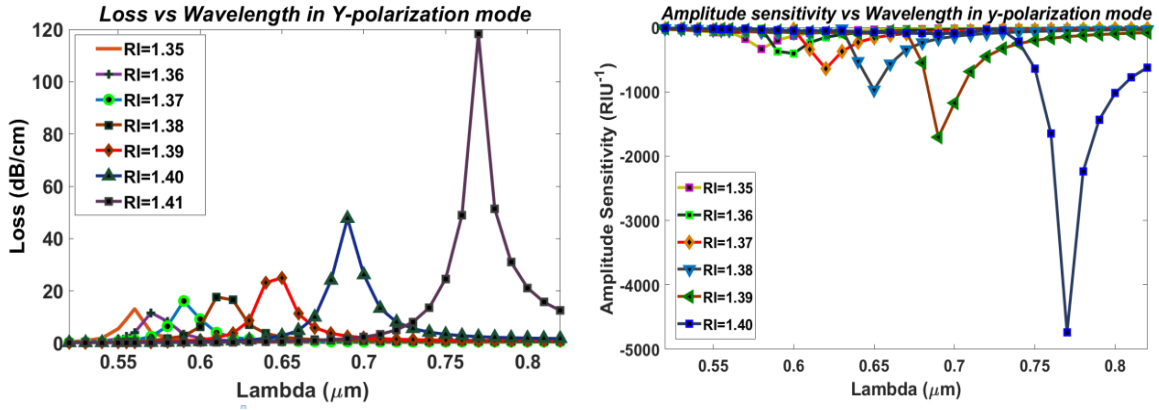

(a) (b)

Figure 6-10: (a) Loss vs. Wavelength for different RI and (b) Amplitude Sensitivity vs. Wavelength for different RI.

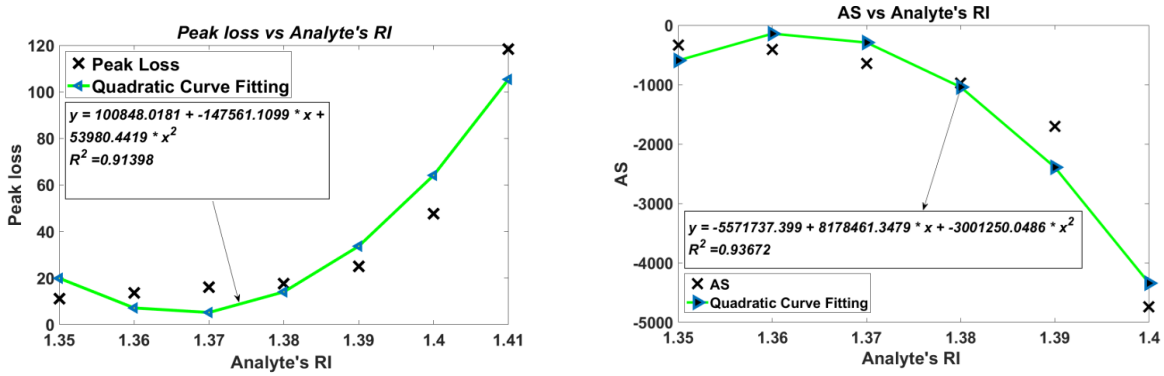

(a) (b)

Figure 6-11: Polynomial behavior of (c) peak loss and (d) amplitude sensitivity at different RI.

Between X-polarization and Y-polarization modes, Y-polarization generates larger evanescent fields exciting more surface-free electrons in the loss curve. It is better than X-polarization even though similar properties can be found in X-polarization. That is why for the final result, we are considering y-polarization as the fundamental mode. Within the wavelength range between 520 nm to 820 nm, the characteristics of confinement loss and amplitude sensitivity for the Y polarization of the analyte RI varying from 1.35 to 1.41 are demonstrated in Figures 6.10(a) and 6.10(b). Confinement loss characteristics of different analytes provide the performance measurement of the sensor. An increment of analyte RI is shown in Figure 6.10(a) which states that the resonance peak shifts towards the longer wavelengths eventually. It is observed from figure 6.10 that this instance results in high sensitivity for greater RI. Figure 6.11 describes the characteristics of the pattern or behavior of the confinement loss and amplitude sensitivity with the change of analyte RI. Both the parameters follow a quadratic behavior which results in a sharp increase in their values at the last RI of our range. We found a resonance wavelength shifting of 80 nm for the analyte RI of 1.40 and 1.41 in Y polarization mode after investigating figure 6.10(a) which is the maximum

in this case. At RI of 1.4 in the Y polarized mode, we achieved a wavelength sensitivity of 8000 nm/RIU which is the maximum one. For X polarized mode, a maximum shift of 145 nm was found and thus a maximum wavelength sensitivity of 14500nm/RIU was found in that mode.

For detecting the analytes, the amplitude (phase) detection method is more convenient than the wavelength interrogation method. The amplitude sensitivity which we calculated for y polarization mode has appeared in Fig. 6.10(b). As a sharper loss peak is obtained at analyte RI= 1.4, the maximal AS for the Y polarization is evidently 4738 RIU^{-1}. At wavelength 690 nm, the highest loss spectrum is 118 dB/cm and the maximal WS equals 14500 nm/RIU is achieved for analyte refractive index = 1.4 at X-polarized mode.

6.5 Fiber Linearity

To get an optimized sensor within a defined effectual range, linear fitting features are needed. For the measurement of sensors, high sensor linearity is a precondition, particularly for high RI analytes. Average sensitivity can be deduced from the gradient of the linear fitting curve. The nonlinearity of the reaction causes critical varieties in the average sensitivity and resolution making the detection procedure increasingly intricate. Thus it is not a desired quality in a sensor [98,102, 103] If the sensor shows linearity, it is easier to predict the resonant wavelength for the higher analyte RI [104]. The more the linearity, the more proportional is the shift of resonant wavelength. The correlation coefficient (R) can depict the linearity and it is acquired by performing linear regression. As a component of analyte RI, linear fitting of the resonant wavelength is portrayed in Figure 6.12. The regression equation for a linear fit of the proposed sensor is $y = -3949.2857 + 3321.4286x$ and the Regression Coefficient is R^2=0.90927. For the quadratic fit, the equation and value of R^2 were found to be $y = 107117.3838 - 157678.5755x + 58333.3348x^2$ and 0.99341. It is evident that the value of the correlation coefficient is very close to the value 1. This shows the continuous response over the sensing region of 1.35-1.41.

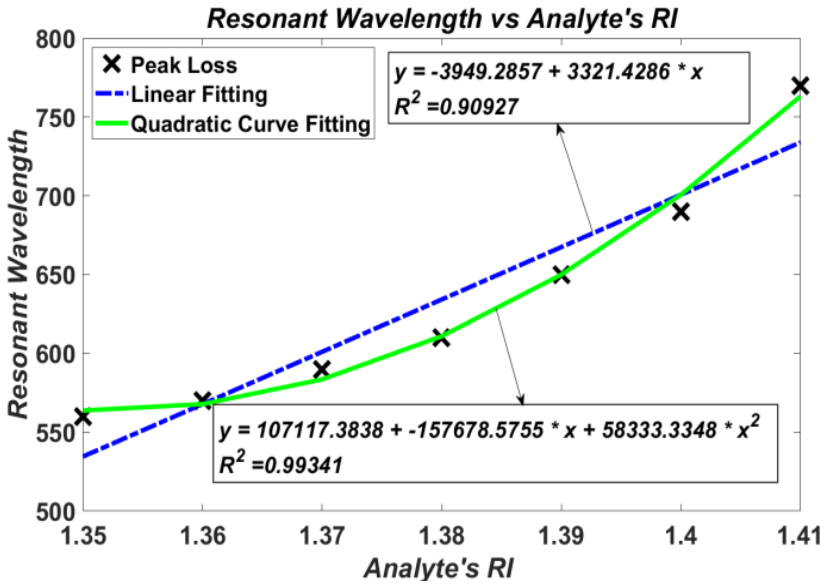

Figure 6-12: Resonant wavelength vs. analyte RI for Y-polarization.

From figure 6.12, it was found that a quadratic fit produced a closer regression coefficient to 1 than that of the linear fit. From this instance, the sensor performance can be predicted for the next RI range following the quadratic behavior.

6.6 Sensor resolution:

The suitability and importance of a sensor not only rely upon a higher sensitivity but also relies upon precise detection of the minimum spectral shift change, which detects analytes properly. By investigating the sensor resolution, small changes of the spectral shift with precision can be identified effectively. In the interval of 1.35-1.41, the analyte refractive indexes are shown. An average shift of 49.16 nm and 35 nm in the resonance wavelength is observed with the variation of 0.01 in the refractive index for X and Y polarized mode respectively. From this phenomenon, we obtained an average spectral sensitivity of 3500 nm/RIU accurately. In the resolution wavelength interrogation method, a resolution is calculated by the equation (4.9) and our result is compared with the reference [105]. While producing practical simulation, Optical Spectrum Analyzer (OSA) is used. To correctly assess the change in resonant wavelength shift for the smallest change, this instrument computes results with a wavelength resolution of 0.1 nm or 1 Å [106]. Assuming that, $\Delta\lambda_{min}$ = 0.1 nm which denotes the minimum spectral resolution, maximum peak shift denoted as $\Delta\lambda$peak and the analyte RI change is Δn_a = 0.01, we can calculate the maximum sensor resolution. The amplitude detection procedure is proved as a very cost-effective method to measure the sensitivity. The absence of the need of spectral manipulation reduces the number of iterations done for calculation [107]. The resolution determined by the amplitude interrogation method is calculated by the equation (4.10). Amplitude sensitivity has appeared in Fig. 6.10 (b) with varying analyte RI. From Fig. 6.10(b), among the refractive indexes of 1.35, 1.36, 1.37, 1.38, 1.39, 1.4 respectively, we obtained amplitude sensitivities and a maximum sensitivity of 4738.9 RIU^{-1} is achieved for the analyte refractive index of 1.4 in our case. Thus, the lowest amplitude sensor resolution it can offer is 2.11×10^{-6} RIU. This Amplitude Sensitivity is taken as the final result from our proposed sensor which is the best result it can produce to its capabilities.

6.7 Figure of Merit:

Another parameter that can describe the quality of the sensor is the Figure of Merit (FOM). FOM is characterized as the proportion of WS and FWHM (Full Width at Half Maximum) which is given below in equation (5.1). A better estimation of FOM is finalized when the sensitivity is high and FWHM is low. The FWHM obtained at refractive index of 1.35, 1.36, 1.37, 1.38, 1.39, 1.4, 1.41 are 23, 15, 20, 25, 20, and 37.5 for x-polarization respectively. The FWHM obtained at refractive index of 1.35, 1.36, 1.37, 1.38, 1.39, 1.4 and 1.41 are 18, 20, 20, 27, 28 and 22 respectively for y-polarization.

6.8 Sensor Length:

Sensor length is required to determine the power detected by the sensor at the output for input power. It can be computed by taking the inverse of the maximum confinement loss found in cm at each RI which is given in equation (6.1) [108].

$$L = \frac{1}{\alpha(\lambda, \Delta n_a)} \tag{6.1}$$

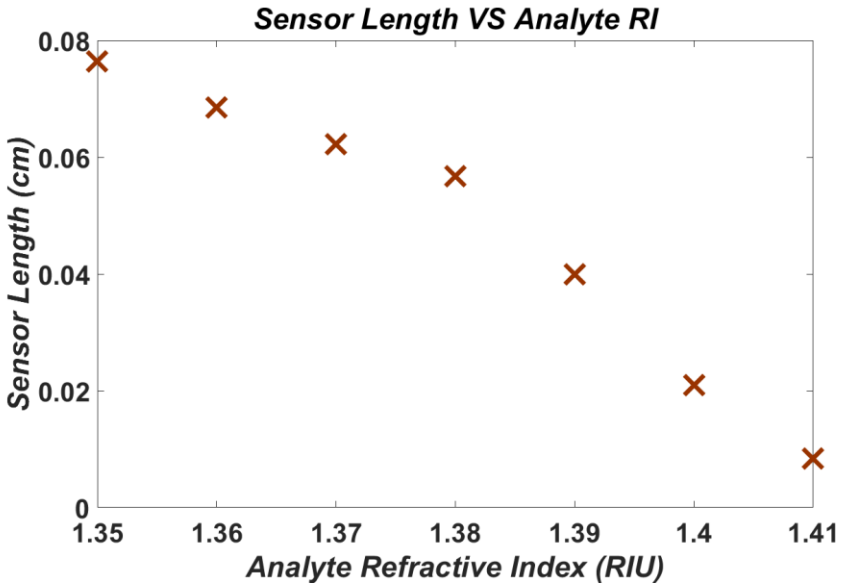

Figure 6-13: Sensor length at different Refractive Indices of Analyte RI.

Figure 6.13 depicts the sensor lengths at different analyte RI. Since it is inversely proportional to the confinement loss, the minimum loss gives the maximum sensor length applicable to the sensor.

6.9 Tabulation of sensing performance of parameters:

Table 6-1: Evaluation of the proffered sensor

Analyte RI	Peak Loss(dB/cm)	Resonant Peak Wavelength(nm)	Resonant Peak Shift (nm)	Amplitude Sensitivity(RIU^{-1}))	Wavelength Sensitivity(nm/RIU) In X-polarization	Wavelength Sensitivity(nm/RIU) In Y-polarization	FWHM (X-pol)	FWHM (Y-pol)	FOM(X-pol)	FOM(Y-pol)
1.35	13.08	560	10	336.5	2000	1000	23	18	86	55
1.36	14.59	570	20	404.908	2000	2000	15	20	133	100
1.37	16.08	590	20	643.45	2500	2000	20	20	125	100
1.38	17.63	610	40	971	3500	4000	25	27	140	148
1.39	25.01	650	40	1705	5000	4000	20	28	250	143
1.4	47.68	690	80	4738.9	14500	8000	37.5	22	387	364
1.41	118.4	770	N/A	N/A	N/A	N/A	12.5	10	N/A	N/A

Table 6.1 signifies the performance breakdown of the preferred sensor. In this table, we can see, with increasing RI, resonant peak shifts to the right just as our discussion in theory. In table 6.2, the correlation of performance of this sensor has been made with different reported sensors and the superiority of this proposed sensor has been established.

Table 6-2: Performance comparison with reported sensors

Ref. No	Structure Type	RI-range	Polarization mode	Amplitude Sensitivity (RIU^{-1})	Wavelength Sensitivity (nm/RIU)	Resolution (Wave. Int.) (RIU)	Resolution (Amp. Int.) (RIU)
[107]	A Hi-Bi ultra sensitive SPR	1.33-1.38	N/A	1411	25000	4.00×10^{-6}	7.09×10^{-6}
[101]	Localized SPR biosensor	1.33-1.43	N/A	2050	111000	9×10^{-7}	4.88×10^{-6}
[39]	Propagation controlled photonic crystal fiber	1.33-1.39	X-pol	1506	30000	3.33×10^{-6}	6.64×10^{-6}
[109]	Circularly slotted highly sensitive	1.40-1.46	N/A	780	16000	6.25×10^{-6}	1.28×10^{-5}
[110]	Multi-coating PCF SPR at near-infrared wavelength	1.40-1.44	N/A	1739.26	9600	1.04×10^{-5}	5.77×10^{-6}
[111]	Hollow core circular shaped PCF biosensor	1.33-1.42	N/A	2456	21000	4.76×10^{-6}	4.07×10^{-6}
[100]	Dual-polarized highly sensitive	1.33-1.4	N/A	1189.5	13000	7.69×10^{-6}	8.41×10^{-6}
Proposed Sensor	Gold coated Circular PCF SPR sensor	1.35-1.41	Y-pol	4738.9	8000 14500(X-pol)	1.25×10^{-5} $6.9\text{x}\ 10^{-6}$	2.11×10^{-6}

6.10 Conclusion

A novel highly amplitude sensitive gold-coated SPR sensor based on PCF has been redesigned and researched to detect three types of analytes that are- organic, biochemical, and biomedical. In-depth analysis and numerical simulation of the sensor exhibits optimum WS specifically for X polarization that is about 14500 nm/ RIU and the maximal AS of 4738.9 RIU^{-1} and the lowest amplitude sensor resolution of 2.11×10^{-6} RIU for Y-polarization mode, respectively in the range of 1.35 to 1.41 for the analyte refractive index (RI). FOM values of 387 and 364 are obtained for x and y polarization respectively. The lowest wavelength sensor resolution offered by this sensor is $6.9\text{x}10^{-6}$ RIU/nm. With existing advances, the manufacture of the sensor can be acknowledged directly alongside basic handy use. With existing technologies, the fabrication of the sensor can be realized straightforwardly along with simple practical utilization. Having such striking identifying properties, the proposed sensor has brilliant potential in the field of biomedicine, science, and for error-free and exact identification of other natural and biomedical applications.

Chapter 7

Simulation and Experimental Analysis of a gold-coated PCF-SPR biosensor for High-Temperature Sensing

7.1 Introduction

In this manuscript, we are theorizing the favorability of an SPR sensor possessing a dual-polarized, novel, and simple structure with circular air holes. The conception of this sensor was executed to consummate a fabrication-friendly configuration that resulted in a convenient set of attributes such as resolution, sensitivity, Figure of Merit, birefringence. The obtained results were authenticated by the implementation of the Finite Element Method through the software COMSOL Multiphysics 5.3a.

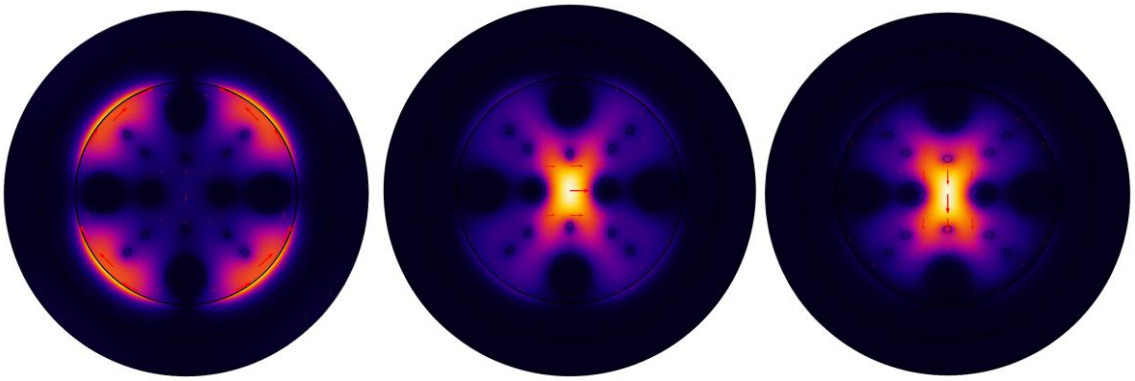

(a) (b) (c)

Figure 7-1: Light energy distribution of (a) SPP-mode, (b) core-guided mode X polarization,(c) core-guided mode Y-polarization.

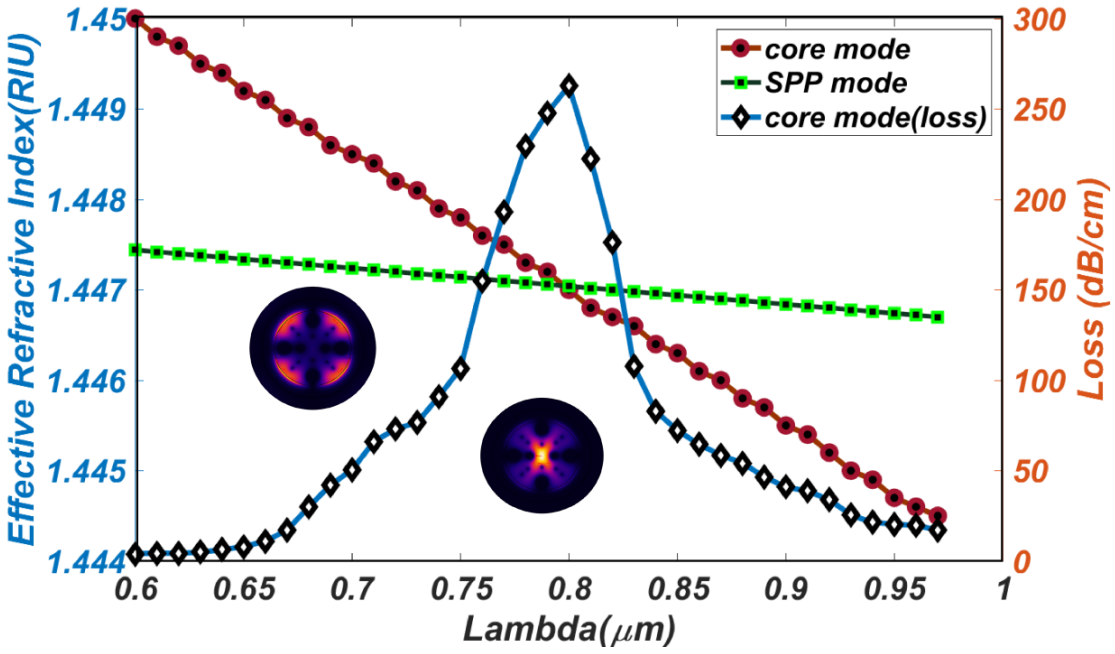

Figure 7-2: Dispersion relation of the proposed sensor.

Figure 7.1 characterized the fundamental modes of operation of the proposed sensor. The modes are Surface Plasmon Polariton (SPP) mode and Core-guided mode. In mathematical articulation, the resonance between the mentioned modes transpires with the equipoising of the real parts of effective refractive indices of the respective modes. This situation is explained as phase-matching. Phase matching is the expedient performance for the detection of refractive index. This phase matching or dispersion relation enables the sensor to detect analyte at the resonant wavelength which in this case is 800 nm. This dispersion relation is additionally unavoidable for the verification of the design. If there is no phase matching between the fundamental modes, the sensor fails to detect the test material. The phase-matching behavior of the suggested sensor is depicted in figure 7.2.

7.2 Design Methodology

The structure of the sensor being discussed has a plasmonic metal layer, an analyte layer, and a perfectly matched layer (PML) with circular air holes in its base layer illustrated in figure 7.3. The thicknesses of the overlays are defined by tg, andt_p. The base layer and the PML of the sensor were made up of Silica. Three different diameters have been used here for the airholes. The air holes have been positioned in a way that facilitates the light-guiding propagation for the tight confinement in the center as well as the formation of Surface Plasmon Waves (SPW) at the plasmonic layer. Gold has been chosen as the plasmonic material for its advantageous attributes. Analyte layer was positioned on the plasmonic layer for conventional detection. PML was then installed on the analyte layer for effectuating the computational boundary. The evaluation of the sensor was executed on the basis of the RI. Thereupon, wave-dependent relations of refractive index for the aforementioned layers were appointed. Silica's RI can be procured with the help of the empirical relation of wavelength and refractive index in the Sellmeier Equation illustrated in equation (4.4)

Equation (4.4) is appointed considering the assumption that the temperature in the environment of the sensor is constant and at 25^0C. A modified version of this equation is also available (equation 7.1) for correlating refractive index with variable wavelength and temperature. The refractive index for Gold is obtained from the Drude-Lorenz model given in equation (4.5)

The obtained mesh rendering from COMSOL for this sensor is also illustrated in figure 7.4. Rendering of mesh allows making the elements under investigation a set of finite elements for the ease of numerical analysis.

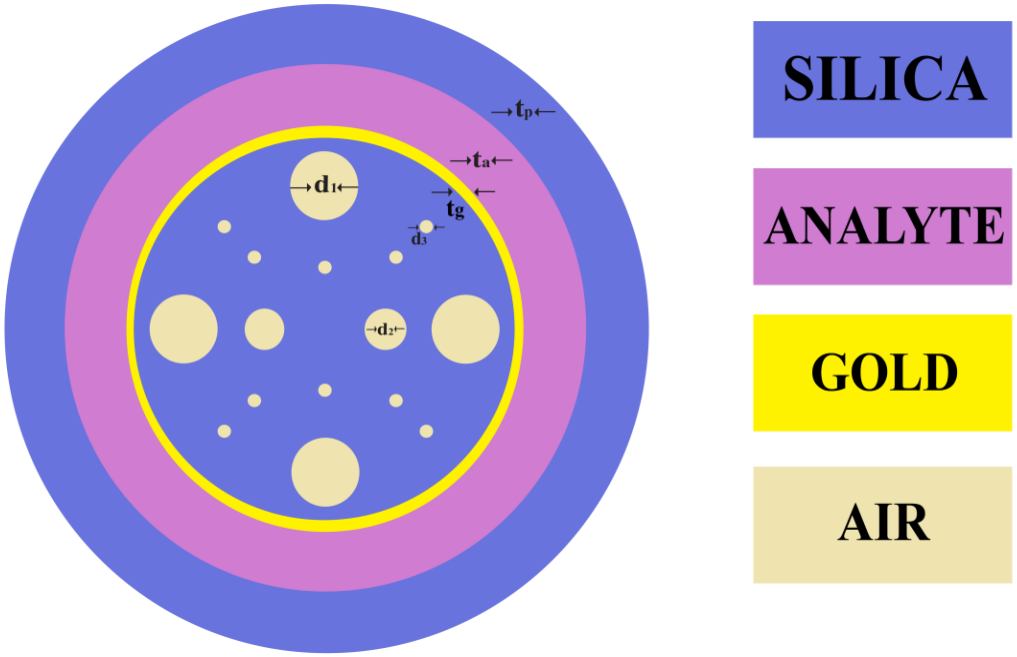

Figure 7-3: 2-D cross-sectional view of the proposed sensor.

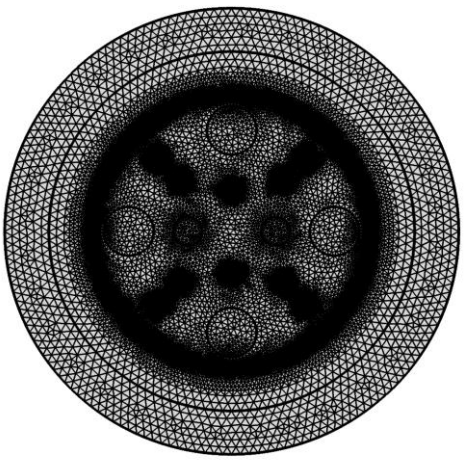

Figure 7-4: Meshing of the proposed structure.

7.3 Optimum parameters of the design

To achieve the desired attributes in the suggested sensor, numerical analysis is performed. Numerous studies have proved that optimizing the physical parameters in the sensors before doing numerical analysis provides better and improved results. In accordance with the opportunity of finding better results, optimization is encouraged. Our basis of optimization was the selection of parameters providing the best Amplitude Sensitivity (AS) assessing the loss spectra. The loss spectrum was calculated using equation (4.6). The amplitude sensitivity was formulated using equation (4.8). The AS is obtained through the amplitude interrogation method which is much more economic than the wavelength interrogation method. We can also find the sensitivity using wavelength interrogation from equation (4.7).

7.3.1 Gold Thickness

Sensing performance of an SPR sensor is impacted greatly by the thickness of the plasmonic material. A diminutive change in the thickness of plasmonic material results in a greater shift in resonance wavelength which affects the sensitivity. Again, a thick layer of plasmonic material fails to produce the desired evanescent field. [112]. Thus, it is of utmost importance to optimize the thickness of this layer. For our purpose, we varied the values by $\pm$20% of the initial to notice the change in the amplitude sensitivity. We examined the change by computing results from two values of refractive indices (1.39 and 1.4). Figure 7.5 illustrates the effect of varying gold thickness. Increasing the thickness from the initial value of 30 nm resulted in a drastic diminishing in sensitivity and below 25 nm thickness, sensitivity also reduced drastically. Thus we decided upon 25 nm as the optimum thickness. Table 7.1 depicts the variation in AS with the alteration of gold thickness t_g

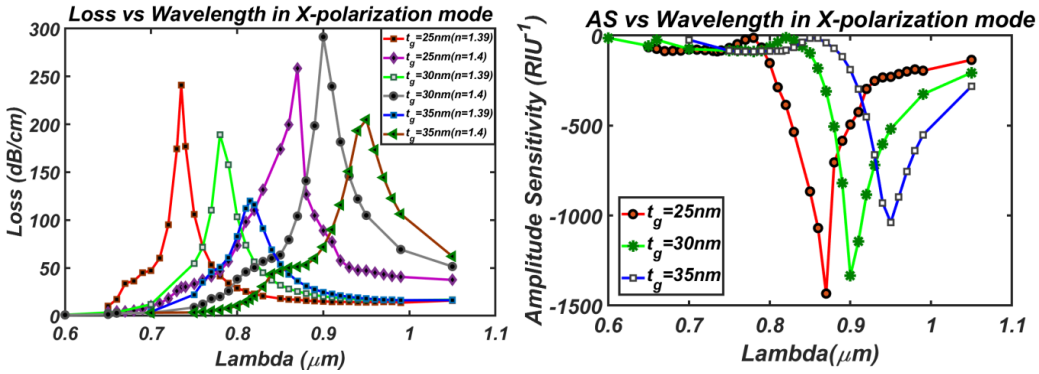

(a) (b)

Figure 7-5: (a) CL for varying gold thickness (t_g), (b) AS for varying gold thickness (t_g).

Table 7-1 : Obtained values of as for altering gold thickness, t_g

Thickness (t_g) (nm)	Amplitude Sensitivity (RIU^{-1})	Analyte RI (RIU)
25	1433	1.39 1.4
30	1334	1.39 1.4
35	1038	1.39 1.4

7.3.2 Analyte Thickness

The analyte in the sensor represents the material to be detected. This layer is situated just above the plasmonic layer for the facilitation of detection. To be able to detect the test material accurately, its thickness must be optimized. Otherwise, detection of analyte's refractive index and hence the corresponding material will prove to be erroneous. We varied the thickness of this layer by $\pm 33.33\%$from the initial value keeping the value of gold thickness at its optimum value (25 *nm*) to notice the change in AS. Our findings suggested that the initial value of 1.5 μm should be the optimum value of the thickness. Figure 7.6 illustrates the effect of varying the analyte thickness and table 7.2 contains the obtained values in this process.

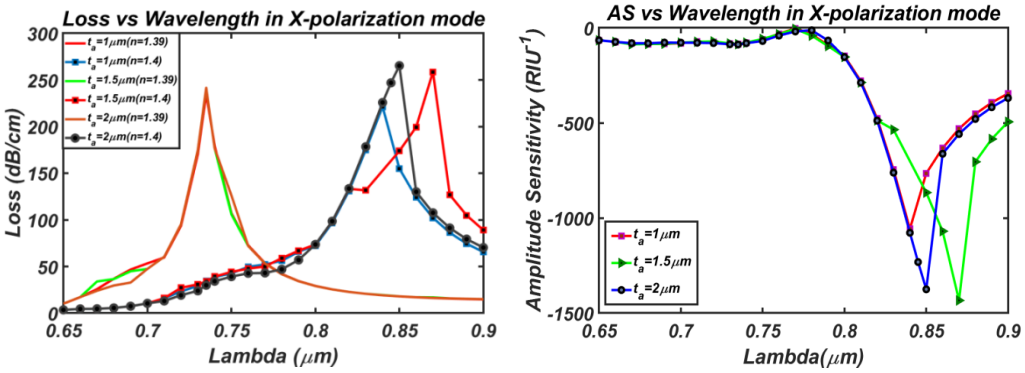

(a) (b)

Figure 7-6: (a) CL for varying analyte thickness (t_a), (b) AS for varying analyte thickness (t_a).

Table 7-2: Obtained values of as for altering analyte thickness, t_a

Thickness (t_a) (μm)	Amplitude Sensitivity (RIU^{-1})	Analyte RI (RIU)
1	1057	1.39 1.4
1.5	1433	1.39 1.4
2	1375	1.39 1.4

7.3.3 PML (Perfectly Matched Layer) Thickness

PML or Perfectly Matched Layer serves as a fictitious gripping layer used when wave equations are employed for computation. It is a mere computational boundary to prevent facing problems with open boundary conditions associated with mathematical computation such as the Finite Element Method (FEM) in this case. Its thickness should be optimized to give the boundary an opportunity to absorb the outgoing waves. This layer is not imperative to the enhancement of sensitivity which can be realized from figure 7.7 and table 7.3. However, it still needs optimization. Figure 7.7 interprets the effect of PML and we can see negligible effects by comparing figure 7.6. Table 7.3 showcases the values obtained for this analysis.

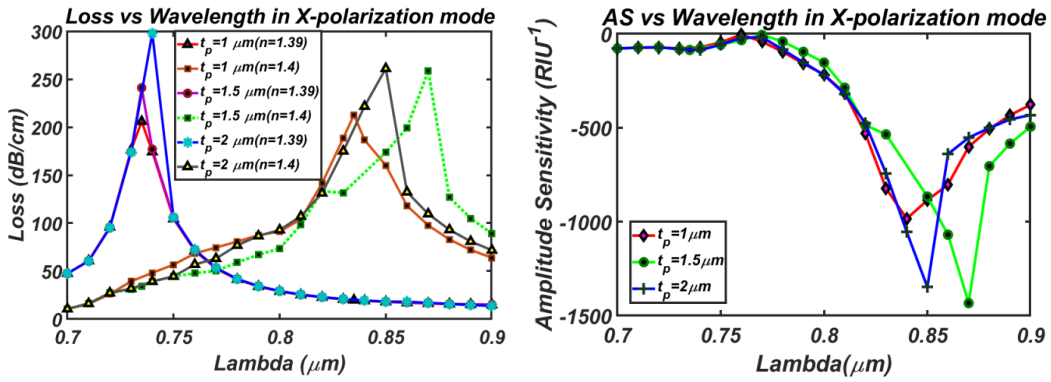

(a) (b)

Figure 7-7: (a) CL for varying PML thickness (t_p), (b) AS for varying PML thickness (t_p).

Table 7-3: Obtained values of as for altering PML thickness, t_p

Thickness (t_p) (μm)	Amplitude Sensitivity (RIU^{-1})	Analyte RI (RIU)
1	984	1.39 1.4
1.5	1433	1.39 1.4
2	1348	1.39 1.4

7.4 Sensing performance

The sensing performance of a sensor can be scrutinized by contemplating the resulting parameters from that particular sensor. Various criteria for enhanced sensor performance are resolution, sensitivity, birefringence, Figure of Merit, and many more. The analysis of these attributes is discussed below.

7.4.1 Effect of Variation of Refractive Index of Analyte

Analyte RI has the most significant effect on an SPR sensor's sensitiveness. To assess the behavior of the sensor due to dynamic values of the refractive index, the sensor was checked with the obtained optimum parameters. The RI range varied from 1.34 to 1.4 RIU. The phase alignment of core mode and SPP mode enables the sensor to provide a condition for maximum power transfer. As a result, the sensor becomes sensitive to changes. Successively with accreting analyte RI, an increasing loss spectrum is observed. This indicates that the sensor is being able to detect losses more accurately and hence is sensitive to that particular RI. In consequence, the resonant wavelength or the wavelength at which the maximum loss was found, shifts to right with the advancing RI. From our analysis, we can see for both polarizations, in figure 7.8 and 7.9, maximum loss spectrum was found at the analyte RI 1.4 which produced the maximum obtained sensitivity for both amplitude and wavelength interrogation.

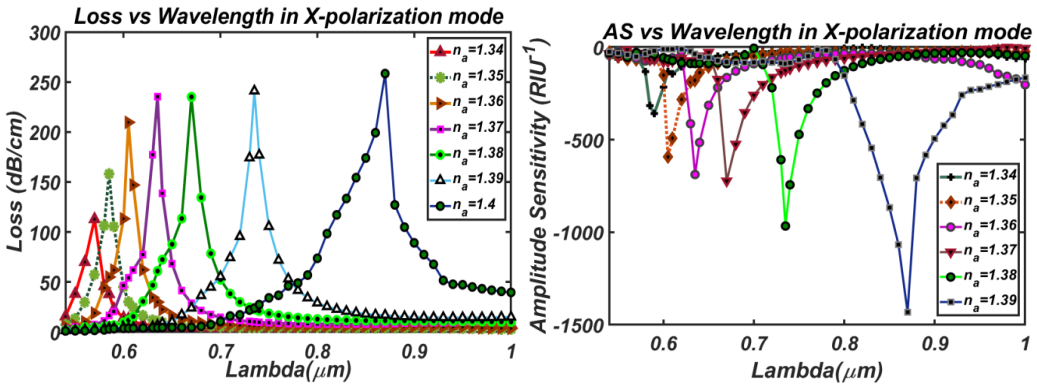

(a) (b)

Figure 7-8: (a) Loss vs Wavelength for different RI, (b) AS vs Wavelength for different RI in X-polarization.

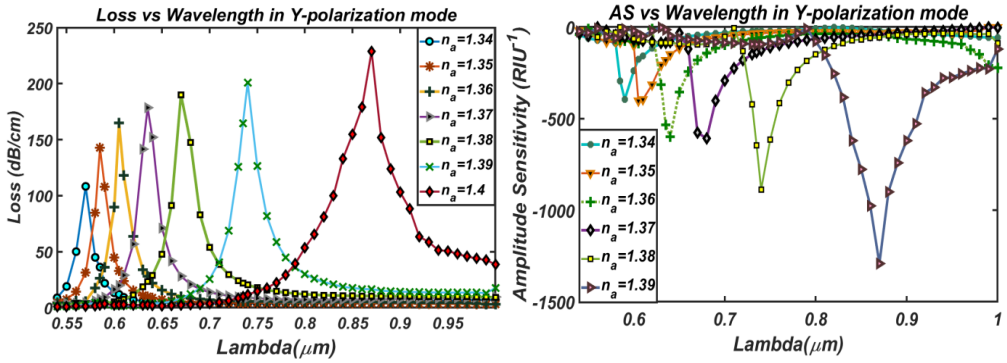

(a) (b)

Figure 7-9: (a) Loss vs Wavelength for different RI, (b) AS vs Wavelength for different RI in Y-polarization.

On the grounds of being able to detect incurred losses by being sensitive, x-polarization transcended y-polarization.

7.4.2 Curve Fitting

Determination of curve fitting of any sensor has proved to be of high importance for being able to realize the behavior of that sensor. A 3rd order fitting on the obtained values of resonant wavelength for each RI has been employed that resulted in a high regression of 0.9972. The characteristic equation for the fitting can be found from the coefficients which are $[y = 2 \times 10^6 x^3 - 10^7 x^2 + 10^7 x - 6 \times 10^6]$ and $R^2 = 0.9972$

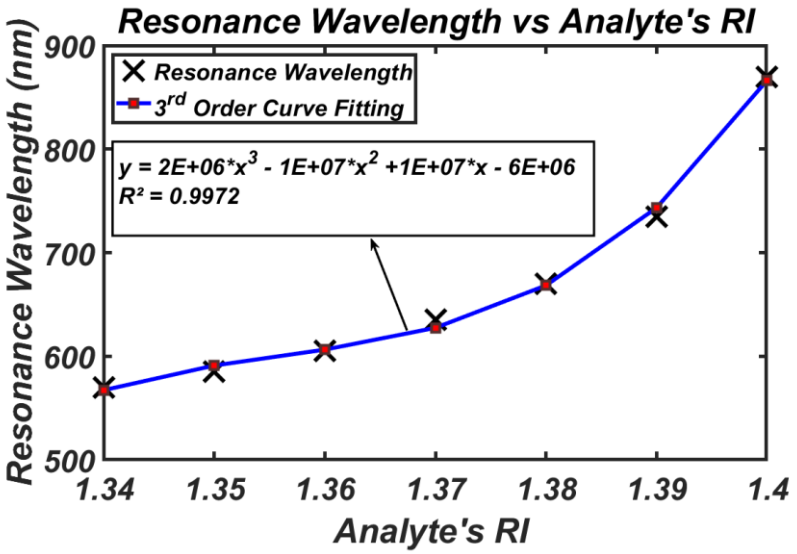

Figure 7-10: Curve Fitting with regression=0.9972.

7.4.3 Resolution

Precise detection of the minimum spectral shift change, which detects analytes properly, is very crucial for the characterization of any sensor to be an efficient one. In the implicated sensor, an average wavelength shift of 50 nm was found for both polarizations in the RI range 1.34-1.4. Resolution can be detected following both methods of interrogations. Resolution by the method of wavelength interrogation conceivably is measured by the equation (4.9). Following equation (4.9), a minimum resolution of $7.407 \times 10^{-6} RIU$was found for x-polarization and that for y-polarization was$7.6923 \times 10^{-6} RIU$. Resolution can also be found by amplitude method of interrogation where we use the given relation in equation (4.10) for computing the resolution [112]. Employing equation (4.10), we obtained minimum resolution of $6.9832 \times 10^{-6} RIU$ and $7.74593 \times 10^{-6} RIU$ for x-polarization and y-polarization respectively.

7.4.4 FOM

A figure of Merit or FOM is the correlation amid the wavelength sensitivity and FWHM (Full Width at Half Maximum) of a sensor at a particular RI. FWHM is obtained by taking the width (in nm) between the points of intersection of half the value of peak loss at each RI. Figure 7.11 depicts the values of FWHM obtained at various RI. Table 7.4 and 7.5 also contain the numerical values of FWHM for both polarizations. FOM can be computed by equation (5.1) [112].

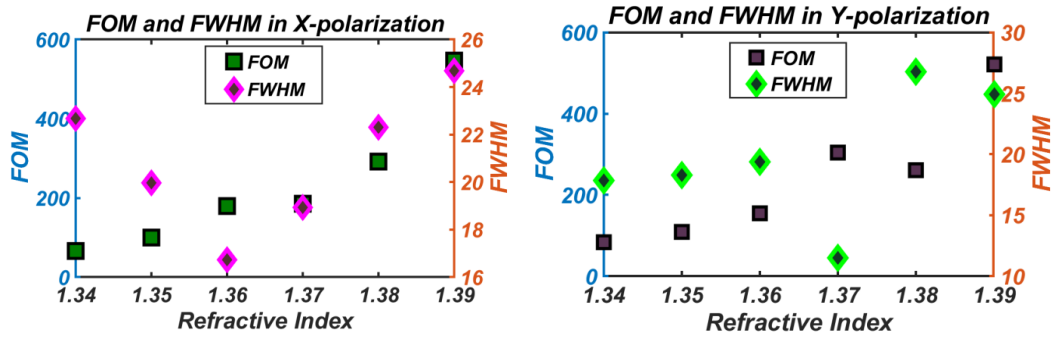

(a) (b)

Figure 7-11: (a) FOM and FWHM values in X-polarization, (b) FOM and FWHM values in Y-polarization for different RI.

A maximum FOM value of 546.93 in x-polarization and that of 521.4601 in y-polarization were obtained. Evidently from the equation 7.8, FOM is related to WS directly and inversely to FWHM. Thus a high value FOM can be deduced by the contribution of a high WS value and a low FWHM value. Our obtained FOM value can be considered as an indication of advanced sensitivity since it is a very high value.

7.4.5 Sensor Length

Sensor length depicts inverse relation with resonant wavelength since it is obtained by inverting the peak loss for each RI. It is cast by the equation (6.1) **[**108].

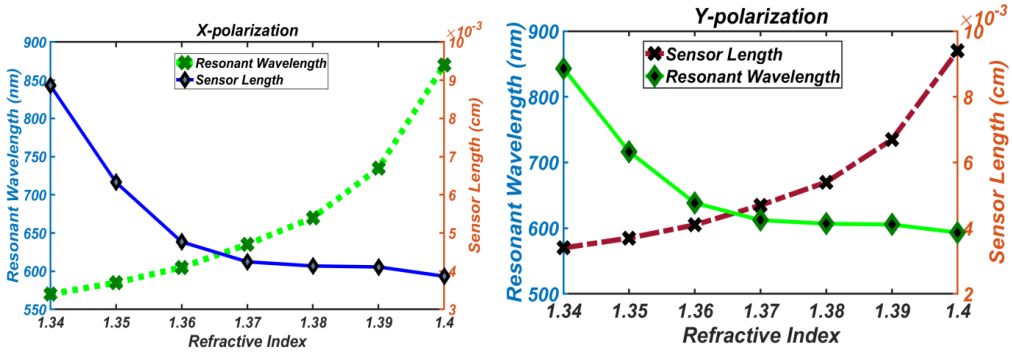

(a) (b)

Figure 7-12: Sensor Length at (a) X-polarization and (b) Y-polarization

Figure 7.12 portrays the sensor length variation for our analyzed refractive indices and also the resonant wavelength for each RI. We obtained a maximum sensor length of 0.008865 cm in x-polarization and 0.009233 cm in y-polarization.

7.4.6 Birefringence

Birefringence is defined as the difference in polarization of two modes of polarization (x and y). It is quantified as the absolute value of the contrast between the real part of refractive indices in x-polarization and y-polarization that is shown

in equation (2.3). A high birefringence value assists the input signal to maintain the polarization state [85].

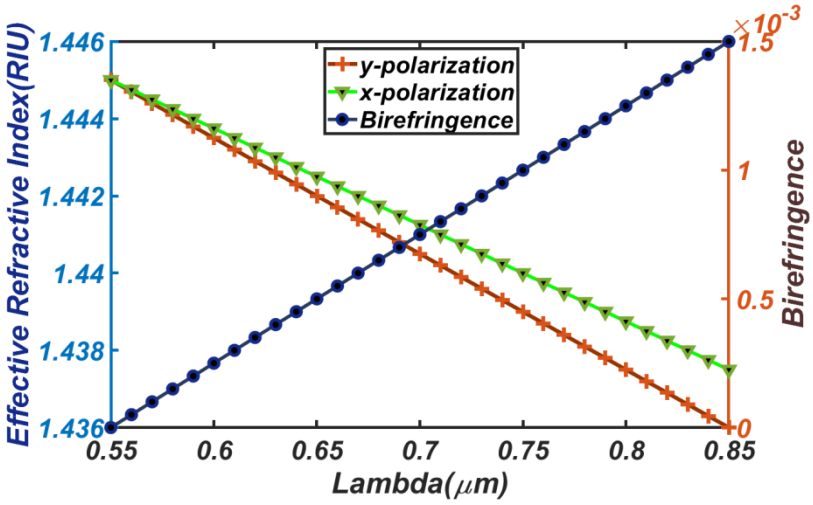

Figure 7-13: Birefringence with varying wavelength at RI=1.39.

A maximum birefringence value of 0.0015 was found for the proposed sensor at wavelength 850 nm for refractive index 1.39. Figure 7.13 depicts the birefringence behavior at the RI=1.39. It is evident that when the real parts of effective refractive indices for both polarizations are identical, a birefringence of value zero was obtained at 550 nm. Contrariwise, the highest birefringence was found for the maximum difference between the aforementioned values.

7.5 Tabulation of results

Table 7.4 illustrates the obtained parameters by investigating our sensor for the analyte RI in the range of 1.34-1.4 in x-polarization. Maximal AS of 1432 RIU^{-1} and maximal WS of 13500 nm/RIU were found at RI=1.39. A maximum FOM of 546.93 was also found.

Table 7-4 : Performance analysis of the suggested sensor in x-polarization

Analyte RI	Peak Loss (dB/cm)	Resonant Peak Wavelength (nm)	Resonant Peak Shift (nm)	Amplitude Sensitivity X-pol (RIU^{-1})	Wavelength Sensitivity (nm/RIU) X-pol	FWHM (X-pol)	FOM (X-pol)
1.34	112.8	570	15	-358	1500	22.678	66.143
1.35	158	585	20	-593	2000	19.968	100.16
1.36	209.7	605	30	-688	3000	16.722	179.40
1.37	235.5	635	35	-746	3500	18.935	184.84
1.38	241.7	670	65	-966	6500	22.31	291,35
1.39	243.2	735	135	-1432	13500	24.683	546.93
1.4	258.5	870	N/A	N/A	N/A	N/A	N/A

Table 7.5 illustrates the obtained parameters by investigating our sensor for the analyte RI in the range of 1.34-1.4 in y-polarization. Highest AS of 1291 RIU^{-1} and highest WS of 13000 nm/RIU were found at RI=1.39. A maximal FOM of 521.4601 was also found.

Table 7-5 : Performance breakdown of the intended sensor in y-polarization

Analyte RI	Peak Loss (dB/cm)	Resonant Peak Wavelength (nm)	Resonant Peak Shift (nm)	Amplitude Sensitivity Y-pol (RIU^{-1})	Wavelength Sensitivity(nm/RIU) Y-pol	FWHM (Y-pol)	FOM (Y-pol)
1.34	108.2996	570	15	-394	1500	17.842	84.0713
1.35	142.7929	585	20	-563	2000	18.29	109.3494
1.36	168.7431	605	30	-608	3000	19.37	154.88
1.37	171.5342	635	35	-791	3500	11.491	304.5862
1.38	190.0778	670	70	-887	7000	26.78	261.3891
1.39	200.8912	740	130	-1291	13000	24.93	521.4601
1.4	228.7019	870	N/A	N/A	N/A	N/A	N/A

7.6 Temperature sensing

We now investigate our sensor's sensitivity performance depending on temperature by replacing the analyte with ethanol. Earlier our analysis had the assumption that the sensor did not encounter temperature change apart from the room temperature. Temperature sensitivity is an additional advantage to an SPR sensor. It provides a perception of a particular sensor is sensitive to a certain range of temperature rather than being sensitive to one single temperature. This presents the opportunity to detect analytes at various temperatures using a single sensor.

We chose Ethanol as our test material to assess the temperature sensitivity. Ethanol has a melting point and boiling point of -114.1°C and 78.37 °C. The mentioned temperature range reciprocates an RI range of approximately 1.343 to 1.41. Thus appointing Ethanol as the analyte for this analysis is homogenized with our earlier analysis in terms of refractive index. Fused silica melts at about 1670 °C making the detection range have little to no effect on the fiber's properties. To investigate the sensor with temperature-dependent characteristics, we need to appoint a temperature-dependent equation to compute the refractive indices of materials. Temperature-dependent materials being used here are Silica and Ethanol. The temperature-dependent equation for silica is a modified version of the previously used Sellmier's Equation. It is depicted in equation (7.1) [113].

$$n_{Si}^2(\lambda,T) = (1.31552 + 6.90754 \times 10^{-6}T) + \frac{(0.788404 + 23.5835 \times 10^{-6}T)\lambda^2}{\lambda^2 - (0.0110199 + 0.584758 \times 10^{-6}T)} + \frac{(0.91316 + 0.548368 \times 10^{-6}T)\lambda^2}{(\lambda^2 - 100)} \quad (7.1)$$

Temperature dependent equation for Ethanol is given in equation (7.2).

$$n_1 = n_0 + \frac{dn}{dT}(T_1 - T_0) \quad (7.2)$$

where n_1 and n_0 are the RI at temperatures T_1 and T_0, respectively. RI of ethanol is n_0 = 1.361 at T_0= 20 ^{0}C. $\left(\frac{dn}{dT}\right)$typifies the thermo optical coefficient which is quantified as - 3.117 × 10^{-4} °C^{-1} [99].
Temperature sensitivity can be computed by equation (7.3).

$$S_\lambda = \frac{\delta\lambda_{peak}}{\delta T}(nm/°C) \quad (7.3)$$

$\delta\lambda_{peak}$ denotes the resonant wavelength shift and $\delta T$is the temperature interval taken for the analysis. An interval of 24°C in this was applied to divide the temperature range into 9 values of temperature (-114°C, -90°C, -66°C, -42°C, -18°C, 6°C, 30°C, 54°C, and 78°C). Resolution for Temperature sensitivity can also be calculated using equation (7.4).

$$R_T = \delta T \times \frac{\delta\lambda_{min}}{\delta\lambda_{peak}}(^oC) \quad (7.4)$$

In consideration of the previous analysis, x-polarization is chosen with the intention of obtaining a surpassing result. The loss spectra were formulated using the equation appointed in the earlier analysis (equation 7.3). Figure 7.14 demonstrates the loss variation for every temperature.

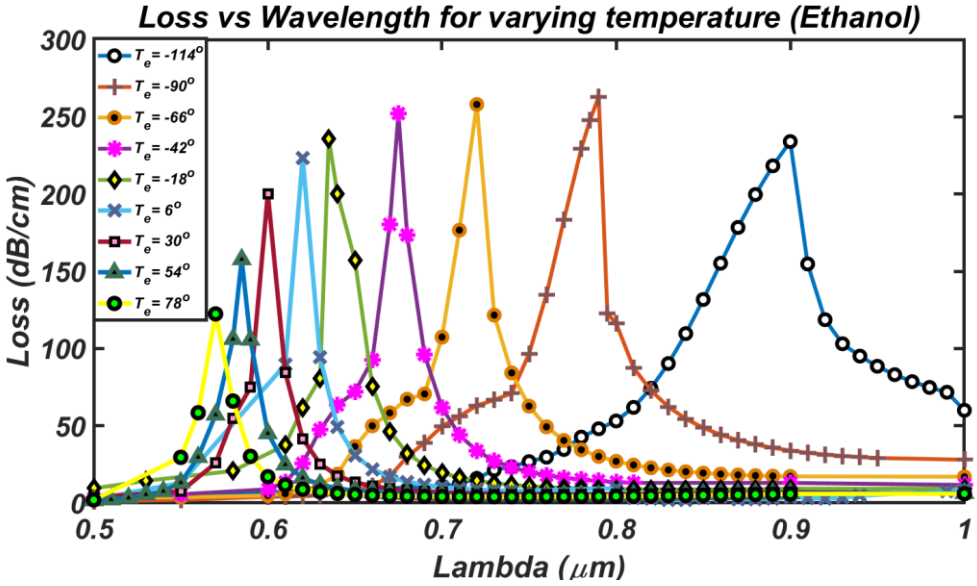

Figure 7-14: Loss vs Wavelength for a varying temperature of Ethanol.

It is noticeable from figure 7.14 that peak loss for the lowest temperature in our chosen range is situated at the highest wavelength and the peak for the highest temperature is at the lowest wavelength. With the increasing wavelength, a larger shift in resonant wavelength is found. A maximum shift of 110 nm was found at T_e=78°C. By following equation 7.13, maximum temperature sensitivity for the suggested sensor in this work was found to be 4.5833nm/°C. Table 7.6 demonstrates the effect of increment of temperature.

Table 7-6: Performance breakdown of the proffered sensor due to fluctuation in temperature in analyte medium (ethanol)

Temp ($°C$)	**Corresponding RI *(RIU)***	**Resonant Wavelength *(nm)***	**Peak Shift *(nm)***	**Peak loss *(dB/cm)***	**Temperature Sensitivity ($nm/^0\,C$)**	**Resolution (^oC)**
-114	1.4028	900	110	233	4.5833	0.0218
-90	1.3953	790	70	262.9	2.9167	0.03428
-66	1.3878	720	45	257	1.875	0.0533
-42	1.3803	675	40	252.1	1.667	0.0599
-18	1.3728	635	15	235.8	0.625	0.16
-6	1.3654	620	20	232.2	0.833	0.12
30	1.3579	600	15	200.2	0.625	0.16
54	1.3504	585	15	157.7	0.625	0.16
78	1.3426	570	N/A	122.4	N/A	N/A

Figure 7.15 illustrates the behavior of the proposed sensor's sensitivity to different temperatures and attests to the fact that this sensor will give diminished sensitivity at increased temperatures.

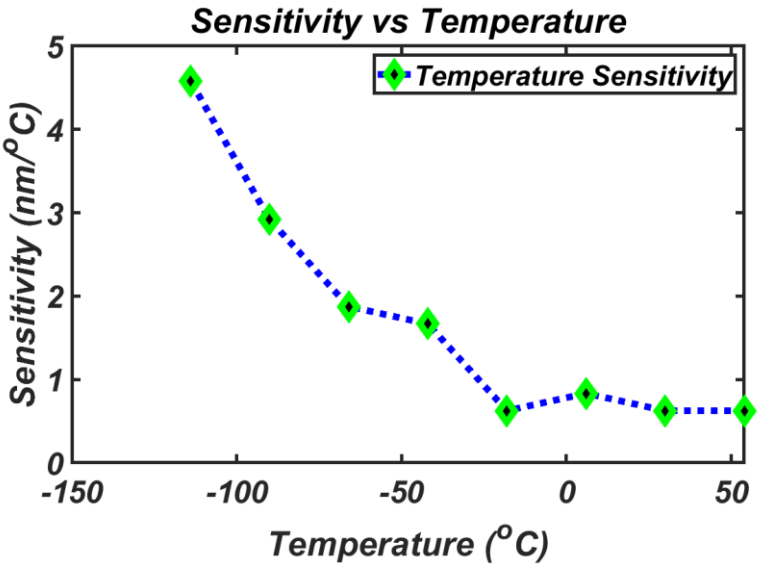

Figure 7-15: Temperature Sensitivity obtained at various temperatures.

A polynomial fitting demonstrates the behavior of this sensor's resonant wavelength for varying temperatures. A regression of 0.9991 was found which is very close to 1. Thus, a third-order fit is an excellent fitting in determining the behavior of the sensor. From figure 7.16, we can deduce that at the higher temperature, the resonant wavelength will shift to the left and thus result in lower sensitivity.

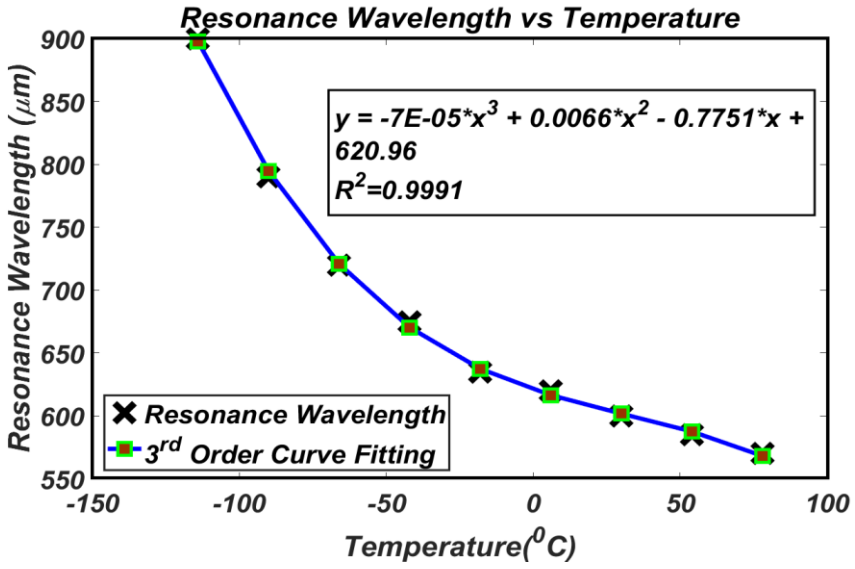

Figure 7-16: Curve fitting for resonant wavelength at different temperatures.

A comparison of the obtained results with that of few previously reported sensors has been performed to attest to the favorability of the proposed sensor. The comparison is given in Table 7.8.

Table 7-7: Distinction of suggested Temperature sensor with the existing sensors

Ref. No	Detecting Range (℃)	Sensor Resolution (℃)	Sensitivity ($nm/$℃)	Plasmonic Material and Analyte
[114]	0-50	N/A	0.72	Gold and Liquid
[115]	0-100	N/A	0.72	Gold and Ethanol
[99]	-70-70	1.33×10^{-1}	0.75	Gold and Ethanol
[116]	0-50	5×10^{-2}	2.0	Gold and Benzene
[116]	60-90	4×10^{-2}	2.5	Gold and CS_2
Our Proposed Sensor	-114 -78	2.18×10^{-2}	4.5833	Gold and Ethanol

7.7 Conclusion

We proposed a simple gold coated SPR based PCF for our research purpose. Gold was given priority due to its numerous advantages over other plasmonic material. Perfectly matched layer was chosen so that light could not get out of the fiber. We optimized each parameter while keeping the other parameters constant. All the numerical analysis was conducted by using Finite Element Method. Our proposed sensor gave us the highest AS of 1432nm/RIU and highest wavelength of 13,500 RIU^{-1} and FOM of 546.93 for x polarization. In the y polarization it gave us highest AS of 1291 RIU^{-1}, highest WS of 13000 nm/RIU and FOM of 521.4601.The RI range was varied from 1.34 to 1.4. For further analysis we varied the temperature to observe whether our proposed sensor can sustain a change in environment or not. For this purpose we chose ethanol as the sensing medium. Temperature sensitivity for varying temperature within range -114 to 78℃ was 4.5833 nm/℃.Thus it can be concluded that our sensor gives good performance even if the temperature is changed. From the performance breakdown we can say that our sensor can be used for sensing applications.

Chapter 8

Conclusion and Future work

8.1 Conclusion

By analyzing our proposed sensors we can say that the performance offered by them is appreciable. In our first proffered sensor the highest AS is 1779 RIU^{-1} which is higher compared to other sensors. The loss is very low in our proposed sensor. In addition a birefringence of 0.0049 and FOM value 187.5 have been obtained. Due to its strong sensing characteristics, the analyzed sensor will be beneficial for problem-solving time diagnostic applications for example: control and biological analyte identification. This sensor may be used for a variety of bio-sensing experiments.

From our second proposed sensor gave WS for of 14,500 nm/ RIU and the maximum amplitude sensitivity of 4738.9 RIU^{-1} for X-polarization and the lowest amplitude sensor resolution of 2.11 $\times 10^{-6}$ RIU for y-polarization mode, respectively in the range of 1.35 to 1.41. FOM values of 387 and 364 were obtained for x and y polarization conjointly. Comparing with other outcomes, we can say that this sensor gave improved AS and WS. The fabrication of the proposed design as well as its practical use can be accomplished easily using current technologies. The developed method provides amazing opportunities in the fields of biomedicine, physics, and error-free and exact identification of many other natural and biomedical applications due to its remarkable identification characteristics.

Our last proposed design gave the AS of 1432 RIU^{-1} and 1291 RIU^{-1} in X and Y polarized mode reciprocally. It also gave a WS of 13,500 and 13,000 in X and Y polarized mode respectively. Sensor resolutions of 7.407×10^{-8} and 7.692310^{-8} were obtained using wavelength interrogation method and 6.983210^{-6}, 7.7459310^{-6} were obtained by using amplitude interrogation method in Y and X polarized mode reciprocally. FOM value of 521.4601 and 546.93 were obtained for X and Y polarization method. A birefringence of 0.0015 was procured for the proposed sensor. Temperature sensitivity for temp range (-114 to 78℃) was 4.5833 nm/℃. So after observing the results of our proposed sensors we can say that our sensors can be used for sensing purposes.

8.2 Future work

Throughout the thesis work, we have inspected different PCF-based SPR biosensor which is coated with the effective plasmonic material (Gold) which gives us better-sensing performance in our optimized result. We have used Silica (SiO_2) as a bulk material to get the proper sensing characteristics. Therefore, a computational analysis must be performed to correctly choose the parameters and then provide an optimization. Due to this COVID situation all over the world, we were not able to do our thesis work smoothly and physically. But we have tried to explore our field of research as much as we could. We were not able to finish some of our thesis work due to scarcity of time in a pandemic situation and other technical compulsion. So, we have decided to work soon on the following works by making competent variations,

- Explore the use of different plasmonic materials
- Explore different lattice structures and making a comparison of previously done work
- Explore the effects of strain on PCF-SPR sensors
- Explore the effect of adding a different adhesive layer in the sensor
- Explore the effect of Temperature with other material as the analyte layer
- Improving sensitivity by metal grating
- Improving the fabrication process in design

References:

1. Homola, J., Surface Resonance Sensors for Detection of Chemical and Biological Species. Chem. Rev., 108(2): p. 462-493, 2008.
2. Rich, R.L. and D.G. Myszka, Survey of the year 2005 commercial optical biosensor literature. Journal of Molecular Recognition, 19(6): p. 478-534, 2006.
3. V. V. Ravi Kanth Kumar et al., "Extruded soft glass photonic crystal fiber for ultrabroad supercontinuum generation", Opt. Express 10 (25), 1520 (2002).
4. H. Ebendorff-Heidepriem et al., "Suspended nanowires: fabrication, design and characterization of fibers with nanoscale cores", Opt. Express 17 (4), 2646 (2009).
5. D. Ferrarini, L. Vincetti, M. Zoboli, A. Cucinotta, and S. Selleri, "Leakage properties of photonic crystal fibers," Optics Express, vol. 10, no. 23, pp.1314-1319, 2002.
6. J.C. Knight, T.A. Birks, P.St.J. Russell, D.M. Atkin, Opt. Lett. 21, 1547 (1996).
7. J.C. Knight, J. Broeng, T.A. Birks, P.S. Russel, Science 282, 1476 (1998).
8. M. A. Habib and M. S. Anower, "A Novel Low Loss Porous-Core Photonic Crystal Fiber for Terahertz Wave Transmission," in International Conference on Electrical, Computer and Communication Engineering (ECCE), Cox's Bazar, Bangladesh, 2017.
9. Md. Allama Ikbal, M. Hasnat Kabir, "Reduction of effective material loss in porous core hexagonal lattice fiber," Optik, volume 225, 165777, january 2021.
10. R. Islam, G. K. M. Hasanuzzaman, M. S. Habib, S. Rana, and M. A. G. Khan, "Low-loss rotated porous core hexagonal single-mode fiber in THz regime," Opt. Fiber Technol., vol. 24, pp. 38–43, 2015.
11. LeiYao, Shuqin Lou, Hung Fang, Tieying Guo, Hunglei Li and Shuisheng Jian, "Tailoring confinement losses of photonic crystal fibers", Optical fiber communication and optoelectronics conference, pp. 445-447, Shanghai, 2007.
12. Trolier-McKinstry, S., Fox, G. R., Kholkin, A., Muller, C. A. P. and Setter, N., "Optical fibers with patterned ZnO/electrode coatings for flexural actuators" Sensors and Actuators A: Physical 73(3), 267-274, 1999.
13. Chiu, M. H., Wang, S. F. and Chang, R. S., "D-type fiber biosensor based on surfaceplasmon resonance technology and heterodyne interferometry," Optics Letters 30(3), 233-235, 2005.
14. Cox, F. M., Lwin, R., Large, M. C. J. and Cordeiro, C. M. B., "Opening up optical fibres," Optics Express 15(19), 11843-11848, 2007.
15. Allsop, T., Reeves, R., Webb, D. J., Bennion, I. and Neal, R., "A high sensitivity refractometer based upon a long period grating Mach-Zehnder interferometer," Review of Scientific Instruments (73), 1702-1705, and 2002.
16. Nelson, D. F. et al. Vibration-induced modulation of fiberguide transmission. Proc. Topical Meeting on Optical Fiber Transmission. TU-E7-I to TU-E7–4.
17. Fields, J. N. et al. (1980) Fiber optic pressure sensor. J. Acoust. Soc. Am., 67, 816–818.
18. Fields, J. N. (1980) Attenuation of a parabolic-index fiber with periodic bends. Appl. Phys. Lett., 36, 799–801.
19. KretschmannE, R. (1968). Radiativedecayofnon radiative surface plasmons excited by light. Z Naturforsch, 23, 2135–2136.
20. Knoll, W. (1998). Interfaces and thin films as seen by bound electromagnetic waves. Annual Review of Physical Chemistry, 49(1), 569-638.
21. Dash, J. N., & Jha, R. (2014b). SPR Biosensor Based on Polymer PCF Coated With Conducting Metal Oxide. IEEE Photonics Technology Letters, 26(6), 595-598.

22. R.C. Jorgenson, S.S. Yee, A fiber-optic chemical sensor based on surface plasmon resonance, Sens. Actuators B: Chem. 12 (1993) 213–220.
23. A. A. Rifat, G. A. Mahdiraji, Y. G. Shee, M. J. Shawon, and F. R.M.Adikan, " A novel photonic crystal fiber biosensor using surface plasmon resonance,'' Procedia Engineering, vol. 140, pp. 1–7, 2016.
24. C. Liu, L. Yang, W. Su, F. Wang, T. Sun, Q. Liu, H. Mua, and P. K.Chu, "Numerical analysis of a photonic crystal fiber based on a surface plasmon resonance sensor with an annular analyte channel,''Optics Communications, vol. 382, pp. 162–166, 2016.
25. F. Wang, Z. Sun, C. Liu, T. Sun, and P. K. Chu, "A highly sensitive dual-core photonic crystal fiber based on a surface plasmon resonance biosensor with silver-graphene layer,'' Plasmonics, pp. 1–7, 2016.
26. A. A. Rifat, R. Ahmed, A. K. Yetisen, H. Butt, A. Sabouri, G. A. Mahdiraji, S. H. Yun, and F. R. M. Adikan ,"Photonic crystal fiber based plasonic sensors,'' Sensors and Actuators B, vol. 243, pp. 311–325,2016.
27. X. Yu, Y. Zhang, S. Pan, P. Shum, M.Yan, Y. Leviatan, and C. Li, " A selectively coated photonic crystal fiber based surface plasmon resonance sensor, " Journal of Optics, vol. 12, pp. 1–4, 2009.
28. D. J. J. Hu and H. P. Ho, "Recent advances in plasmonic photonic crystal fibers: design, fabrication and applications," Adv. Opt. Photon. 9, 257–314 (2017).
29. G. H. Li, X. S. Chen, O. P. Li, C. X. Shao, Y. Jiang, L. J. Huang, B. Ni, W. D. Hu, and W. Lu, "A novel plasmonic resonance sensor based on an infrared perfect absorber," J. Phys. D 45, 205102 (2012).
30. J. G. Ortega-Mendoza, A. Padilla-Vivanco, C. Toxqui-Quitl, P. Zaca-Morán, D. Villegas-Hernández, and F. Chávez, "Optical fiber sensor based on localized surface plasmon resonance using silver nanoparticles photodeposited on the optical fiber end," Sensors 14,18701–18710 (2014).
31. L. B. Sagle, L. K. Ruvuna, J. A. Ruemmele, and R. P. V. Duyne, "Advances in localized surface plasmon resonance spectroscopy biosensing," Nanomedicine 6, 1447–1462 (2011).
32. A. A. Rifat, M. R. Hasan, R. Ahmed, and H. Butt, "Photonic crys-tal fiber-based plasmonic biosensor with external sensing approach,"J. Nanophoton., vol. 12, no. 1, p. 012503, Jun. 2017.
33. R. Hasan et al., "Spiral Photonic Crystal Fiber-Based Dual-Polarized," IEEE Sensors Journal, vol. 18, no. 1, pp. 133–140, 2018.
34. T. Wieduwilt *et al.*, "Ultrathin niobium nanofilms on fiber opticaltapers—A new route towards low-loss hybrid plasmonic modes,"*Sci. Rep.*, vol. 5, p. 17060, Nov. 2015.
35. Shafkat A. Analysis of a gold coated plasmonic sensor based on a duplex core photonic crystal fiber. Sensing Bio-Sens Res 2020; 28:100324.
36. Momota MR, Hasan MR. Hollow-core silver coated photonic crystal fiber plasmonic sensor. Opt Mater 2018; 76:287–94.
37. Liu C, Su W, Wang F, Li X, Liu Q, Mu H, Sun T, Chu PK, Liu B. Birefringent pcf-based spr sensor for a broad range of low refractive index detection. IEEE Photon Technol Lett 2018; 30:1471–4.
38. Mollah MA, Razzak SA, Paul AK, Hasan MR. Microstructure optical fiber basedplasmonic refractive index sensor. Sensing Bio-Sens Res 2019; 24:100286.
39. Rifat AA, Haider F, Ahmed R, Mahdiraji GA, Mahamd Adikan FR, Miroshnichenko AE. Highly sensitive selectively coated photonic crystal fiber-based plasmonic sensor. Opt Lett 2018; 43:891.

40. Akter S, Rahman MZ, Mahmud S. Highly sensitive open-channels based plasmonic biosensor in visible to near-infrared wavelength. Results in Physics2019; 13:102328.

41. M. A. Habib and M. S. Anower, "A Novel Low Loss Porous-Core Photonic Crystal Fiber for Terahertz Wave Transmission," in International Conference on Electrical, Computer and Communication Engineering (ECCE), Cox's Bazar, Bangladesh, 2017.

42. E. Haque, A. Hossain, F. Ahmed, and Y. Namihira, "Surface Plasmon Resonance Sensor Based on Modified D -Shaped Photonic Crystal Fiber for Wider Range of Refractive Index Detection," IEEE Sensors Journal, vol. 18, no.20, pp. 8287 - 8293, 2018.

43. Khan S, Ahmed K, Hossain N, Paul BK, Nguyen TK, Dhasarathan V, "Exploring Refractive index sensor using Gold coated D-shaped Photonic Crystal Fiber for biosensing applications, "*Optik* (2019).

44. Chen, L. Xia, C. Li, Surface plasmon resonance sensor based on a novel D-shaped photonic crystal fiber for low refractive index detection, IEEE Photonics J. 10 (2018) 1–9.

45. Abu Sufian Sunny, S. M., Ahmed, T., Anzum, A., & Paul, A. K. (2019). Performance Analysis of a PCF SPR Based Highly Sensitive Biosensor. 2019 IEEE International Conference on Biomedical Engineering, Computer and Information Technology for Health (BECITHCON).

46. Mahabubur Rahman, M., Aslam Molla, M., Kumar Paul, A., Based, M. A., Masud Rana, M., & Anower, M. S. (2020). Numerical investigation of a highly sensitive plasmonic refractive index sensor utilizing hexagonal lattice of photonic crystal fiber. Results in Physics, 103313.

47. Khalek, M. A., Chakma, S., Paul, B. K., & Ahmed, K. (2018). Dataset of surface plasmon resonance based on photonic crystal fiber for chemical sensing applications. Data in Brief, 19, 76–81.

48. Q.M. Kamrunnahar , Jannatul Robaiat Mou , Maliha Momtaj, Dual-core gold coated photonic crystal fiber plasmonic sensor: Design and analysis.ResultsinPhysics2020;18:103319.

49. Hasan, M., Akter, S., Rifat, A., Rana, S., & Ali, S. (2017). A Highly Sensitive Gold-Coated Photonic Crystal Fiber Biosensor Based on Surface Plasmon Resonance. Photonics, 4(4), 18.

50. Hossen, M. N., Ferdous, M., Abdul Khalek, M., Chakma, S., Paul, B. K., & Ahmed, K. (2018). Design and analysis of biosensor based on surface plasmon resonance. Sensing and Bio-Sensing Research.

51. Chu, S., Kaliyaperumal, N., Abobaker, A. M., Aphale, S. S., P, R. B., & Senthilanathan, K. (2018). Design and Analysis of Surface Plasmon Resonance based Photonic Quasi-Crystal Fibre Biosensor for High Refractive Index Liquid Analytes. IEEE Journal of Selected Topics in Quantum Electronics, 1–1.

52. Liang, H.; Shen, T.; Feng, Y.;Liu, H.; Han,W. A D-Shaped Photonic Crystal Fiber Refractive Index Sensor Coated with Graphene and Zinc Oxide. Sensors 2021, 21, 71.

53. A. A. Rifat et al., “Photonic Crystal Fiber-Based Surface Plasmon Resonance Sensor with Selective Analyte Channels and Graphene-Silver Deposited Core,” Sensors, vol. 15, no. 5 pp. 11499–11510, 2015.

54. Lou, J., Cheng, T., Li, S., & Zhang, X. (2019). Surface plasmon resonance photonic crystal fiber biosensor based on gold-graphene layers. Optical Fiber Technology, 50, 206–211.

55. S. Islam et al., “A Hi-Bi Ultra-Sensitive Surface Plasmon Resonance Fiber Sensor,” IEEE Access, vol. 7, pp. 79085–79094, 2019.
56. Kretschmann, E. and Reather, H. Radiative decay of nonradiative surface plasmon excited by light. Z.Naturf. 23A: 2135-2136; 1968.

57. Kretschmann, E. Die Bestimmung optischer Konstanten von Metallen durch Anregung von Oberflachenplasmaschwingugnen. Z Phys 241: 313-324; 1971.

58. Otto, A. Excitation of nonradiative surface plasma waves in silver by the method of frustrated total reflection. Z Phys 216: 398-410; 1968.

59. Leidberg, B., et al., Surface Plasmon Resonance for Gas-Detection and Biosensing. Sensors and Actuators, 4(2): p. 299-304, 1983.

60. Pockrand, I. et al Surface plasmon spectroscopy of organic monolayer assemblies. Surface Sci. 74: 237-244; 1978.

61. Peterlinz, K. A. and Georgiadis, R. Two-color approach for determination of thickness and dielectric constant of thin films using surface plasmon resonance. Opt.Commun. 130: 260-266; 1996.
62. Liedberg, B. et al Principles of biosensing with an extended coupling matrix and surface plasmon resonance. Sensors and Actuators B 11: 63-72; 1993.

63. Zhang, L. and Uttamchandani, D. Optical chemical sensing employing surface plasmon resonance. Electron Lett. 23: 1469-1470; 1988.

64. Striebel, Ch. et al Characterization of biomembranes by spectral elipsometry, surface plasmon resonance and interferometry with regard to biosensor application. Biosens.Bioelectron. 9: 139-146; 1994.

65. Lofas, S. and Johnsson, B. A novel hydrogel matrix on gold surfaces in surface plasmon resonance sonsors for fast and efficient covalent immobilization of ligands. J.chem.soc., chem commun. 1526-1528; 1990.

66. Lofas, S. Dextran modified self-assembled monolayer surfaces for use in biointeraction analysis with surface plasmon resonance. Pure & Appl.Chem. 67: 829-834; 1995.

67. S. Sjolander and C. Urbaniczky, “Integrated fluid handling system for bio-molecular interaction analysis.” Analytical Chemistry vol. 63, pp. 2338-2345,1991.
68. B.D. Gupta and A.K. Sharma,“Sensitivity evaluation of a multi-layered surface plasmon resonance-based fiber optic sensor: A theoretical study.”Sens. Actuators B Chem., vol. 107, no. 9, pp. 40–46,2005.
69. B. D. Gupta and R. K. Verma, Surface Plasmon Resonance-Based Fiber Optic Sensors: Principle, Probe Designs, and Some Applications, Journal of Sensors, 2009,1-12,2009.

70. Descrovi, E., Paeder, V., Vaccaro, L., & Herzig, H.-P. A virtual optical probe based on localized Surface Plasmon Polaritons. Optics Express, 13(18), 7017.
71. L.C. Thomson, J. Courtial, G. Whyte, M. Mazilu, Algorithm for 3D intensity shaping of evanescent wave fields, 2007, in preparation.
72. Raether, H., [Surface plasmons on smooth and rough surfaces and on gratings], Springer, New York, 1988.
73. Kretschmann E, Raether H (1968) Notizen: radiative decay of non radiative surface plasmons excited by light. Z Naturforsch A 23:2135–2136.
74. R. Jorgenson and S. Yee, "A fiber–optic chemical sensor based on surface plasmon resonance," Sensors and Actuators B: Chemical, vol. 12, no. 3, pp. 213–220, 1993.
75. Sharma, A. K, Jha, R. and Gupta, B. D., "Fiber-optic sensors based on surface plasmon resonance: a comprehensive review," IEEE Sensors 7(8), 1118-1129 ,2007.
76. Fan, X., White, I. M., Shopova, S. I., Zhu, H., Suter, J. D. and Sun, Y., "Sensitive optical biosensors for unlabeled targets: a review," Analytica Chimica Acta 620(1-2), 8-26 ,2008.
77. Wolfbeis, O. S., "Fiber-optic chemical sensors and biosensors," Analytical Chemistry 80(12), 4269-4283 ,2008.
78. Lee, B., Roh, S. and Park, J., "Current status of micro- and nano-structured optical fiber sensors," Optical Fiber Technology 15(3), 209-221 ,2009.
79. M. A. Jabin, K. Ahmed, M. J. Rana, B. K. Paul, Y. Luo, and D. Vigneswaran, "Titanium-Coated Dual-Core D-Shaped SPR-Based PCF for Hemoglobin Sensing," Plasmonics, vol. 14, no. 6, pp. 1601–1610, 2019.
80. Tubb, A. J. C., Payne, F. P., Millington, R. B. and Lowe, C. R., "Single-mode optical fiber surface plasma wave chemical sensor," Sensors and Actuators B: Chemical 41(1-3), 71-79 ,1997.
81. Verma, R.K.; Sharma, A.K.; Gupta, B.D. Surface plasmon resonance based tapered fiber optic sensor with different taper profiles. Opt. Commun. 2008, 281, 1486–1491.
82. R. Mondragon, J.E. Julia, A. Barba, and J.C. Jarque, "Characterization of silica–water nanofluids dispersed with an ultrasound probe: a study of their physical properties and stability," Powder Technol., vol. 224, pp. 138-146, Jul. 2012.
83. H. Murata, "Recent developments in vapor phase axial deposition," J. Lightwave Technol., vol. 4, pp. 1026-1033, Aug. 1986.
84. M.S. Aruna Gandhi, K. Senthilnathan, P.R. Babu, Q. Li, Visible to near infrared highly sensitive microbiosensor based on surface plasmon polariton with external sensing approach. Results Physics 15, 8 (2019).
85. Islam MR, Jamil MdA, Zaman MdS-U, Ahsan SAH, Pulak MK, Mehjabin F, et al., "Design and analysis of birefringent SPR based PCF biosensor with ultra-high sensitivity and low loss," Optik , vol.221, 2020.
86. R. Hasan, S. Akter, A. A. Rifat, S. Rana, and S. Ali, "A Highly Sensitive Gold-Coated Photonic Crystal Fiber Biosensor Based on Surface Plasmon Resonance" Photonics, vol. 4, no. 4, pp. 18 ,2017.
87. A. A. Rifat et al., "Photonic Crystal Fiber-Based Surface Plasmon Resonance Sensor with Selective Analyte Channels and Graphene-Silver Deposited Core," Sensors, vol. 15, no. 5 pp. 11499–11510, 2015.
88. R. K. Gangwar and V. K. Singh, "Highly Sensitive Surface Plasmon Resonance Based D-Shaped Photonic Crystal Fiber Refractive Index Sensor," Plasmonics, vol. 12, no. 5, pp. 1–6, 2016.
89. A. A. Rifat, G. A. Mahdiraji, Y. M. Sua, Y. G. Shee, R. Ahmed, D. M. Chow, & F. R. M. Adrikan," Surface Plasmon Resonance Photonic Crystal Fiber Biosensor: A

Practical Sensing Approach," IEEE Photonics Technology Letters, vol.27, no. 15, pp. 1628–1631, 2015.
90. https://math.mit.edu/~stevenj/18.369/pml.pdf.
91. M. S. Islam et al., "A Hi-Bi Ultra-Sensitive Surface Plasmon Resonance Fiber Sensor," IEEE Access, vol. 7, pp. 79085–79094, 2019.
92. A. A. Rifat, G. A. Mahdiraji, R. Ahmed, D. M. Chow, Y. M. Sua,Y. G. Shee, M. J. Shawon, F. R. Mahamd Adikan, ''Copper Graphene-based photonic crystal fiber plasmonic biosensor,'' IEEE Photonics Journal, vol.8, pp. 1–7, 2016.
93. X. Yang, Y. Lu, B. Liu, et al., Analysis of graphene-based photonic crystal fiber ensor using birefringence and surface plasmon resonance, Plasmonics 12 (2) (2017) 489e496.
94. Firoz Haider, Rifat Ahmmed Aoni, Rajib Ahmed, and Andrey E. Miroshnichenko, "Highly amplitude-sensitive photonic-crystal-fiber-based plasmonic sensor," J. Opt. Soc. Am. B 35, 2816-2821 (2018).Firoz Haider, Rifat Ahmmed Aoni, Rajib Ahmed, and Andrey E. Miroshnichenko, "Highly amplitude-sensitive photonic-crystal-fiber-based plasmonic sensor," J. Opt. Soc. Am. B 35, 2816-2821 (2018).
95. Hoseinian, M.S., Bolorizadeh, M.A. Design and Simulation of a Highly Sensitive SPR Optical Fiber Sensor. *Photonic Sens* 9, 33–42 (2019).
96. F. Mohr, "Gold chemistry: applications and future directions in the life sciences". New York, USA: Wiley, 1–408 (2009).
97. Rahman, M.M., Rana, M.M., Anower, M.S. *et al.* Design and analysis of photonic crystal fiber-based plasmonic microbiosensor: an external sensing scheme. *SN Appl. Sci.* 2, 1194 (2020).
98. M. Mahfuz, M. Mollah, M. Momota et al., "Highly sensitive photonic crystal fiber plasmonic biosensor: Design and analysis," , Optical Materials, vol. no 90 (2019).
99. M. Rakibul Islam, M. Khan, F. Mehjabin et al., "Design of a fabrication friendly & highly sensitive surface plasmon resonance-based photonic crystal fiber biosensor," , Result in Physics, vol. 19 (2020).
100. Mohammad Rakibul Islam, A. N. M. Iftekher, Kazi Rakibul Hasan, Md. Julkar Nayen, and Saimon Bin Islam, "Dual-polarized highly sensitive surface-plasmon-resonance-based chemical and biomolecular sensor," Appl. Opt. 59, 3296-3305 (2020).
101. Md. Saiful Islam, Jakeya Sultana, Rifat Ahmmed Aoni, Md. Selim Habib, Alex Dinovitser, Brian W.-H. Ng, Derek Abbott, "Localized surface plasmon resonance biosensor: an improved technique for SERS response intensification", Optics Letter, Vol. 44, No. 5 (2019).
102. Araf Shafkat, "Analysis of a gold coated plasmonic sensor based on a duplex core photonic crystal fiber, Sensing and Bio-Sensing Research, vol no. 28 (2020).
103. M. R. Hasan, S. Akter, A. A. Rifat, S. Rana, K. Ahmed, R. Ahmed, H. Subbaraman, and D. Abbott, "Spiral photonic crystal fiber-based dual-polarized surface plasmon resonance biosensor," IEEE Sensors Journal 18, 133-140 (2018).
104. A. Rifat, G. Mahdiraji, D. Chow, Y. Shee, R. Ahmed, and F. Adikan, "Photonic Crystal Fiber-Based Surface Plasmon Resonance Sensor with Selective Analyte Channels and Graphene-Silver Deposited Core," Sensors, vol. 15, pp. 11499-11510 (2015).
105. E. Haque, M. A. Hossain, F. Ahmed and Y. Namihira, "Surface Plasmon Resonance Sensor Based on Modified D -Shaped Photonic Crystal Fiber for Wider Range of Refractive Index Detection," in *IEEE Sensors Journal*, vol. 18, no. 20, pp. 8287-8293, 15 Oct.15 (2018).
106. https://www.rp-photonics.com/optical_spectrum_analyzers.html.

107. Md. S. Islam, C. M. B. Cordeiro, J. Sultana, R. A. Aoni, S. Feng, R.581 Ahmed, M. Dorraki, A. Dinovitser, B. W.-H. Ng, and D. Abbott, “A Hi-Bi ultra-sensitive surface plasmon resonance fiber sensor”, IEEE 583 Access (2019).
108. F. Haider, R. A. Aoni, R. Ahmed, M. S. Islam and A. E. Miroshnichenko, "Propagation Controlled Photonic Crystal Fiber-Based Plasmonic Sensor via Scaled-Down Approach," in *IEEE Sensors Journal*, vol. 19, no. 3, pp. 962-969, 1 Feb.1 (2019).
109. M. Sakib, S. Islam, T.Mahendiran et al. “Numerical Study of Circularly Slotted Highly Sensitive Plasmonic Biosensor: A Novel Approach”, Results in Physics, Volume 17 (2020).
110. D. Li, W. Zhang, H. Liu, J. Hu, and G. Zhou, "High sensitivity refractive index sensor based on multicoating photonic crystal fiber with surface plasmon resonance at near-infrared wavelength," IEEE Photonics Journal 9, 1-8 (2017).
111. Md. Biplob Hossain, S.M. Riazul Islam, K.M. Tasrif Hossain, Lway Faisal Abdulrazak, Md. Nazmus Sakib, I.S. Amiri, “High sensitivity hollow core circular shaped PCF surface plasmonic biosensor employing silver coat: A numerical design and analysis with external sensing approach”, Results in Physics, Volume 16 (2020).
112. M. R. Islam et al., “Design and numerical analysis of a gold-coated photonic crystal fiber based refractive index sensor,” Opt. Quantum Electron., vol. 53, no. 2, 2021.
113. M. A. Mollah, S. M. R. Islam, M. Yousufali, L. F. Abdulrazak, M. B. Hossain, and I. S. Amiri, “Plasmonic temperature sensor using D-shaped photonic crystal fiber,” Results Phys., vol. 16, no. January, p. 102966, 2020.
114. Y. Peng, J. Hou, Z. Huang, and Q. Lu,“Temperature sensor based on surface plasmon resonance within selectively coated photonic crystal fiber”, *APPLIED OPTICS* , vol. 51, no. 26, pp. 6361-6367, 10 September 2012.
115. M. Y. Azab, M. Farhat, O. Hameed and S. S. A. Obayya, “Temperature Sensors Based on Plasmonic Photonic Crystal Fiber”, Computational Photonic Sensors, pp. 179-201, 2019.
116. Md. Abu Bakar Siddik et al., “ Design and Evaluation of Liquid Filled PCF Temperature Sensor Based on SPR,” 2020 IEEE Region 10 Symposium (TENSYMP), 5-7 June, 2020.